AUTOMATED MATERIALS DISCRIMINATION USING 3D DUAL-ENERGY X-RAY IMAGES

Ta Wee Wang B.Eng.

A thesis submitted in partial fulfilment of the requirements of The Nottingham Trent University for the degree of Doctor of Philosophy

School of Engineering,
Faculty of Computing and Technology,
The Nottingham Trent University,
Burton Street,
Nottingham, UK.

Collaborating Establishment:

Home Office Science and Technology Group,
Police Scientific Development Branch (P.S.D.B),
Sandridge,
Hertfordshire, UK.

August 2002

ACKNOWLEDGEMENTS

I would like to extend my sincere thanks to the following people for their help during the research programme.

To my director of studies Dr. Paul Evans for his guidance and valuable advice throughout the research project.

To my second supervisor Professor Max Robinson for his encouragement and helpful advice.

To Dr. Dev Chakraborty (Associate Professor of Radiological Physics at the University of Pennsylvania, USA) for his helpful advice.

To Professor Dick Lacey and his team at the Home Office Science and Technology Group, P.S.D.B., Sandridge, UK for their support throughout the research programme.

To Dr. Simon Godber of Image Scan Holdings plc for his assistance and useful advice.

DEDICATION

For my Parents and Brothers
with Gratitude and Affection.

AUTOMATED MATERIALS DISCRIMINATION USING 3D DUAL-ENERGY X-RAY IMAGES

Ta Wee Wang

ABSTRACT

The ability of a human observer to identify an explosive device concealed in complex arrangements of objects routinely encountered in the 2D x-ray screening of passenger baggage at airports is often problematic. Standard dual-energy x-ray techniques enable colour encoding of the resultant images in terms of organic, inorganic and metal substances. This transmission imaging technique produces colour information computed from a high-energy x-ray signal and a low energy x-ray signal (80keV<E<140keV). The broad nature of this materials discrimination places plastic explosive in the same organic window as other innocuous organic items. Also, images of a threat substance which has been masked by other materials will result in colour encoding which is proportional to the effective atomic number of the threat material and the masking material. The work presented in this thesis enables the effective atomic number of the target material within a specified window ($6.6 \leq Z_{eff} \leq 13$) to be automatically discriminated from many layers of overlapping substances. This is achieved by applying a basis materials subtraction technique to the data provided by a wavelet image segmentation algorithm. This imaging technique is reliant upon the image data for the masking substances to be discriminated independently of the target material. Further work investigated the extraction of depth data from stereoscopic images to estimate the mass density of the target material.

A binocular stereoscopic dual-energy x-ray machine previously developed by the Vision Systems Group at The Nottingham Trent University in collaboration with The Home Office Science and Technology Group provided the image data for the empirical investigation. This machine utilises a novel linear castellated dual-energy x-ray detector recently developed by the Vision Systems Group. This detector array employs half the number of scintillator-photodiode sensors in comparison to a conventional linear dual-energy sensor. The castellated sensor required the development of an image enhancement algorithm to remove the spatial interlace effect in the resultant images prior to the calibration of the system for materials discrimination.

To automate the basis materials subtraction technique a wavelet image segmentation and classification algorithm was developed. This enabled overlapping image structures in the x-rayed baggage to be partitioned. A series of experiments was conducted to investigate the discrimination of masked target materials. It was found that the system noise produced significant errors in the polynomial equations used for estimating the thickness of the aluminium and plastic basis materials. However, a successful demonstration of an automated technique for discriminating a plastic plate in some realistic scenarios has been demonstrated. Although, the technique will only work correctly if the materials masking the target fall within the window of effective atomic number defined by the chosen basis materials. Thus, for instance a steel mask would produce a false negative result.

In order to discriminate it accurately a material would require the determination of its mass density. This could be provided within the reported basis material subtraction theory if the thickness of the target were known. However, the depth resolution (±6.7mm) produced by the experimental stereoscopic system was found to be too coarse for inclusion in the automated material discrimination program.

SYMBOLS

a_1	Basis material coefficient for basis material 1
a_2	Basis material coefficient for basis material 2
a_c	Compton contribution to μ
a_p	Photoelectric contribution to μ
A_c	Path integrals of a_c
A_p	Path integrals of a_p
A	Atomic weight
B_s	Linear translation speed (m/s)
σ	Convergence angle
θ	Characteristic angle
E	X-ray energy
f_c	Klein-Nishina formula for Compton scatter
f_p	Energy dependence of the photoelectric interaction
f_s	Detector scan frequency
$g(k)$	Detail filter
$h(k)$	Smooth filter
$H(n)$	Histogram
HI	High energy signal
I	Measured intensities with attenuation
I_o	Measured intensities without attenuation
LO	Low energy signal
μ	Linear attenuation coefficient
μ/ρ	Mass attenuation coefficient
δP	Minimum parallax
ρ	Mass density
r_0	Classical electron radius
S_s	Coarse signal (i.e. smooth signal) approximation at scale s
$S(E)$	X-ray energy spectrum distribution
$S_L(E_L)$	Low energy x-ray spectra
$S_H(E_H)$	High energy x-ray spectra
t	Thickness
t_1	Aluminium basis material thickness
t_2	Plastic basis material thickness
T_L	Low energy logarithmic transmission
T_H	High energy logarithmic transmission
w_n	Weight fraction of component n
W_s	Wavelet coefficients (i.e. detail signals) at scale s
δX	Projected field of view of individual scintillator elements in the translation X-axis (i.e. motion axis)
δZ	Minimum resolvable depth increment
Z	Atomic number
Z_{eff}	Effective atomic number

ABBREVIATIONS

BMD	Basis Materials Decomposition
BMS	Basis Materials Subtraction
CT	Computed Tomography
FAA	Federal Aviation Administration
FNA	Fast Neutron Analysis
keV	kilo electron Voltage
kVp	kilo Voltage peak
MRI	Magnetic Resonance Imaging
PFNA	Pulsed Fast Neutron Analysis
QRA	Quadrupole Resonance Analysis
TNA	Thermal Neutron Analysis
TNTU	The Nottingham Trent University

TABLE OF CONTENTS

CHAPTER FIVE TARGET MATERIAL CALIBRATION AND RECOGNITION

CHAPTER SIX INVESTIGATION OF DEPTH MEASUREMENT FOR MASS DENSITY EXTRACTION

CHAPTER SEVEN SUMMARY, CONCLUSIONS AND FUTURE WORK

APPENDIX A

APPENDIX B

APPENDIX C

APPENDIX D

APPENDIX E

APPENDIX F

CHAPTER ONE

INTRODUCTION

1.1 Background

On the 8th November 1895, Wilhelm Conrad Rontgen discovered x-rays during his normal routine of experiments[M1]. A screen of barium platinocyanide placed some distance away from a gas filled cathode ray tube displayed an unexpected fluorescent glow in the darkened laboratory. The first application of x-rays was in the field of medical radiography and was quickly followed by many other applications which today include security screening, non-destructive inspection of materials, diffraction and structure analysis and elemental analysis[H1]. Thus, x-rays are the most important means of investigating unknown crystal structure, chemical composition and polycrystalline orientation of materials.

In recent years the aviation security screening industry has almost universally adopted linear x-ray detector array technology for the routine 2D screening of carry-on luggage and hold cargo at airports. This technology utilises the line-scan principle of image formation and as such requires continuous relative motion between the baggage under inspection and the linear detector array. This is provided by a conveyor belt system typically operating at speeds of 0.2m/s to 0.5m/s. Initially simple systems produced 6 bit or 8 bit monochrome shadowgraph images consisting of 512x512 pixels displayed on a video monitor. In an attempt to make all the grey level data present in the images available to the human operator, image enhancement algorithms were implemented. Typically these operated on very dark or very light areas of the image content. However, although such technology can meet the stringent throughput demands of luggage in airports it does not provide the x-ray machine operator with information relating the three-dimensional shape or the material composition of the object under inspection.

The problem of materials discrimination was partially addressed by the security screening industry in the late 1980's with the development of the dual-energy sensor[G1, K1]. This technology enables materials discrimination information to be imparted to the observer in the form of colour encoded images representing organic, inorganic and metal substances. The organic compounds are defined generally as consisting of elements having effective atomic number of 10 or less, the inorganic materials are defined as being comprised of elements having effective atomic number between 10 to 20, while the metal substances have an effective atomic number greater than 20. This description is used only as a general indicator of substances and is by no means a precise materials definition. This type of system is available from companies such as the EG&G Astrophysics Research Corporation, Heimann, Vivid Technologies Incorporated and Rapiscan.

There is an increasing awareness throughout the security screening industry that the presentation of high 'quality' (i.e. high spatial resolution) three-dimensional images to a well-trained human operator will prevent high false alarm rates. This is underpinned by the findings of the UK Home Office and the USA Federal Aviation Administration (FAA). In fact the FAA Technical Centre, Atlantic City, has purchased two fully operational stereoscopic dual-energy scanners from Image Scan Holdings plc, a University spin off company. This technique is beginning to influence the security industry as it produces the highest quality 3D x-ray images available to the security-screening sector. The Nottingham Trent University (TNTU) team has conducted research in this area since their development of the first monochrome binocular stereoscopic line-scan x-ray machine in 1987, which was funded by HM Customs and Excise. This early research was expanded to include the development of a dual-energy folded array system in collaboration with the Home Office Science and Technology Group, Sandridge UK in 1992. This collaboration has been continuously in place since this time. More recently, TNTU team has developed a novel linear array castellated dual-energy x-ray detector. This new sensor[E1] is employed in the experimental binocular stereoscopic system used in the research programme reported in this thesis.

It is becoming apparent that much of the industry effort over recent years into means of automatically detecting explosives in hold baggage has been misplaced. A number of sophisticated methods have been tried. These have included nuclear techniques[G1, [E2, T1, W1] such as thermal neutron analysis (TNA), fast neutron analysis (FNA) and pulsed fast neutron analysis (PFNA). Also electromagnetic techniques[C1, G1] such as magnetic resonance imaging (MRI), quadrupole resonance analysis (QRA) and microwave imaging have been tried. In addition X-ray scatter techniques[G2, H2, J1, S1, S2] have been incorporated into commercial systems. All these technologies are designed to detect the presence of explosives and do not produce conventional image data. Generally the data is very noisy and has very poor spatial correlation with the object under inspection[W2]. Manufacturers such as Vivid Technologies who use two-dimensional x-ray imaging techniques with increased materials discrimination capability adopt a more conventional approach. Whilst the EG&G Astrophysics Research Corporation utilises twin orthogonal views produced using a pair of x-ray sources and dual-energy arrays. However this technique is wholly unsuitable for human interpretation as far as three-dimensional information is concerned. InVision Technologies and International Security Systems Inc. have opted for helical scan dual-energy tomography. However, this technique confronts the security industry with a number of problems including a high x-ray dose, slow image production, mechanical complexity and cost (i.e. £500,000). The compromise solutions that are commercially available suffer from relatively poor image quality in order to provide some 3D information. It is becoming universally accepted that the 25% to 30% false alarm rates currently produced by all types of explosive detection systems presents serious logistical problems in airport luggage handling areas. Generally these techniques cannot compete with the throughput capability of manually controlled line-scan x-ray techniques which is still the industry workhorse. Thus it is becoming increasingly apparent to the security industry that automated threat detection is currently not logistically possible. In its current form it has the potential to create more problems than it solves.

The research presented in this thesis builds upon the work of the Vision Systems Group[E3, E4, E5, E6, E7, E8, E9, E10, E11] to augment the binocular stereoscopic technique by automatically discriminating specific or target materials in the resultant stereoscopic images. A previously developed experimental binocular stereoscopic dual-energy x-ray machine produced the raw image data for the empirical analysis. The major problem in discriminating specific materials in a complex arrangement of overlapping objects is that the x-ray signal produced by the dual-energy sensor elements represents the average x-ray signature for both the 'masking structure' and the target material. This of course is a natural consequence of using transmitted radiation to form an image. To extract materials information requires combining sophisticated calibration techniques with advanced image processing capability. Therefore, the aim of this research is to develop an automated technique to segment (i.e. to delineate layers) and extract the effective atomic number (in terms of a characteristic angle) and mass density for a target material masked by other materials. In this way the binocular stereoscopic images may be improved by additional colour encoding of possible threat materials.

The initial research concentrates on the development of an image enhancement algorithm to remove the spatial interlace effect produced by the castellated detectors. This work was conducted prior to the calibration of experimental x-ray system for broad materials discrimination capability (i.e. organic, inorganic and metal materials). The automated x-ray image segmentation and categorisation algorithms were subsequently developed to segment overlapping objects in the resultant x-ray images into individual regions for further quantitative analysis. This process provided the data for basis materials subtraction (BMS) technique to extract the characteristic angle for the target material. Finally, an investigation into exploiting range information extracted from the binocular stereoscopic image pairs to obtain the target's mass density was conducted. The mathematical algorithms introduced in this thesis for the extraction of depth information from the stereoscopic dual-energy x-ray images are based on a series of successful investigations and research work previously undertaken by TNTU[E6, E12, E13, E14, E15]. However, no attempt has been made to automate the extraction of the range data as the depth resolution of the experimental system is of the order of ±6.7mm. This uncertainty in depth measurement produced mass density errors too large for practical security applications. However, the overall findings of this research have resulted in further collaboration with the Home Office UK to apply the techniques developed to more sensitive stereoscopic imaging equipment.

1.2 Objectives

The objectives of the research are summarised below in the context of the three phases in which the work was undertaken.

Phase (I):

- The development of an image enhancement algorithm to remove the spatial interlace effect produced by the dual-energy castellated sensors.
- The calibration of the experimental x-ray machine for broad materials discrimination capability.
- The empirical evaluation of the noise present in the resultant images and the repeatability of the image data.

Phase (II):

- The development of algorithms to automatically segment objects in the dual-energy x-ray images.
- The development of a program that can categorise the segmented regions in terms of overlapping structures.
- Theoretical evaluation of the basis materials decomposition (BMD) technique for specific materials discrimination capability.
- The development of a basis materials subtraction (BMS) technique to compute the characteristic angle for overlapping materials.
- Empirical evaluation of the BMS technique to extract a material's characteristic angle when masked by multiple layers of different materials.
- Combine the image segmentation based identification of overlapping image structure with the BMS technique to automatically discriminate a target material.

Phase (III):

- Investigate the extraction of depth information from the stereoscopic dual-energy x-ray images.

- Investigate the validity of establishing a target materials mass density by employing empirically derived depth data.

1.3 Structure of the Thesis

The arrangement of the thesis is summarised in the following paragraphs.

Chapter two provides general background information for the research detailed in the chapters that follow. It introduces stereoscopic dual-energy x-ray imaging, image segmentation and dual-energy materials discrimination utilising the basis materials decomposition technique.

Chapter three presents the image enhancement algorithm developed to remove the spatial interlace effect produced by the castellated detectors. Also, the calibration of the experimental x-ray machine for organic, inorganic and metal discrimination is described. Subsequently, system noise is investigated together with system repeatability to establish the stability of the experimental x-ray system's imaging chain.

Chapter four presents the development of the automated x-ray image segmentation software utilising a wavelet transform technique. This program is applied to segment potentially overlapping objects in an x-ray image into individual regions. The data is used to extract automatically the low energy and the high energy information to enable further categorisation in terms of overlapping and non-overlapping regions.

Chapter five presents a theoretical evaluation of the BMS technique for the purpose of specific materials recognition. This enables a material's characteristic angle for each layer in a multi-layered object to be computed. A series of experiments was conducted to validate the BMS technique. The automated x-ray image segmentation and categorisation programs developed in Chapter 4 are combined with the BMS technique to produce an automated target recognition program.

Chapter six describes the investigation of extracting a target materials mass density by establishing its thickness from stereoscopic parallax measurements.

Chapter seven is a summary of the results, conclusions and the direction of further work.

Following the main text is a list of publications and reference material, the appendices include the following information:

- calibration data for the plastic, aluminium and steel stepwedges;
- computational results for the materials discrimination curves;
- grey level noise data;
- automated image categorisation results;
- software listing for the automated target material detection program;
- automated target material detection results.

CHAPTER TWO

BACKGROUND INFORMATION

2.1 Introduction

The information presented in this chapter provides a background to the development of a technique to automatically discriminate target materials utilising the image data provided by an experimental binocular stereoscopic dual-energy x-ray machine. Central to this investigation is the extraction of a material's characteristic angle (i.e. effective atomic number[L1]) and mass density from the resultant stereoscopic dual-energy images.

The discussion presented is divided into the following three broad areas:

- stereoscopic dual-energy x-ray imaging;
- image segmentation;
- dual-energy materials discrimination.

A binocular stereoscopic design theory has been employed successfully by the Vision Systems Group at TNTU to the development of camera systems for use with teleoperated robotic manipulator arms[A1, F1, P1, R1, R2, R3, R4, R5, R6, R7, S3, S4] and x-ray screening systems[E3, E4, E5, E7, E8, E12, E13, E14, E15, E16]. The algorithms to extract depth information from the stereoscopic x-ray image pairs utilise this previous work to investigate the optimisation of the materials discrimination process.

An automated image segmentation technique that is based on wavelet analysis is introduced. The x-ray image segmentation is a preliminary image processing task that is required for automated materials recognition.

The initial discussion on dual-energy x-ray imaging presents the fundamental properties of x-ray interaction with materials within the x-ray energy region of 30-200 keV. This provides a background to discriminating target materials which utilises the BMD technique developed by Alvarez and Macovski[A2, L2] in the field of medical imaging. This approach is modified by the author to access the feasibility of this technique for target materials recognition in aviation security screening.

2.2 Stereoscopic X-ray Imaging

The Manual of photogrammetry[L3] defines stereoscopy as:

"......... the science and art that deals with the use of images to produce a three-dimensional visual model with characteristics analogous to those of actual features viewed using true binocular vision."

Stereoscopy was introduced to radiology by J. Mackenzie Davidson in 1898[C3]. The advantages of stereoradiography as far as interpreting three-dimensional structure is concerned has long been acknowledged in the field of medical imaging and more recently security screening. The application of stereoscopy in x-ray imaging originates from the operating principle of the human visual system[D1, H5, K2, S5, T2, V1]. Binocular parallax is one of the most robust depth cues utilised by a human observer[O1, P2]. This cue can only exist when the observer's eyes are focused and converged onto an object producing a *conjugate image point* on the retina of each eye. If the convergence point image is taken as a reference in each eye, points which lie in front or beyond of this point in object space will give rise to images which are relatively displaced on the retina as a function of range hence producing depth information.

A binocular stereoscopic x-ray screening system[E6, E16] can greatly enhance the observer's understanding of the true nature of the three-dimensional scene under observation. The extraction of depth information from the resultant stereoscopic images may also be exploited if the conjugate points can be identified in each perspective image and suitable coordinate measurement algorithms are employed.

A stereoscopic x-ray imaging system has two basic prerequisites:

- The points on the inspected object must lie in the field of view of the 'left' x-ray beam and the 'right' x-ray beam to form an overlapping field of view or stereoscopic region in object space.
- The conjugate image points situated within the stereoscopic region must be located to obtain three-dimensional coordinate information from object space[D5, H6, M3]. The identification of the conjugate image points is termed the *correspondence problem* and it is not within the scope of this thesis. However, there are partial solutions to this problem that have been developed by other researchers which include the use of edge-detection and grey-level matching[D2, H6] and neural networks[M4]. However, a manual solution to the correspondence problem is adopted in this research.

Fig. 2.1 illustrates the schematic diagram of the experimental stereoscopic line-scan dual-energy x-ray screening system utilised in this research[E16]. The X and Y-axis in the diagram are in the plane of the conveyer belt. Thus the Z-axis also termed the depth or range axis is normal to the plane of linear translation.

The experimental x-ray machine has an inspection tunnel height of 0.4 m and a width of 0.6 m. It utilises a polychromatic x-ray source with nominal accelerating voltage of 140 kVp and a tube current of 1 mA. The slit collimated x-ray beams are arranged at angles of ±3.75° about the normal to the plane of linear translation (conveyer belt). The x-ray source output is filtered by a 0.5 mm Aluminium strip that helps to remove the lower energy x-rays that are not useful.

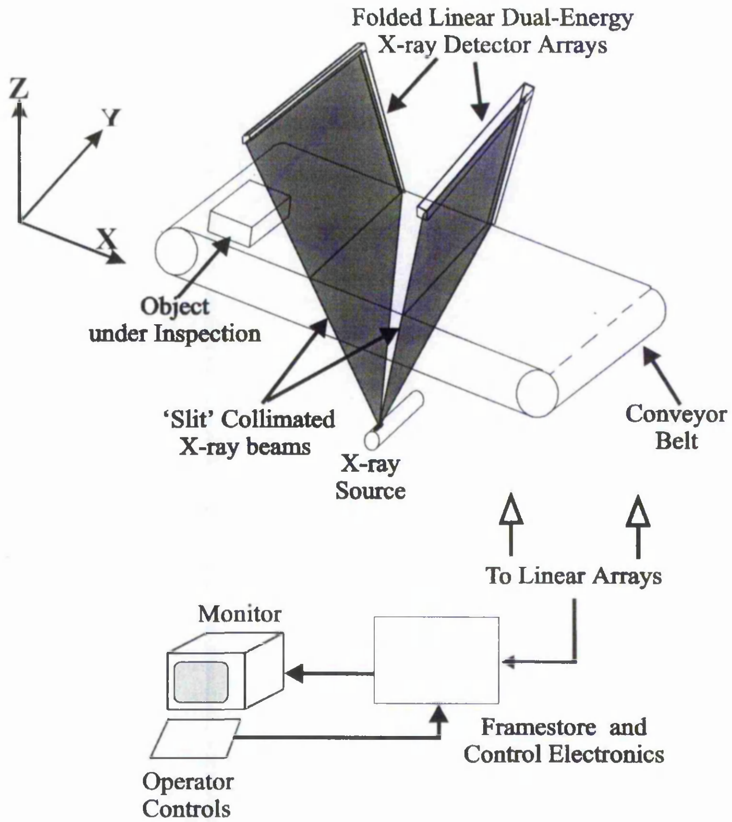

Fig. 2.1 Experimental binocular stereoscopic folded array dual-energy x-ray system.

The folded linear array detectors employed in the experimental system utilise the new castellated array dual-energy x-ray detector[E1]. This detector employs a side-by-side low energy/high energy scintillator arrangement. Its physical principles of operation are similar to the standard sandwich detector arrangement. The design detail of the castellated detector array is described in Chapter 3.

The folded array configuration of dual-energy detectors ensures that the full cross sectional area of the inspection tunnel is available for imaging. It can be appreciated from Fig. 2.2 that the midline normal to each detector module comprising the folded array is positioned at 90° with respect to the x-ray source. Each detector module has 16 low energy and 16 high energy scintillation elements.

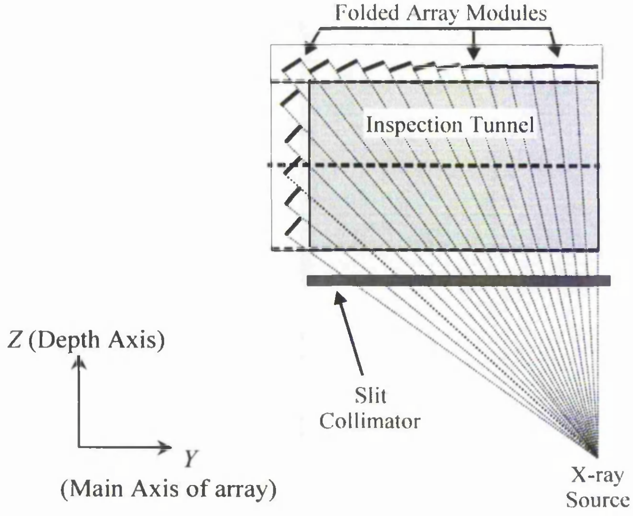

Fig. 2.2 Folded linear dual-energy x-ray detector array.

The object under inspection is translated by a conveyer belt at a constant speed (typically 0.2 m/s) through the inspection tunnel in which a pair of divergent collimated x-ray beams are arranged to illuminate each of the dual-energy detector modules (i.e. scintillator-photodiode array). Thus, a binocular stereoscopic pair image can be produced from the pixel columns collected from the folded array sensors[E13, E14, E15] during the scanning process.

2.2.1 Depth Information

The ability of the stereoscopic system shown in Fig. 2.1 in resolving depth information (Z-axis) is dependent on the *voxel*[H5] dimensions. In the context of this work, the overlapping field of view of two pixels in object space forms a volume element (i.e. *voxel*). Hence, the entire stereoscopic region is made up from voxels.

Fig. 2.3 illustrates the dependency of voxel dimensions on the convergence angle[H11] σ of the x-ray beams and the projected field of view δX of individual scintillator elements (i.e. pixels) in the translation X-axis (i.e. motion axis) in object space. It can be deduced that as the convergence angle increases (i.e. $\sigma_2 > \sigma_1$), the minimum resolvable depth increment δZ in object space reduces (i.e. $\delta Z_2 < \delta Z_1$). On the other hand, δZ will also become smaller as the δX decreases. Thus, δX can be decreased by increasing the detectors' scan frequency although this is limited by the physical dimensions of the scintillator elements.

Therefore, a large convergence angle σ and small δX are required to improve the measurement capability of a stereoscopic x-ray system. However, the maximum allowable convergence angle is limited by the maximum permissible parallax in the resultant stereoscopic images. In other words the screen parallax must be constrained to that which can be fused by an observer comfortably[F2, J2].

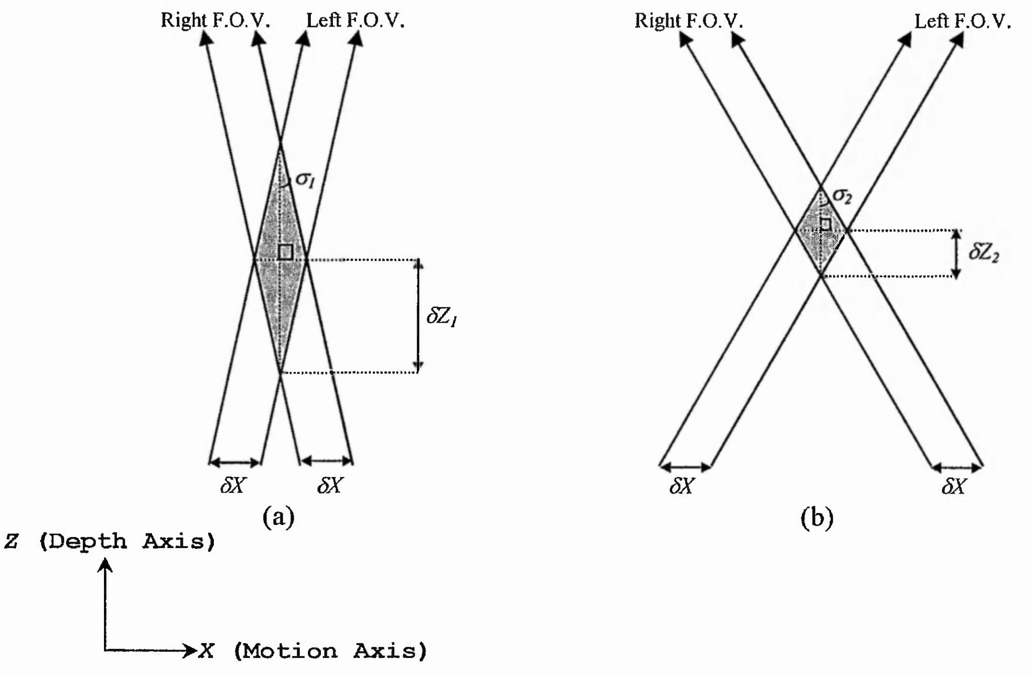

Fig. 2.3 Illustration of the dependency of voxel dimensions on the convergence angle σ and the field of view in the X-axis of a pixel element δX[E16].

2.3 Dual-energy X-ray Imaging

The concept of utilising two photon energies (i.e. dual-energy) to obtain information on tissue characteristics in medical imaging was first suggested by Jacobson[J3] in 1953. The idea was extended to the field of computed tomography (CT)[F4, K5, R9, S12] in 1976 by Alvarez and Macovski to employ spectral information inherent in x-ray attenuation measurements for bone/tissue characterisation[A2, F6, M2]. Theoretically, the dual-energy x-ray screening technique can potentially offer a major advance in the ability to distinguish between materials differing only slightly in atomic composition[S6, S14].

The conventional dual-energy x-ray imaging technique utilises a dual monochromatic or a polychromatic x-ray beam and detectors with differential energy discrimination (high energy and low energy) to determine the amount of organic, inorganic or metal substances along the line of sight throughout the object under inspection. It is very helpful since plastic explosives are organic compounds[A3, G3].

Dual-energy x-ray imaging can be achieved by either acquiring two separate images using different x-ray tube voltages[B1, D3, D4] or by using a dual-energy sandwich detector[B2, D3, D4]. The first technique relies on direct switching of the x-ray accelerating voltage which requires two separate exposures to be made[S10], hence any movement by the object will cause the possibility of motion misregistration artefacts during image acquisition. Besides that, two images must be acquired thus doubling the imaging time, equipment load and radiation dose to the examined targets[B2]. In addition, rapidly switching the x-ray tube voltage for the low and the high x-ray energy can be technically difficult[G5].

The second approach requires a k-edge pre-filtering technique, which involves passing the x-ray output through a filter material that has a k-shell absorption edge within the energy range of the tube's output x-ray spectrum[H9]. The k-edge filter facilitates a double peak x-ray spectrum. The resulting spectrum is effectively split into low energy and high energy components. The security screening industry has adopted a line-scan based dual-energy technique developed during the late 1980's.

The standard dual-energy linear detector array utilised by industry consists of a sandwich structure of two scintillation elements through which the x-ray beam passes. In such a scheme, the signal from the first 'thin' scintillation sensor arises primarily from low energy photons while the signal from the second 'thick' scintillation sensor arises from the remaining higher energy photons. This sensor is described in more detail in the following section.

2.3.1 Sandwich Detector Array

Screen or film radiography has significantly contributed to the field of medical imaging and non-destructive inspection of materials. Image intensifiers and imaging plates consisting of phosphor screens[D3] have been employed for conventional radiographic applications. More recently, linear x-ray detector arrays[G8, H7, H8, K3, S8, T3] consisting of a linear array of discrete semiconductor photodiodes optically coupled to a strip of scintillation material have been widely adopted for security screening applications. This imaging technique employs a slit collimated x-ray beam which significantly reduces radiation scattering[W3, W4] thereby producing increased image contrast in the resultant digital images.

The digital radiography approach is capable of converting the detected x-ray photons into electronic signals that have the following advantages[A4, C5, G4, G8, H7, T3]:

- High sensitivity and a high signal to noise ratio can be obtained;
- Energy information from the incident x-ray photons can be measured.

The digital dual-energy radiography technique is now widely applied in the field of medical imaging[A2, B1, D4, F3, G6, T3] and security screening[B4, G6, K1, R10].

The linear array detector system is not suitable for capturing dynamic events. It requires the inspected object to be (internally) static during the image acquisition process. The only movement involved is the relative linear translation generally provided by a conveyer belt. The images are displayed on a video monitor as each *strip* of the irradiated object is captured by the linear array detector system.

A typical sandwich dual energy detector is shown in Fig. 2.4. The front or low energy scintillators are exposed to the full spectral content of the x-ray beam and preferentially absorb the low energy x-ray photons while allowing the majority of the high energy photons to be detected by the rear scintillator (high energy). The scintillators are utilised for converting x-ray radiation to visible light and the silicon photodiode detectors are used to convert the visible light produced by the scintillation process to electrical signals. Thus, two spatially equivalent samples of irradiated object space can be obtained simultaneously. As a result, dual radiographs (i.e. low energy and high energy images) can be produced from a single exposure where the low energy and the high energy signals can be utilised for materials discrimination.

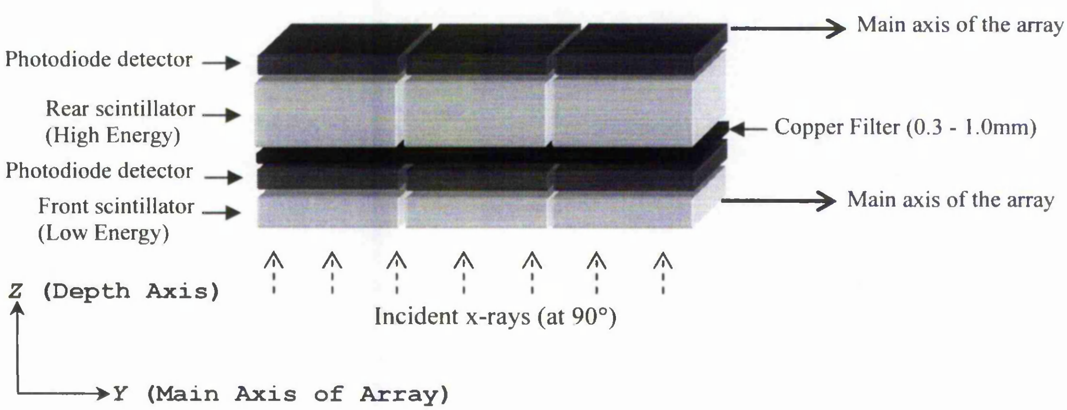

Fig. 2.4 A linear dual-energy x-ray sandwich detector array.

A copper filter with thickness approximately 0.3 to 1.0 mm is placed in between the front and rear scintillators to increase the effective energy of the x-ray beam incident on and absorbed by the rear scintillators. This results in a greater and more desirable energy separation between the x-rays absorbed in both the front and rear scintillators[H9, S11]. However, the filter has the effect of hardening the x-ray beam and reducing the radiation intensity in the detected high energy signals. Consequently, a reduced signal-to-noise ratio in the rear detector may result[G8].

2.3.2 Line-scan Image Formation

The digital image is produced by storing the individual signal outputs from each scintillator-photodiode element in digital memory (i.e. framestore), during the relative translation of the inspected object with respect to the detector array and x-ray source. The image is accumulated *strip by strip* (or line by line) over a time interval of typically 6 s that is determined by the conveyer belt speed and the scan frequency of the detector array. Therefore, the image data may be displayed as panning onto the video screen during the image acquisition process.

The total number of the detector elements (i.e. scintillator-photodiode pairs) along the length of the linear array will determine the pixel resolution in the *Y*-axis (i.e. main axis of array). The scan frequency of the detector system and the conveyer belt speed will determine the pixel resolution in the *X*-axis (i.e. motion axis).

It can be appreciated from Fig. 2.5 that the low energy and the high energy image data are produced for each pixel location in the resultant image.

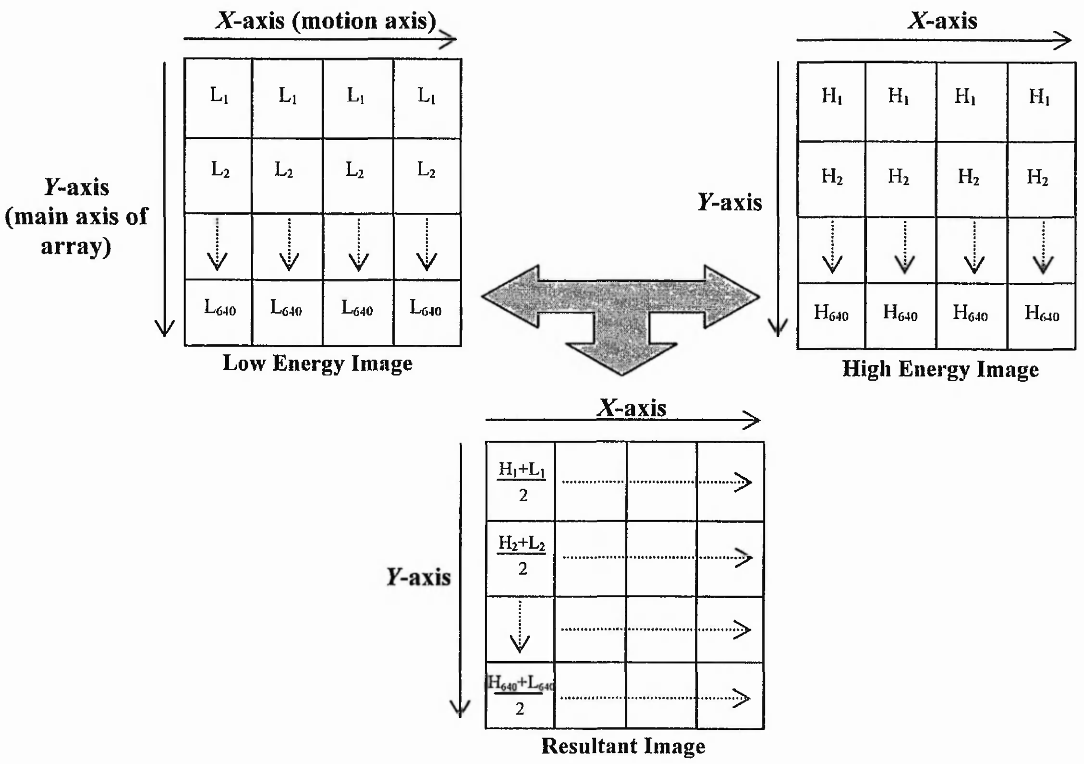

Fig. 2.5 Spatially discrete image digitisation produced by a 'sandwich' detector array.

The monochrome images acquired from scanning baggage sample-1 utilising a dual-energy sandwich detector array are shown in Fig. 2.6.

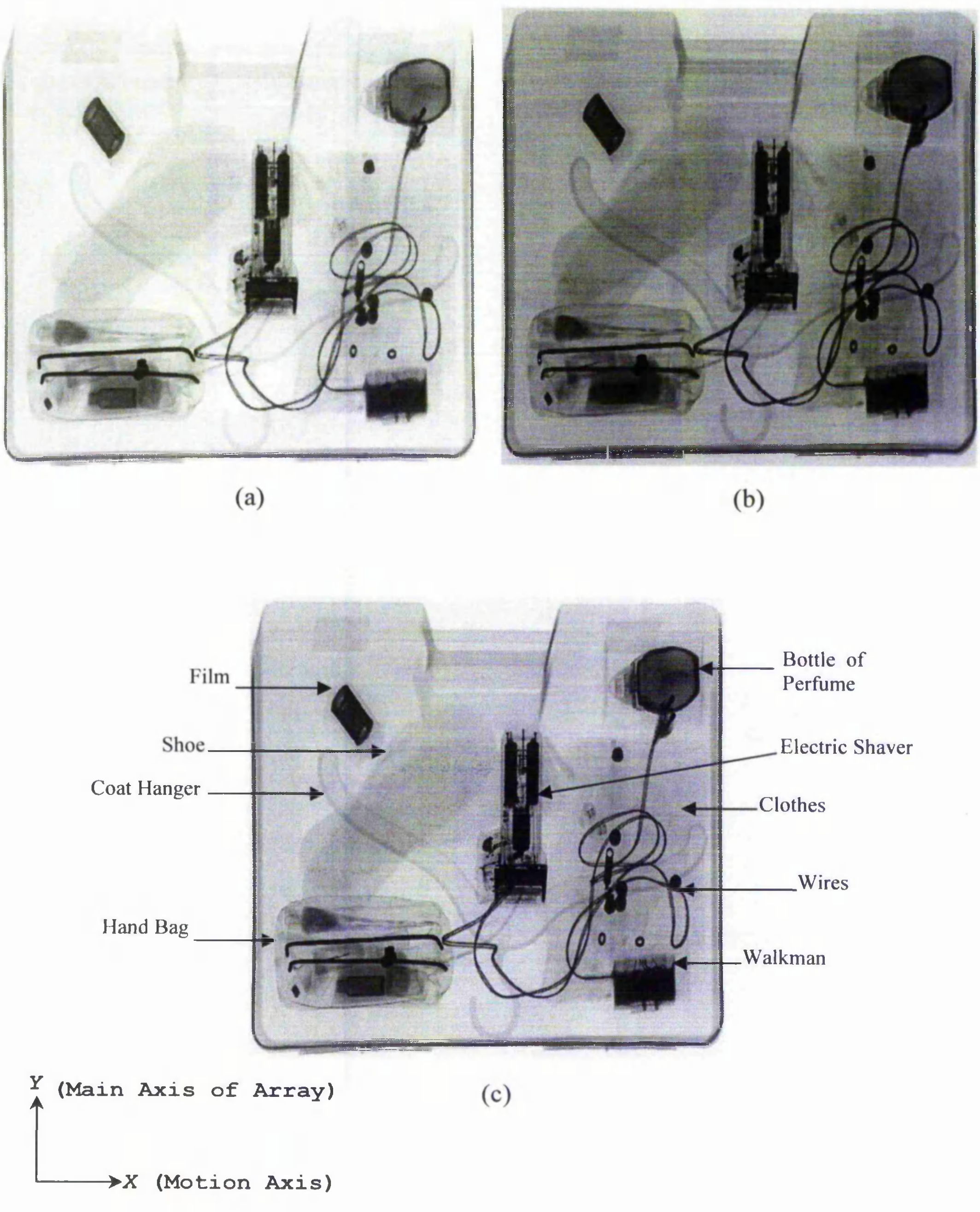

Fig. 2.6 Monochrome images of baggage sample-1 utilising a linear sandwich detector array: (a)- High energy image, (b)- Low energy image and (c)- Resultant image.

2.3.3 Limitations

Threat items such as plastic explosives tend to have higher densities compared to common plastics and hydrocarbon fibres. Therefore, they have greater x-ray attenuation than normally found for innocuous materials in luggage. There are marked differences in attenuation at optimum energies around 10 keV for a thin sheet of explosives[L4]. An unfortunate exception is wool[L4]. Hence, even at low energies, the system measurement errors will lead to Z_{eff} ranges which will obscure distinctions between materials. In addition, baggage inspection normally requires considerably higher energies (i.e. 80-140 keV) to penetrate through typical baggage contents. At these high energies, a thin sheet of explosive (≈2 to 5 mm) is almost transparent to the x-ray system.

2.4 Image Segmentation

The main goal of image segmentation is to split the original image into a set of connected regions, each defined by a uniform grey level intensity[K4, R11, T4]. This process enables the spatially discrete blocks of data to be extracted for further processing and analysis. Segmentation strategies for a real time system must be both robust and consistent with the overall vision system to be of practical use in the field.

The critical problem in searching for target materials like plastic explosives is the requirement to resolve each layer of the materials present in the baggage. The problem becomes worse for the complicated arrangements of overlapping objects routinely encountered in security screening applications. Therefore, pre-processing procedures such as segmentation require to be applied to reduce the overlapping objects into smaller more manageable regions (homogeneous grey level areas).

There are many image segmentation techniques that have been developed by researchers over recent years. A comparison and evaluation of a number of segmentation techniques is detailed in the survey by S.U. LEE[L5] and the paper by Jean-Christophe Olivo[O3]. The automated image segmentation technique based on wavelet analysis as presented by Jean-Christophe Olivo[O2, O3] and Stephane Mallat[M5] is employed in this research. The approach was proved computationally effective and stable. Additionally, the approach describes the segmented image in terms of homogeneous regions instead of edge-based segmentation of images. This information is very useful in this research work, since overlapping materials with homogeneous thickness in an x-ray image require segmenting before its characteristic angle and mass density can be computed.

2.4.1 Wavelet Transform

"The wavelet transform is a linear operation that decomposes a signal into components that appear at different scales and is based on the convolution of the signal with a dilated filter" [O3]. The wavelet transform of a function $f(x)$ at the scale s and position x is given by the convolution product[M5]:

$$W_s f(x) = f * \psi_s(x)$$

where $\psi_s(x) = \frac{1}{s}\psi\left(\frac{x}{s}\right)$ is the dilation of the mother wavelet $\psi(x)$ by a factor s *(scale $s=2^j$, where $j=0,1,2...$)*. The scale s characterises the size and regularity of the signal features extracted by the wavelet transform. When the scale s decreases, the support of $\psi_s(x)$ decreases so the wavelet transform is sensitive to finer details where the locations of sharper variations in an image can be detected.

The discrete wavelet transform algorithm consists of a recursive sequence of convolutions with two discrete filters $h(k)$ and $g(k)$[B5, G7, M5] (where k=0,1…5). These filters represent respectively the transfer functions of a low-pass filter (i.e. smooth filter, $h(k)$) and a high-pass filter (i.e. detail filter, $g(k)$). At scale s=1, the algorithm computes with $h(k)$ a coarser resolution representation of the smooth signal S_1, and also with $g(k)$ where the wavelet coefficients W_1 (i.e. detail signal) will be generated. The low-pass filter $h(k)$ is used for the calculation of the wavelet coefficients and is of a coarser resolution representation at the next scale (i.e. W_2^1 and S_2^1, W_2^2 and S_2^2 and etc.). The wavelet coefficients W_s can be interpreted as the details removed by the successive applications of the wavelet transform to the coarse signal approximation S_s. The zero-crossings of the derived wavelet transform W_s curve indicate the location of the input signal's sharper variation points. The sharp variation points of a signal are always implied to the important features in an image[O3]. Therefore, the image segmentation task can be carried out automatically if all these sharp variation points are known in advance.

The detail and smooth wavelet filter coefficients are defined by Stephane Mallat[M5] as the following:

$g(k)$ = {0.7118, -0.2309, -0.1120, -0.0226, 0.0062, 0.0039},

$h(k)$ = {0.4347, 0.2864, 0.0450, -0.0393, -0.0132, 0.0032}.

It is not within the scope of this thesis to provide a detailed study of the wavelet transform. A more detailed presentation of the wavelet transform can be found in references[B5, G7, M5, O2, O3, S9].

2.5 Dual-energy Materials Discrimination

The aim of dual-energy radiography is to provide information about the chemical composition of the x-rayed materials in terms of their effective atomic number and mass density[C7, H3]. This information is extremely useful in the fields of medical imaging, security screening and non-destructive inspection.

The dual-energy approach provides the parameter of effective atomic number, which enables a means of distinguishing materials. The term effective atomic number Z_{eff} refers to the average atomic number of that hypothetical single element which produces the same x-ray attenuation as a compound being measured[R8, C2]. In other words, Z_{eff} represents the average atomic number weighted according to each element's contribution towards attenuating the x-ray beam. This is conveyed by the following relationship[L1]:

$$(\mu/\rho)\,(Z_{eff}, E) \;=\; \Sigma\;(\mu/\rho)_n\,(Z_n, E)\,w_n \qquad \text{Equation 2-1}$$

where the mass attenuation coefficient μ/ρ is a function of atomic number Z and x-ray energy E, ρ is the material mass density, w_n is the weight fraction of component n, and Σ represents a summation over all components. Every element can be characterised by material Z_{eff} and mass density. Since x-ray attenuation at a particular energy is a function of both material composition (i.e. Z_{eff} and ρ) and x-ray energy, the two parameters Z_{eff} and ρ can be separated by making measurements at dual energies.

In radiology (i.e. 30-200 keV), every material has unique interactions with the x-rays by Compton scattering and photoelectric absorption. The photoelectric effect dominates at lower energies and is mainly dependent on the atomic number of the material whereas the Compton effect dominates at higher energies and is mainly dependent on the mass density of the material[C4, E17, I2, J4]. Hence, if the attenuating material is imaged in two different energy windows (i.e. low energy and high energy x-ray spectrum), the amount of attenuation due to each of the effects can be calculated and thus the effective atomic number and mass density of the material can be subsequently computed[C7, H3, H4, S6, F3].

Ideally, materials can be discriminated by two energy independent constants, which can be obtained from the measurements of the changes in the transmitted low energy and high energy x-ray spectrum detected by the dual-energy x-ray sensors. The two energy independent constants characterise the integrated Compton scattering and photoelectric attenuation coefficients. Alvarez and Macovski stated that, above the k-edge, the total linear attenuation coefficient μ (E) of a given material for photon energies in the x-ray range of 30-200 keV could be expressed approximately as a linear combination of Compton and photoelectric interaction coefficients [A2, C6, G9, L2, W2, W5]. Note that Rayleigh scattering is not considered, because it is only important in low energy photons and its total quantity is too small to be important for the x-ray energy (140 kVp)[H4] considered in this programme of work.

$$\mu(E) \approx a_c f_c(E) + a_p f_p(E) \qquad \text{Equation 2-2}$$

where E is the incident x-ray energy, $a_c \approx k_1 \rho Z / A$ is the Compton contribution to μ (E), ρ is the mass density, Z and A are the atomic number and atomic weight respectively, k_1 is Avogadro's number, f_c (E) is the Klein-Nishina formula for

Compton scatter; and $a_p \approx k_2 \rho Z^{4.8} / A$ is the photoelectric contribution to $\mu(E)$, k_2 is a proportional constant which includes Avogadro's number, and $f_p(E) \approx (1/E)^{3.2}$.

The Klein-Nishina function $f_c(E)$ is defined as[L2]:

$$f_c(\alpha) = 2\pi r_0^2 \left[\frac{1+\alpha}{\alpha^2} \left[\frac{2(1+\alpha)}{1+2\alpha} - \frac{1}{\alpha} \ln(1+2\alpha) \right] + \frac{1}{2\alpha} \ln(1+2\alpha) - \frac{1+3\alpha}{(1+2\alpha)^2} \right] \qquad \text{Equation 2-3}$$

where r_0 is the classical electron radius and $\alpha = E / 510.975$ keV.

The functions $f_c(E)$ and $f_p(E)$ have physical meaning where $f_c(E)$ represents the energy dependence of the total cross section for Compton scattering and $f_p(E)$ approximates the energy dependence of the photoelectric interaction. The amount of a_c and a_p provide a basis for distinguishing materials having different effective atomic numbers and mass density.

The logarithmic transmission T (unconventional use of the term 'transmission' for the quantity T[A2, L2]) of a collimated pencil x-ray beam through a volume in an object of interest with thickness t is given by:

$$I = I_o \int S(E) \exp(-\mu t)\, dE$$

$$T = \ln\left(\frac{I_o}{I}\right) = \ln\left(\int S(E) \exp\{ [a_c f_c(E) + a_p f_p(E)]\ t \}\ dE \right)$$

$$= \ln\left(\int S(E) \exp\ [A_c f_c(E) + A_p f_p(E)]\ dE \right) \qquad \text{Equation 2-4}$$

where I and I_o are the measured intensities with and without attenuation respectively, $S(E)$ is the x-ray energy spectrum distribution, $A_c = \int a_c\, ds$, and $A_p = \int a_p\, ds$ are the path integrals of a_c and a_p respectively, where ds is a short section of path length.

Materials are characterised by values of a_c and a_p[A2, L2]. Dual-energy screening is employed to allow the separation of the total attenuation coefficient into these two energy independent components by utilising the measurements of the low energy and high energy x-ray attenuations. If $S_L(E_L)$ and $S_H(E_H)$ are the low energy and high energy x-ray spectra, the logarithmic transmission for T_L and T_H can be respectively expressed as:

$$T_L = \ln(\frac{I_o}{I})_L = \ln(\int S_L(E_L) \exp\{[a_c f_c(E_L) + a_p f_p(E_L)]\ t\}\ dE)$$

$$= \ln(\int S_L(E_L) \exp\ [A_c f_c(E_L) + A_p f_p(E_L)]\ dE) \qquad \text{Equation 2-5}$$

$$T_H = \ln(\frac{I_o}{I})_H = \ln(\int S_H(E_H) \exp\{[a_c f_c(E_H) + a_p f_p(E_H)]\ t\}\ dE)$$

$$= \ln(\int S_H(E_H) \exp\ [A_c f_c(E_H) + A_p f_p(E_H)]\ dE) \qquad \text{Equation 2-6}$$

The challenge in dual-energy imaging is to resolve the values A_c and A_p from the measured values of T_L and T_H by solving Equations 2-5 and 2-6. For monochromatic radiation, the logarithmic transmission is a linear exponential function of the traversed thickness t, thus Equations 2-5 and 2-6 can be simplified to two first-order equations:

$$T_L = [a_c f_c(E_L) + a_p f_p(E_L)]\ t$$
$$= A_c f_c(E_L) + A_p f_p(E_L) \qquad \text{Equation 2-7}$$

$$T_H = [a_c f_c(E_H) + a_p f_p(E_H)]\ t$$
$$= A_c f_c(E_H) + A_p f_p(E_H) \qquad \text{Equation 2-8}$$

Thus, the two unknowns A_c and A_p in the Equations 2-7 and 2-8 can be solved to discriminate a material.

However, for polychromatic radiation, the Equations 2-5 and 2-6 require to be expanded to include higher order terms (i.e. which can be modelled by polynomial functions) to compensate for x-ray beam hardening effect[Y1] which increases as the thickness of the irradiated substances increases. A general form of polynomials of 2nd or 3rd order has been widely used to compensate for these effects (see Equations 2-14 and 2-15 on page 29)[A2, C6].

The advantage of polychromatic radiation is that it provides a high intensity source compared to monochromatic radiation. This is vital for the throughputs required for baggage screening at airports where the x-ray scanning, image processing and decision analysis require to be accomplished in approximately 6 seconds per luggage item. The experimental x-ray machine utilised in this research utilises a polychromatic x-ray source.

2.5.1 Organic, Inorganic and Metal Discrimination

In general, the signals produced by the low energy and the high energy detectors, can be employed to determine the basic discrimination between organic, inorganic and metal substances[B1, S6, I1]. The organic compounds are defined generally as consisting of elements having effective atomic number of 10 or less, the inorganic materials are defined as being comprised of elements having effective atomic number between 10 to 20, while the metal substances are defined as having an effective atomic number greater than 20. The organic material present in an x-ray image is displayed in an orange colour with the appropriate intensity, the metal substance is displayed in blue whilst the inorganic material is displayed in green. This broad definition of materials has been widely adopted by the manufacturers of security x-ray equipment. However, it is used only as a general indicator of substances and is by no means a precise definition.

To produce colour encoded images requires that the materials discrimination curves (known as *banana curves* in the security industry) for three different types of materials be obtained, namely plastic (i.e. organic), aluminium (i.e. inorganic) and steel (i.e. metal). The graph of Fig. 2.7 plots the difference between the high energy and low energy signals versus the high energy signals. This data is derived by sequentially imaging the plastic, aluminium and steel stepwedges. The curves A and B illustrated in Fig. 2.7 are fitted at the mid-points between the steel-aluminium and the aluminium-plastic curves respectively. Thus, the region below curve B is defined as the organic signature, the region between curve A and B is defined as the inorganic signature while the region above curve A is defined as the metal signature. The detail of the calibration process for materials discrimination is presented in Chapter 3.

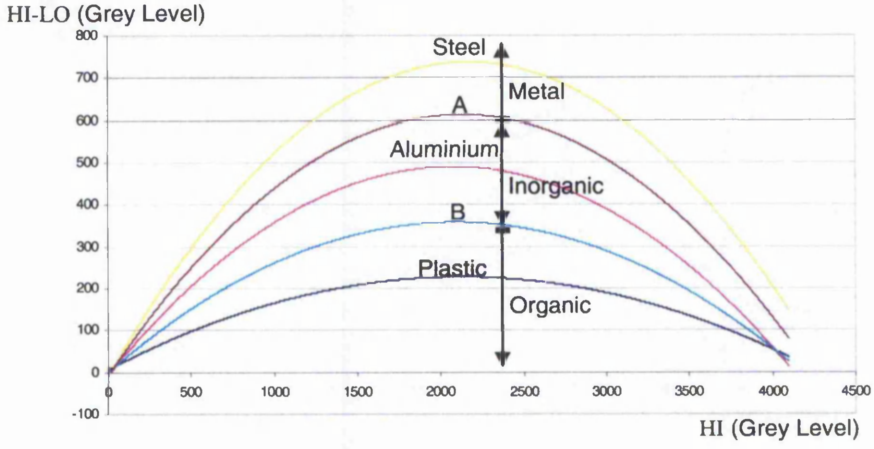

Fig. 2.7 Materials discrimination curves for plastic, aluminium and steel stepwedges.

2.5.2 Discriminating Target Materials

In the following text, the dual-energy basis materials decomposition (BMD) technique is discussed. This is based on work by Alvarez and Macovski 1976, Nalcioglu and Lou 1977, Brody *et al*, and Lehmann *et al* 1981 [A2, A4, L2, N1, S13], for the purpose of extracting characteristic angle (i.e. effective atomic number) and mass density of an attenuating material in the field of medical imaging.

Dual-energy x-ray screening enables the determination of the energy independent material properties (i.e. a_c:Compton scattering and a_p:photoelectric attenuation coefficients). Accurate energy independent constants for every material can, in principle, be obtained at any given x-ray energy using the BMD technique. Previous researchers have observed that the linear attenuation coefficient $\mu_\xi(E)$ of any material ξ at any given energy E can be expressed as a linear combination of the linear attenuation coefficients $\mu_1(E)$ and $\mu_2(E)$ of two basis materials 1 and 2[A2, L2]. If Equation 2-2 is an equality for material ξ and two other basis materials 1 and 2, then:

$$\mu_\xi(E) \approx a_{c\xi} f_c(E) + a_{p\xi} f_p(E) \qquad \text{Equation 2-9(a)}$$

$$\mu_1(E) \approx a_{c1} f_c(E) + a_{p1} f_p(E) \qquad \text{Equation 2-9(b)}$$

$$\mu_2(E) \approx a_{c2} f_c(E) + a_{p2} f_p(E) \qquad \text{Equation 2-9(c)}$$

Equations 2-9(b) and 2-9(c) can be solved simultaneously for $f_c(E)$ and $f_p(E)$, which can be substituted into Equation 2-9(a) to produce:

$$\mu_\xi(E) \approx a_{1\xi}\mu_1(E) + a_{2\xi}\mu_2(E) \qquad \text{Equation 2-9(d)}$$

with $a_{1\xi} = \dfrac{a_{p\xi}\,a_{c2} - a_{c\xi}\,a_{p2}}{a_{c2}\,a_{p1} - a_{c1}\,a_{p2}}$ Equation 2-9(e)

and $a_{2\xi} = \dfrac{a_{p\xi}\,a_{c1} - a_{c\xi}\,a_{p1}}{a_{c1}\,a_{p2} - a_{c2}\,a_{p1}}$ Equation 2-9(f)

Hence, the basis material decomposition of the linear attenuation coefficient is equated to the photoelectric and Compton decomposition. Physically, the basis material coefficients $a_{1\xi}$ and $a_{2\xi}$ are assumed independent of energy E and represent the mass fractions of the basis materials 1 and 2 which are required to produce the same attenuation as a unit thickness of the material ξ[A2, L2].

A dual-energy x-ray technique computes the line integrals of the linear attenuation coefficient: $\int \mu(E)\,ds$. This is equivalent to making measurements of the line integrals of coefficients $a_{1\xi}$ and $a_{2\xi}$. From Equation 2-9(d):

$$\int \mu_\xi(E)\,ds \approx \left[\int a_{1\xi}\,ds\right] \mu_1(E) + \left[\int a_{2\xi}\,ds\right] \mu_2(E)$$

or in terms of mass attenuation coefficients:

$$\int \frac{\mu_\xi(E)}{\rho_\xi}\,ds \approx \int \frac{\mu_1(E)}{\rho_1} a_{1\xi}\,ds + \int \frac{\mu_2(E)}{\rho_2} a_{2\xi}\,ds$$

$$\therefore \quad \int \mu_\xi(E)\,ds = t_1\,\mu_1(E) + t_2\,\mu_2(E)$$

For single projection imaging[A2, L2]:

$$t_1 = \int \frac{\rho_\xi}{\rho_1} a_{1\xi}\,ds = \frac{\rho_\xi}{\rho_1} a_{1\xi}\,t_\xi \qquad \text{Equation 2-10}$$

$$t_2 = \int \frac{\rho_\xi}{\rho_2} a_{2\xi}\,ds = \frac{\rho_\xi}{\rho_2} a_{2\xi}\,t_\xi \qquad \text{Equation 2-11}$$

where ρ is the mass density, t_ξ is the thickness of the attenuating material ξ, t_1 and t_2 are the thickness of basis materials 1 and 2 which together produce the same attenuation at any x-ray energy E as the thickness of the material ξ. Therefore, the quantity of basis materials (i.e. t_1 and t_2) are utilised as the independent constants instead of the Compton and the photoelectric components (i.e. a_c and a_p). The BMD technique with aluminium and plastic (i.e. t_1 and t_2) as the basis materials are employed in this research. They are used as basis materials because they bracket the range of effective atomic numbers ($6.6 \leq Z_{eff} \leq 13$), which contain plastic explosives[G1, R10]. Additionally, they are easily fabricated for the calibration procedure.

The equivalent basis materials thickness (t_1 and t_2) for any attenuating material ξ can be derived from the measured T_L and T_H by applying one of the following three techniques[A2, C6, L2, M2, S13]:

- non-linear equations;
- direct approximation method;
- subregion direct approximation method.

This research programme utilises the direct approximation method with 3rd order polynomial equations. This is because the direct approximation method enables relatively faster computation time compared to the non-linear equations approach[C6]. Additionally, the subregion direct approximation method is not employed by the author because it is more sensitive to system noise[C6].

Non-linear Equations:

Alvarez and Macovski[A2] applied a second-order polynomial equation to approximate the low (T_L) and high (T_H) energy logarithmic transmission as a series of two basis materials t_1 and t_2:

$$T_L = a_0 + a_1 t_1 + a_2 t_2 + a_3 t_1 t_2 + a_4 t_1^2 + a_5 t_2^2 \qquad \text{Equation 2-12}$$

$$T_H = b_0 + b_1 t_1 + b_2 t_2 + b_3 t_1 t_2 + b_4 t_1^2 + b_5 t_2^2 \qquad \text{Equation 2-13}$$

The coefficients a_i and b_i, $i = 0, 1, 2 \ldots, 5$, are determined by polynomial least square estimation during the calibration procedure in which the basis materials with various known thickness combinations are examined radiographically. Using the calibration polynomials, any dual-energy transmission measurements may be transformed into its basis material equivalent components, provided that the examination configuration has not changed in terms of x-ray tube accelerating voltage (kVp), tube current (mA) and source-detector distance[G10]. After the coefficients a_i and b_i are determined, the decomposition of the two basis materials t_1 and t_2 from the measured values of T_L and T_H can be accomplished by utilising the Newton-Raphson iteration method to solve the Equations 2-12 and 2-13 numerically.

The major drawback in using the Newton-Raphson iteration method is that it can be computationally slow and convergence may be difficult to achieve in practice[A2].

Direct Approximation Method:

The thickness of each basis material can also be expressed as a polynomial function of the logarithmic attenuation measurements T_H and T_L (Nalcioglu and Lou 1977, Brody *et al*, and Lehmann *et al* 1981), where t_1 and t_2 can be directly approximated as a third power series of T_H and T_L:

$$t_1 = c_0 + c_1T_L + c_2T_H + c_3T_LT_H + c_4T_L^{\,2} + c_5T_H^{\,2} + c_6T_L^{\,2}T_H^{\,2} + c_7T_L^{\,3} + c_8T_H^{\,3}$$

Equation 2-14

$$t_2 = d_0 + d_1T_L + d_2T_H + d_3T_LT_H + d_4T_L^{\,2} + d_5T_H^{\,2} + d_6T_L^{\,2}T_H^{\,2} + d_7T_L^{\,3} + d_8T_H^{\,3}$$

Equation 2-15

The coefficients c_i and d_i, i = 0, 1, 2 ..., 8, are determined through a calibration procedure in which the true basis materials thicknesses are known by using a polynomial least square fitting algorithm. This direct approximation method enables a relatively faster computation time compared to the non-linear equations approach. However, its accuracy requires further improvement.

Subregion Direct Approximation Method:

The subregion direct approximation method was suggested by K.S. Chuang[C6] in 1986. This approach divides the range of the low energy and the high energy logarithmic transmission values into ten subregions where each has its own beam hardening correction factors. Thus, the measured data for the low energy and the high energy logarithmic transmission will fall into one of the ten low energy subregions and one of the ten high energy subregions. The corresponding thickness of each basis material is approximated by a second-order power series in T_L and T_H:

$$t_1 = e_0 + e_1T_L + e_2T_H + e_3T_LT_H + e_4T_L^{\,2} + e_5T_H^{\,2}$$

Equation 2-16

$$t_2 = f_0 + f_1 T_L + f_2 T_H + f_3 T_L T_H + f_4 T_L^{\,2} + f_5 T_H^{\,2} \qquad \text{Equation 2-17}$$

A set of coefficients e_i and f_i is computed by a standard least square fitting algorithm for each of the low energy and the high energy subregions by using data pertaining to these two regions. This technique is proved computationally efficient and accurate but is sensitive to system noise[C6].

2.5.2.1 Characteristic Angle

From the BMD technique[A2, L2] (from Equations 2-10 and 2-11):

$$\frac{t_2}{t_1} = \frac{\rho_1\, a_{2\xi}}{\rho_2\, a_{1\xi}} \qquad \text{Equation 2-18(a)}$$

t_1 and t_2 are the thickness of basis materials 1 and 2 that can be computed by using the polynomial fit equations obtained from one of the techniques described in Section 2.5.2.

From Equations 2-9(e) and 2-9(f), and with $a_c \approx k_1 \rho\, Z/A = N_g$ and $a_p \approx k_2 \rho\, Z^{4.8}/A = k_{2'} N_g Z^{3.8}$ (where $k_{2'} = k_2/k_1$):

$$a_{1\xi} = \frac{N_{g\xi}\,(Z_\xi^{\,3.8} - Z_2^{\,3.8})}{N_{g1}\,(Z_1^{\,3.8} - Z_2^{\,3.8})} \qquad \text{Equation 2-18(b)}$$

and

$$a_{2\xi} = \frac{N_{g\xi}\,(Z_1^{\,3.8} - Z_\xi^{\,3.8})}{N_{g2}\,(Z_1^{\,3.8} - Z_2^{\,3.8})} \qquad \text{Equation 2-18(c)}$$

By substituting $a_{1\xi}$ and $a_{2\xi}$ from Equations 2-18(b) and 2-18(c) into Equation 2-18(a):

$$\frac{t_2}{t_1} = \frac{\rho_1}{\rho_2} \times \frac{N_{g1}\,(Z_1^{\,3.8} - Z_\xi^{\,3.8})}{N_{g2}\,(Z_\xi^{\,3.8} - Z_2^{\,3.8})}$$

Thus, the ratio t_2 / t_1 is a function of the atomic number of the particular material ξ. The quantities t_1 and t_2 may be plotted as illustrated in Fig. 2.8 in which the characteristic angle $\theta = \tan^{-1}[t_2/t_1]$ depends only on the material's effective atomic number and the aluminium and plastic basis planes [A2, L2].

$$\text{characteristic angle, } \theta = \tan^{-1}\left(\frac{t_2}{t_1}\right) \qquad \text{Equation 2-19}$$

Fig. 2.8 illustrates the basis projection of a material ξ characteristic angle θ. Measurements on materials with the same composition will have the same gradient and hence lie along the same line. Thus, any material ξ within the basis window can be projected by the combination of vector t_1 and t_2 through the equation:

$$\xi = t_1 \cos\theta + t_2 \sin\theta \qquad \text{Equation 2-20}$$

Therefore, the characteristic angle θ is a convenient indicator of the effective atomic number of a target material.

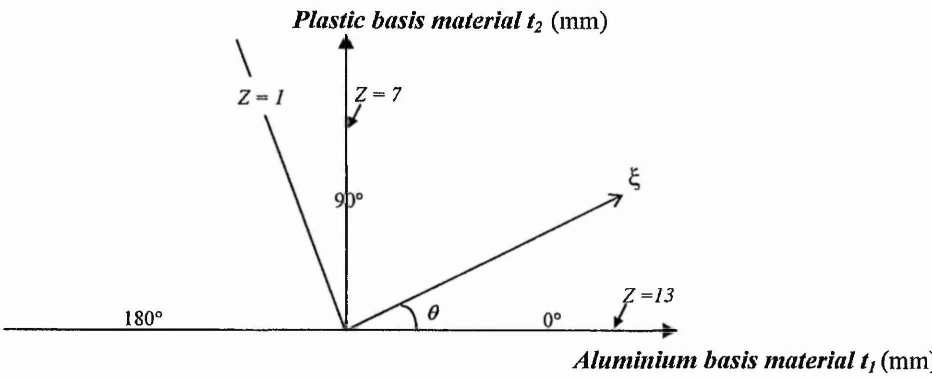

Fig. 2.8 Material discrimination using plastic (t_2) and aluminium (t_1) as the basis materials[L2].

2.5.2.2 Mass Density

From Equations 2-10 and 2-11:

$$\rho_\xi = \frac{\rho_1 t_1}{t_\xi a_{1\xi}} \qquad \text{Equation 2-21}$$

$$\rho_\xi = \frac{\rho_2 t_2}{t_\xi a_{2\xi}} \qquad \text{Equation 2-22}$$

Every target material ξ has unique values of basis material coefficients $a_{1\xi}$ and $a_{2\xi}$. For example, the theoretical values of $\{a_{1\xi}, a_{2\xi}\}$ for the aluminium and plastic basis materials are {1.00,0.00} and {0.00,1.00} respectively. The respective values for aluminium and plastic mass density, ρ_1 and ρ_2 are 2.702 g cm^{-3} and 1.4 g cm^{-3}. The thickness of each basis material t_1 and t_2 can be computed by using the polynomial fit equations obtained from one of the techniques described in Section 2.5.2. Therefore, the mass density of the inspected material ξ (ρ_ξ) can be obtained from Equations 2-21 or 2-22, provided that the thickness of the attenuated material t_ξ is known. The experimental stereoscopic x-ray system can provide depth information which could be used to provide mass density information.

Hence, the characteristic angle θ which is directly proportional to the material's effective atomic number together with the mass density can be utilised to search for a target material. This information can be appreciated from the Z_{eff} versus mass density map for various materials as illustrated in Fig. 2.9.

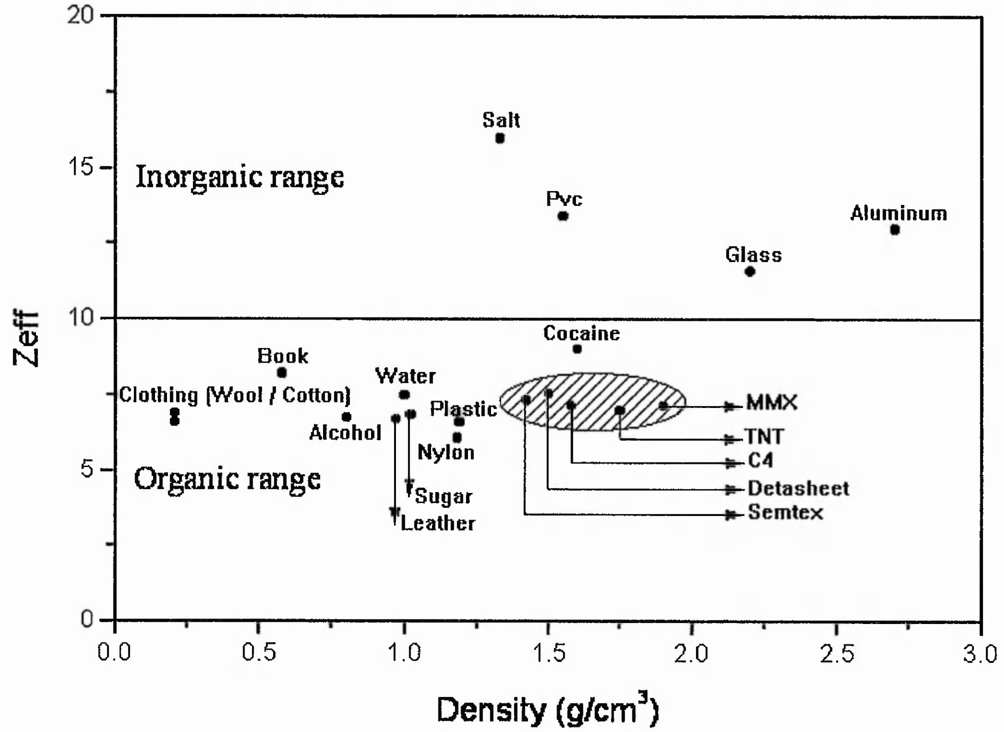

Fig. 2.9 The Z_{eff} and mass density for common items found in airport luggage and for cocaine and some explosive materials[R10].

CHAPTER THREE

CALIBRATION OF THE STEREOSCOPIC DUAL-ENERGY X-RAY MACHINE

3.1 Introduction

This chapter presents the calibration of the experimental dual-energy binocular stereoscopic machine in terms of its monochrome and colour encoded materials discrimination imaging capability. The Vision Systems Group at TNTU has developed a novel castellated linear array dual-energy x-ray detector[E1]. This sensor utilises half the number of scintillator elements in comparison to a conventional sandwich detector arrangement. Therefore, it substantially reduces the detector bandwidth, sensor complexity and cost. The castellated sensor is employed in the experimental machine illustrated in Fig. 3.1 which was utilised for the research work presented in this thesis.

An image enhancement algorithm is developed to remove the spatial interlace effect inherent in the images produced by the castellated detector array. This enables the experimental machine to be calibrated for broad materials discrimination capability. The de-interlaced images are colour encoded for the discrimination of organic, inorganic and metal substances. A series of experiments conducted to examine the noise characteristics of the experimental system is also discussed.

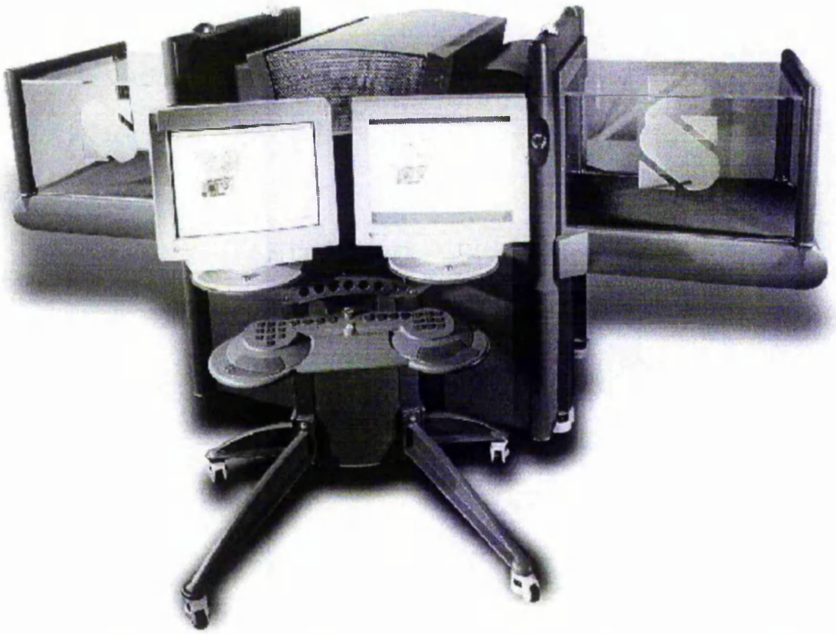

Fig. 3.1 The experimental binocular stereoscopic line-scan dual-energy x-ray screening system (the basis for a commercial product manufactured by Image Scan Holdings plc, a University spin off company).

3.2 Castellated Detector Array

Fig. 3.2 depicts the spatial configuration of the castellated dual-energy detector array[E1]. The array has alternating portions of thick (~5 mm) and thin (~0.6 mm) scintillators along its length. The thick scintillator material enables signals corresponding to the high energy attenuations (i.e. equivalent to the rear scintillator in Fig. 2.4 on page 16) to be produced while the thin scintillator material provides signals corresponding to the low energy attenuations (i.e. equivalent to the front scintillator in Fig. 2.4). The scintillation elements employed in the castellated detector array are made from Thallium-doped Caesium Iodide CsI(Tl). Each array element is coupled to a silicon photodiode which detects the visible light signals produced when x-rays strike the scintillators. The filter layer reduces the extent of the lower energy component producing a response in the thick scintillators. While, the thin scintillators are exposed to the whole x-ray spectrum and will preferentially absorb the lower energy x-ray photons and transmit the majority of the high energy photons.

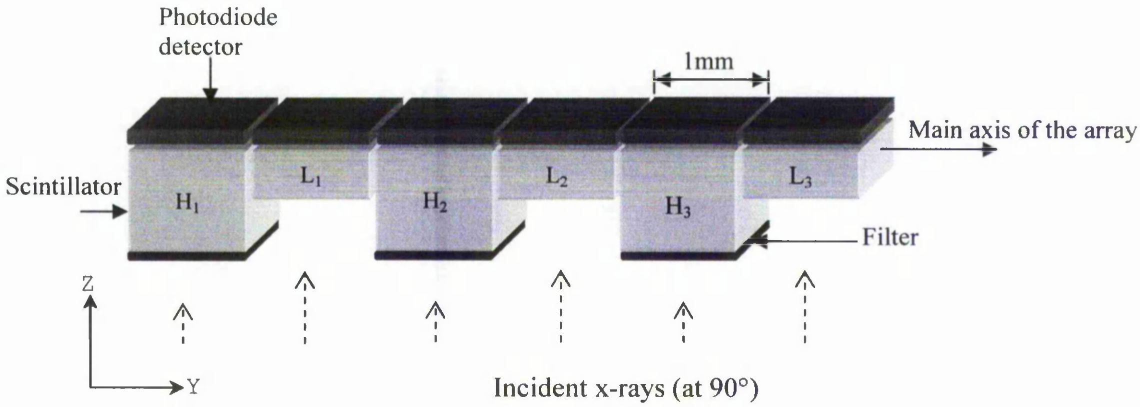

Fig. 3.2 The castellated linear dual-energy x-ray detector array.

It can be appreciated from Fig. 2.5 on page 17 that a linear array sandwich detector would require two signals (i.e. low energy and high energy signals) for each pixel to be generated simultaneously. For a stereoscopic system shown in Fig. 2.1 on page 11, the number of signals required is doubled. This begins to pose a problem in terms of data collection, transmission, and data handling and processing. Therefore, a detector arrangement which will provide both materials discrimination capability and stereoscopic images but which is economical in terms of the number of signals it produces is highly desirable. This can be achieved by the castellated arrangement which only utilises half the sensor elements of a sandwich detector array and produces very similar imaging performance.

3.2.1 Interlaced Image

The castellated detector array utilises 320 high energy and 320 low energy detector elements arranged in a modular folded linear array to produce a pixel resolution of 640 in the *Y*-axis of the resultant digital image. The scan frequency (200 Hz) of the detector array and the conveyer belt speed are set to produce a 1024 pixel resolution in the *X*-axis or motion axis.

The high energy and low energy sampling of space produced by the castellated array is depicted in the matrix of Fig. 3.3.

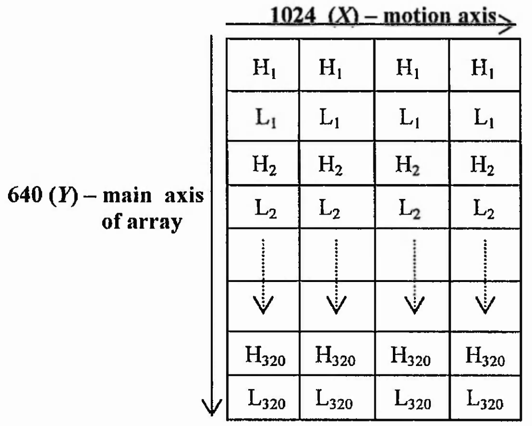

Resultant Monochrome Image

Fig. 3.3 Spatially discrete sampling produced by the castellated detector.

Fig. 3.4 shows the original composite monochrome images for baggage sample-2 illustrating the spatial interlace effect produced by the thick and thin castellated detector elements.

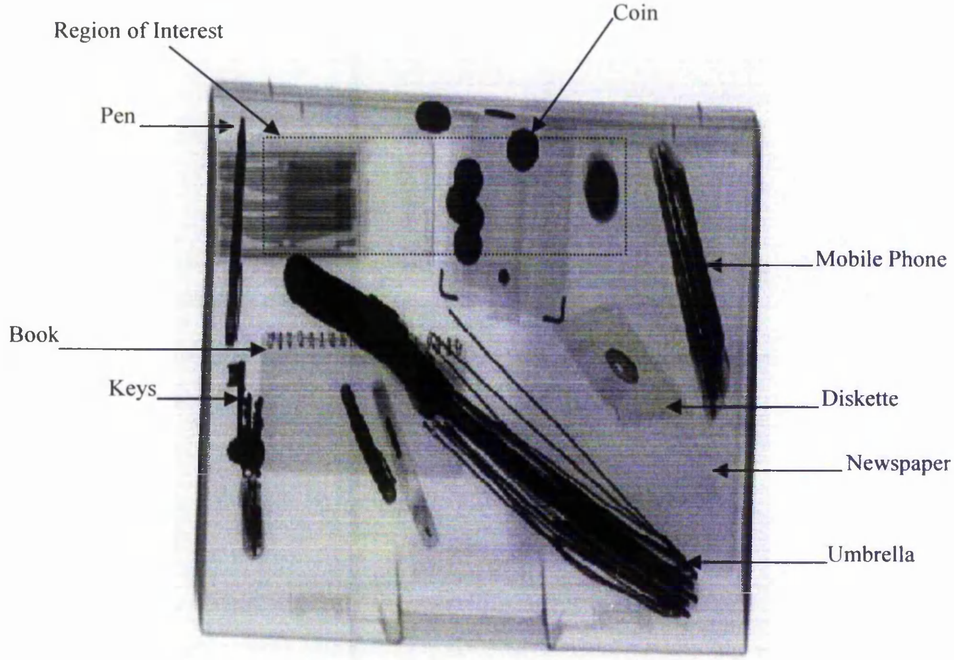

(a)

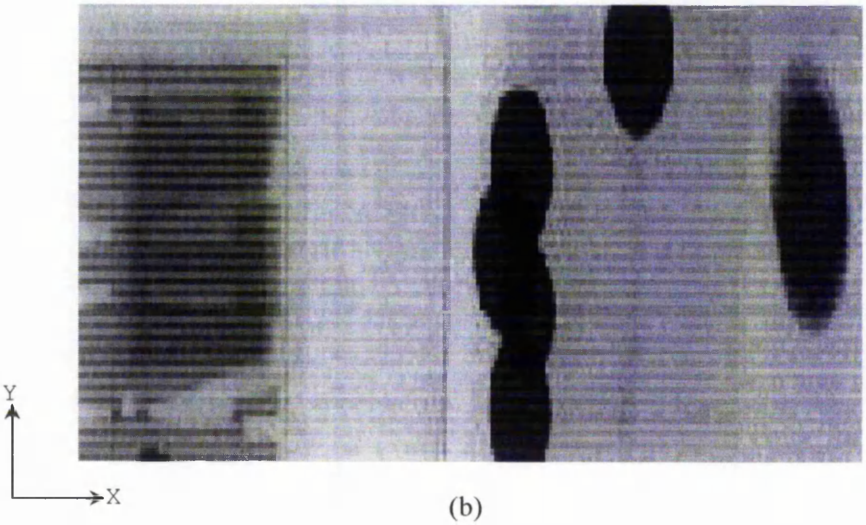

(b)

Fig. 3.4 Monochrome images of baggage sample-2 illustrating interlace noise:
(a)- Full image, (b)- Zoomed image for the region of interest depicted by the rectangle in (a).

3.3 Theoretical Analysis of De-interlacing

The spatially interleaved high energy and low energy detector elements produce a corresponding interlace effect in the resultant images. This is due to the thick and thin portions of the array producing grey level images of different brightness and contrast. Therefore, a de-interlacing algorithm is required to produce visually acceptable images.

The spatial interlace effect can be removed by averaging the alternate high energy and low energy signals. An effective grey scale image is subsequently formed having the same full resolution as a sandwich detector arrangement. Fig. 3.5 illustrates the algorithms employed to remove the interleaving effect apparent in the original image. It can be appreciated from Fig. 3.5 that adjacent pixels in the *Y*-axis are averaged to produce an effective grey level. Therefore, referring to Fig. 3.5, the effective grey level for pixel {1,1} (i.e. the top left of the de-interlaced image) is given by:

$$\frac{H_1 + L_1}{2} \times k$$

where H_1 and L_1 are the respective high energy and low energy signals obtained from the detector elements at positions H_1 and L_1 as illustrated in Fig. 3.2 on page 35.

Therefore, each pixel in the de-interlaced image is produced by applying the following image enhancement algorithm:

$$I'(x,y) = \frac{I(x,y) + I(x,\ y+1)}{2} \times k \qquad \text{Equation 3-1}$$

where $I'(x, y)$ is the grey level value for the respective pixel coordinates in *X* and *Y*-axis of the de-interlaced digital image (i.e. the array size for {*x*,*y*} is {1024x639}), I (x, y) is the grey level value in the original image and *k* is an image contrast constant. Every pair of adjacent pixels in each column is processed in this way (1024 columns in the *X*-axis). Since all pixels in the last row of the de-interlaced image (i.e. $I'(x, 640)$) have no subsequent high intensity data for the purpose of the averaging process, they are assigned the intensity value obtained from row 639 of the de-interlaced image.

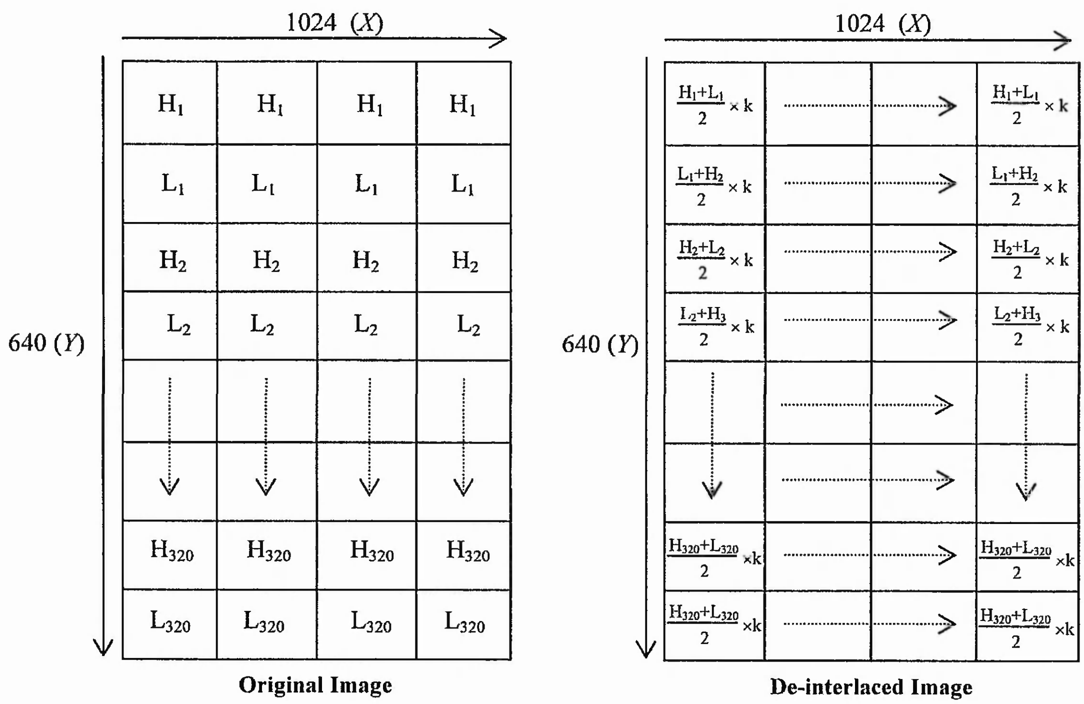

Fig. 3.5 The algorithms applied to remove spatial interlace effect.

3.4 De-interlacing Experiments

A series of experiments was devised to test the de-interlacing algorithms developed in Section 3.3. The image contrast constant *k* was also carefully examined throughout the experiments. The optimum value for k=1.2 was determined empirically. The resultant de-interlaced images are illustrated in Fig. 3.6 and Fig. 3.7. It can be appreciated from the images that the spatial interlace removal algorithms were developed successfully.

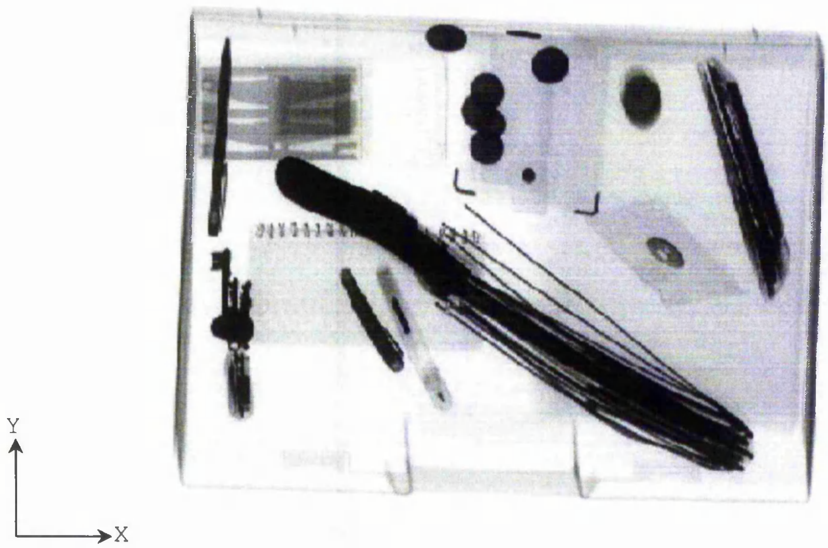

Fig. 3.6 De-interlaced monochrome image for the image shown in Fig. 3.4 on page 37.

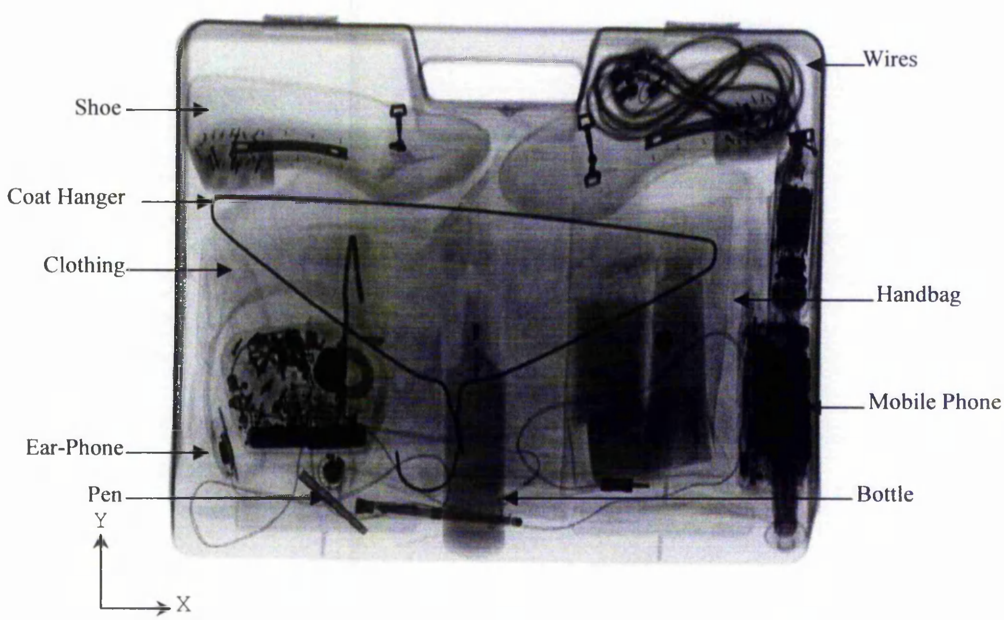

Fig. 3.7 De-interlaced monochrome image for baggage sample-3.

3.5 Theoretical Materials Discrimination Curves

The material discrimination curves illustrated in graph of Fig. 3.8 are calculated from the low energy and high energy signals generated by the thick and thin scintillator-photodiode sensors in the castellated detector array. The curves are derived by analysing the raw 12-bit grey scale high energy and low energy data acquired from the experimental dual-energy x-ray machine.

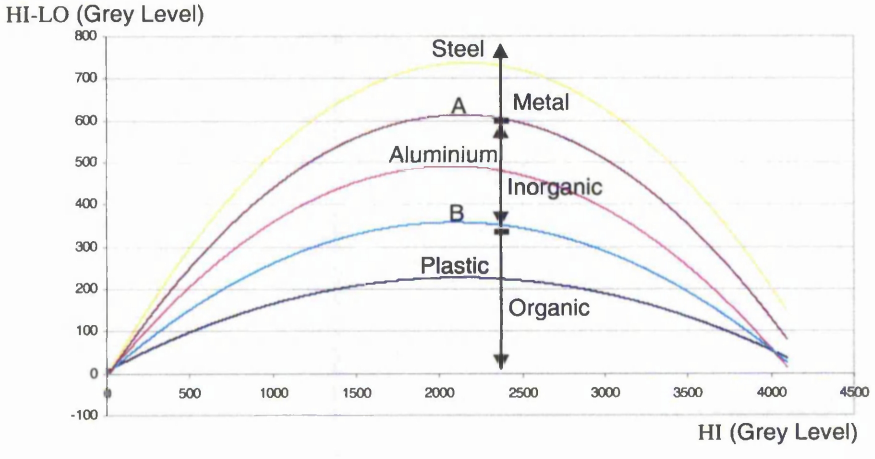

Fig. 3.8 Materials discrimination curves for the plastic, aluminium and steel stepwedges.

Referring to the spatially discrete sampling matrix depicted in Fig. 3.5 on page 39, each pair of adjacent column pixels pertaining to the high energy and the low energy signals produces a material discrimination data. For example, the materials categorisation for pixel {1,1} (i.e. the first pixel in the *X* and *Y*-axis) in the original image illustrated in Fig. 3.5 is derived by mapping the H_1 and L_1 values to the materials discrimination curves, while the materials discrimination for pixel {1,2} is processed by a similar procedure. In this way, all the pixels in the image may be colour encoded.

The raw x-ray images are originally produced in a 12-bit grey scale digital format (i.e. de-interlaced image in Fig. 3.5). This 12-bit grey scale image is converted into an 8-bit digital format and assigned to a standard industry colour palette of 24-bit RGB (red, green and blue), which indicates regions of principally organic, inorganic and metal substances in the resultant images. The established material discrimination criteria is based on the derived materials discrimination curves. The original 12-bit grey scale image has to be converted into an 8-bit digital format, because the standard colour palette utilised by the aviation security industry is based on 8-bit grey scale data. This can be appreciated from graphs in Fig. 3.9, 3.10 and 3.11. Thus, every pixel in the de-interlaced image may be assigned to the appropriate colour by employing the industry standard colour palettes illustrated in the following graphs of Fig. 3.9 for organic materials, Fig. 3.10 for inorganic and Fig. 3.11 for metal substances.

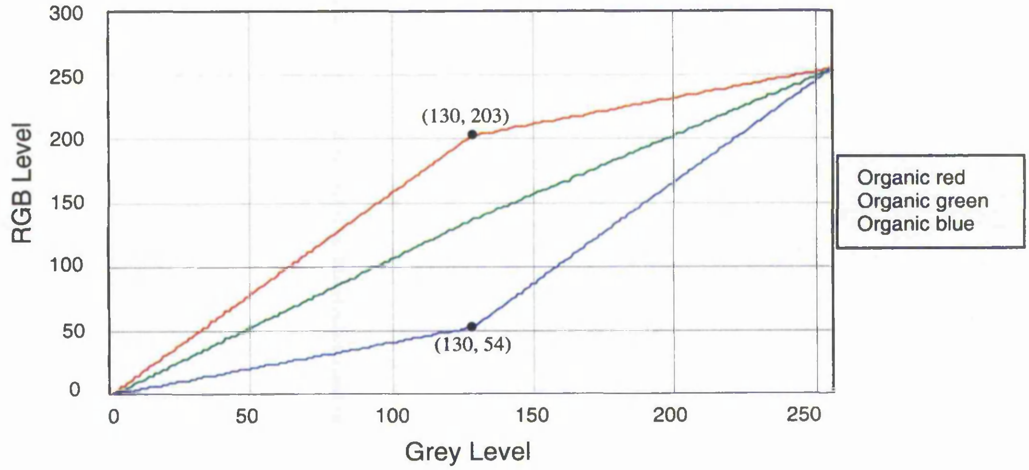

Fig. 3.9 Graph of the industry colour palette (orange) for organic substances.

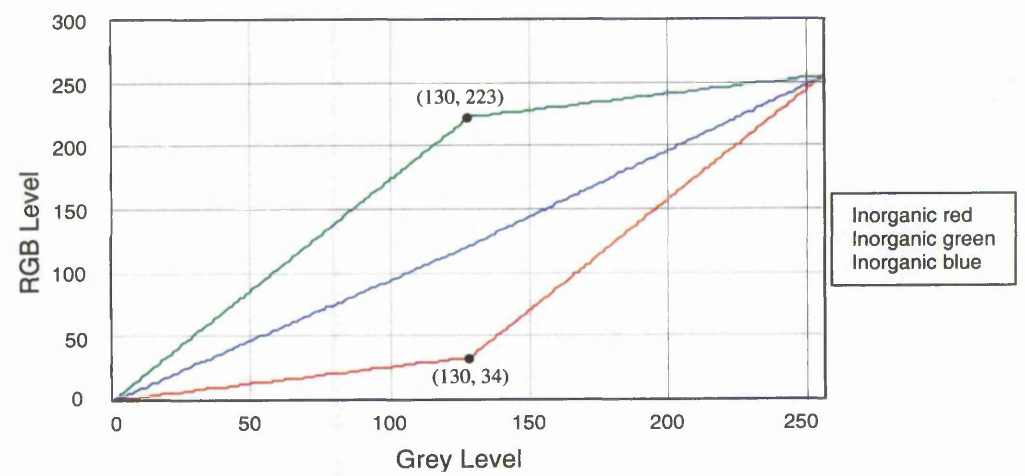

Fig. 3.10 Graph of the industry colour palette (green) for inorganic substances.

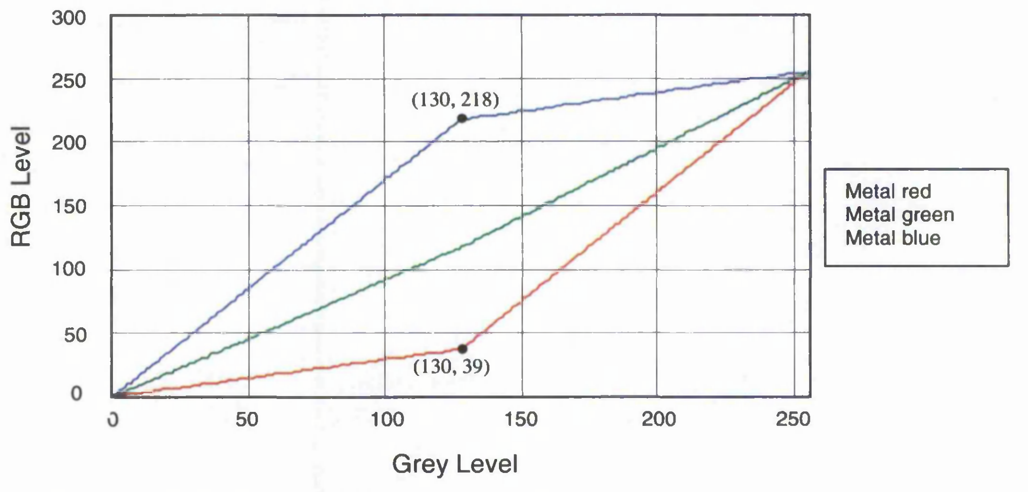

Fig. 3.11 Graph of the industry colour palette (blue) for metal substances.

3.6 Calibration for Materials Discrimination

Plastic, aluminium and steel stepwedges were utilised to calibrate the x-ray machine for organic, inorganic and metal discrimination capability. Each stepwedge was scanned and the average high (HI) and low (LO) energy signals for a 20 x 20 pixel region obtained for every step was used to plot the discrimination curves.

3.6.1 Plastic Stepwedge

Fig. 3.12 illustrates the plastic stepwedge ($H_8C_{13}O_7$, ρ = 1.4 g/cm^3, Z=6.6, each step is approximately 10 mm thick) employed in the calibration process.

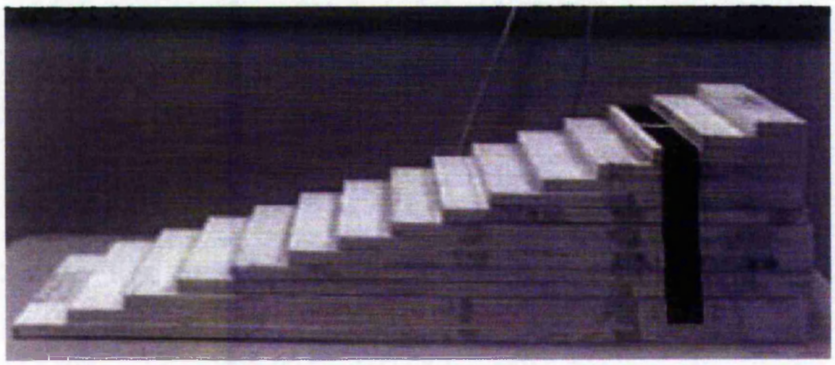

Fig. 3.12 Plastic stepwedge.

The calibration data for the plastic stepwedge is tabulated in Appendix A. The graph of transmitted HI and LO energy signal data (pixel grey levels) are plotted for each step as shown in Fig. 3.13(a). The empirical discrimination curve for the plastic stepwedge together with a smooth polynomial trend is illustrated in Fig. 3.13(b).

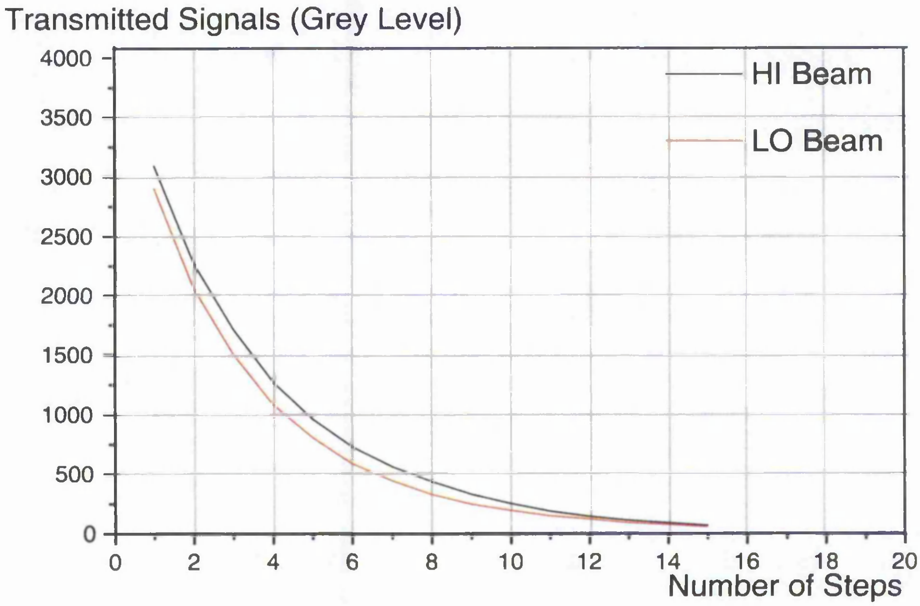

Fig. 3.13(a) Graph of the transmitted HI and LO signals against the number of plastic steps.

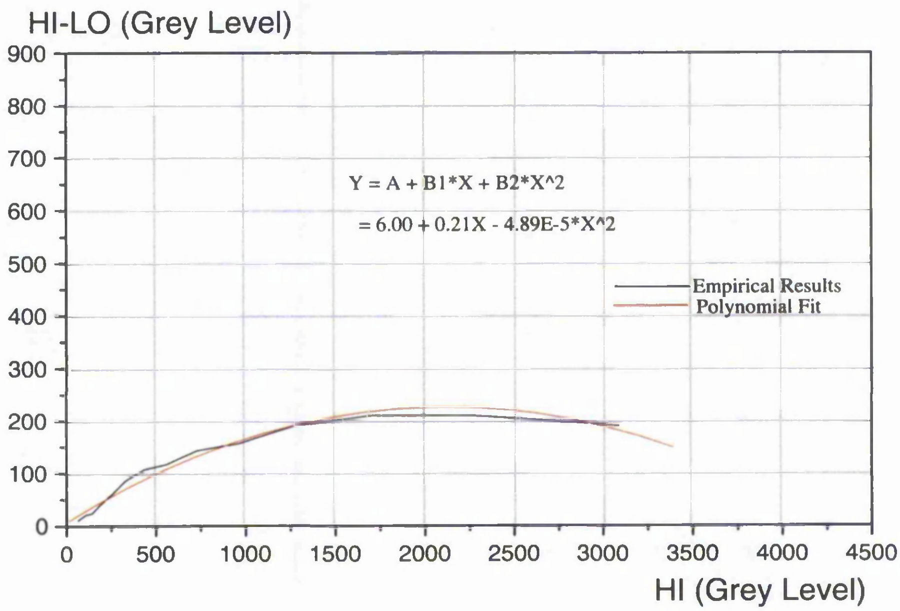

Fig. 3.13(b) The materials discrimination curve for the plastic stepwedge.

3.6.2 Aluminium Stepwedge

Fig. 3.14 shows the aluminium stepwedges (ρ = 2.702 g/cm^3, Z=13, each step is approximately 2 mm thick) utilised in the calibration process. The calibration data for the aluminium stepwedge is tabulated in Appendix A. The graph of transmitted HI and LO energy signal data (pixel grey levels) are plotted for each step as shown in Fig. 3.15(a). While Fig. 3.15(b) shows the empirical discrimination curve for the aluminium stepwedge together with a smooth polynomial trend.

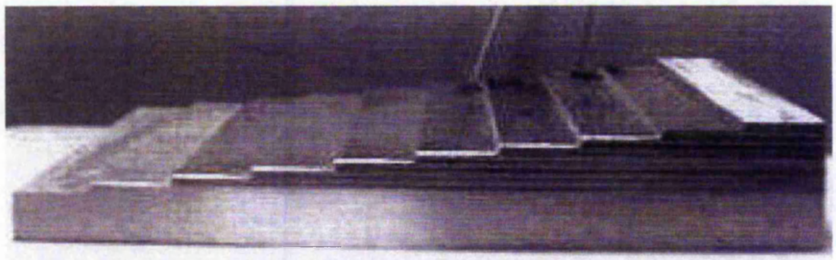

Fig. 3.14 Aluminium stepwedge.

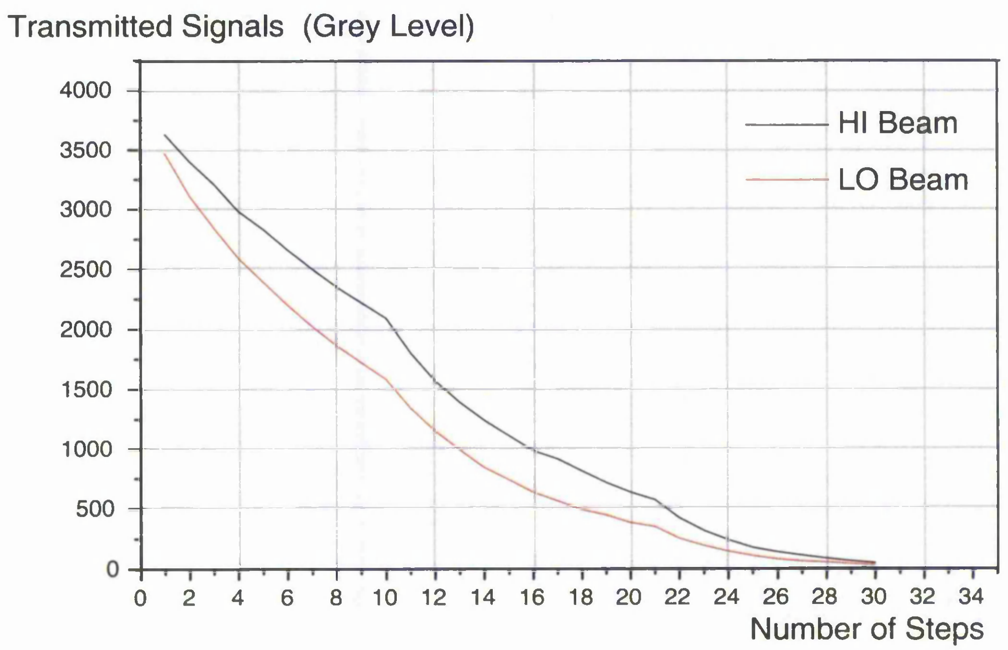

Fig. 3.15(a) Graph of the transmitted HI and LO signals against the number of aluminium steps.

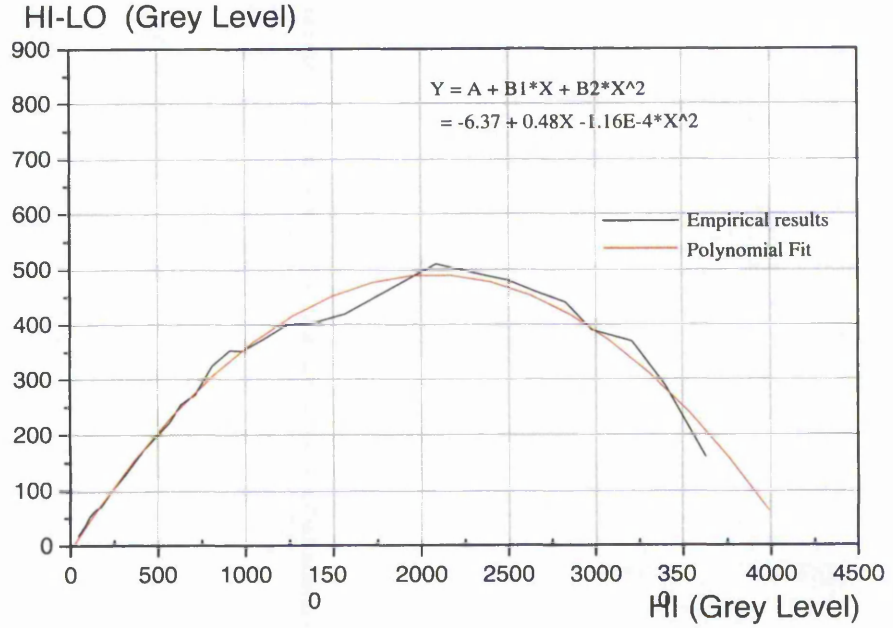

Fig. 3.15(b) The materials discrimination curve for the aluminium stepwedge.

3.6.3 Steel Stepwedge

Fig. 3.16 shows the steel stepwedge (ρ = 7.85 g/cm^3, Z=26, each step is approximately 1 mm thick) used in the calibration process. The calibration data for the steel stepwedge is tabulated in Appendix A. The graph of transmitted HI and LO energy signal data (pixel grey levels) are plotted for each step as shown in Fig. 3.17(a). The empirical discrimination curve for the steel stepwedge together with a smooth polynomial trend is illustrated in Fig. 3.17(b).

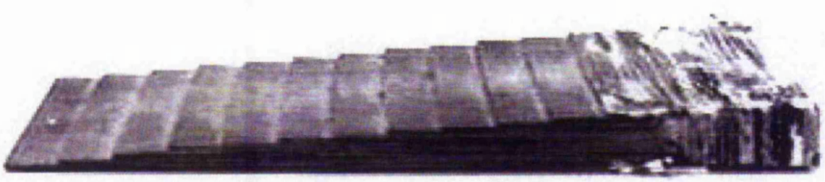

Fig. 3.16 Steel stepwedge.

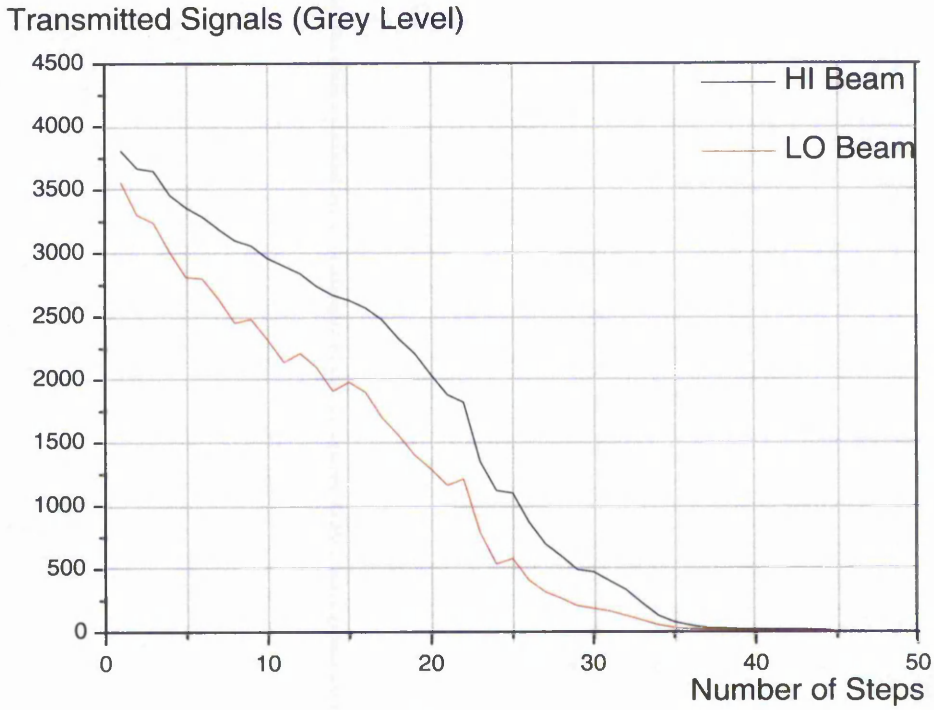

Fig. 3.17(a) Graph of the transmitted HI and LO signals against the number of steel steps.

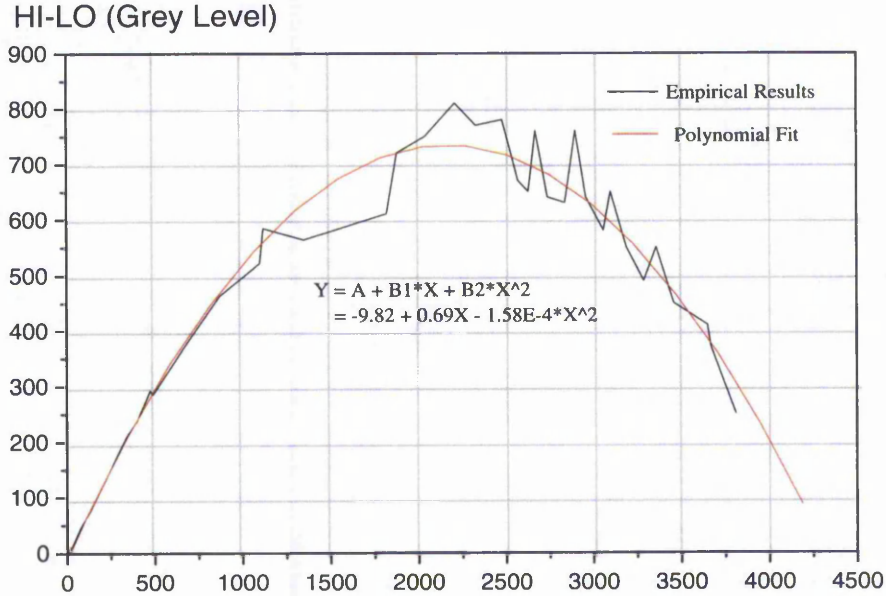

Fig. 3.17(b) The materials discrimination curve for the steel stepwedge.

3.6.4 Empirical Materials Discrimination Curves

The smoothed materials discrimination curves in Fig. 3.13(b), Fig. 3.15(b) and Fig. 3.17(b) are all plotted in the graph of Fig. 3.18(a). The mid-points in between the steel-aluminium and the aluminium-plastic curves (i.e. curves A and B shown in Fig. 3.18(b)) were derived from the polynomial fit equations for the three stepwedges shown in Fig. 3.18(a). Table B-1 of Appendix B tabulates part of the data calculated for curves A and B where remainder of the computational results are listed in the compact disc of Appendix B.

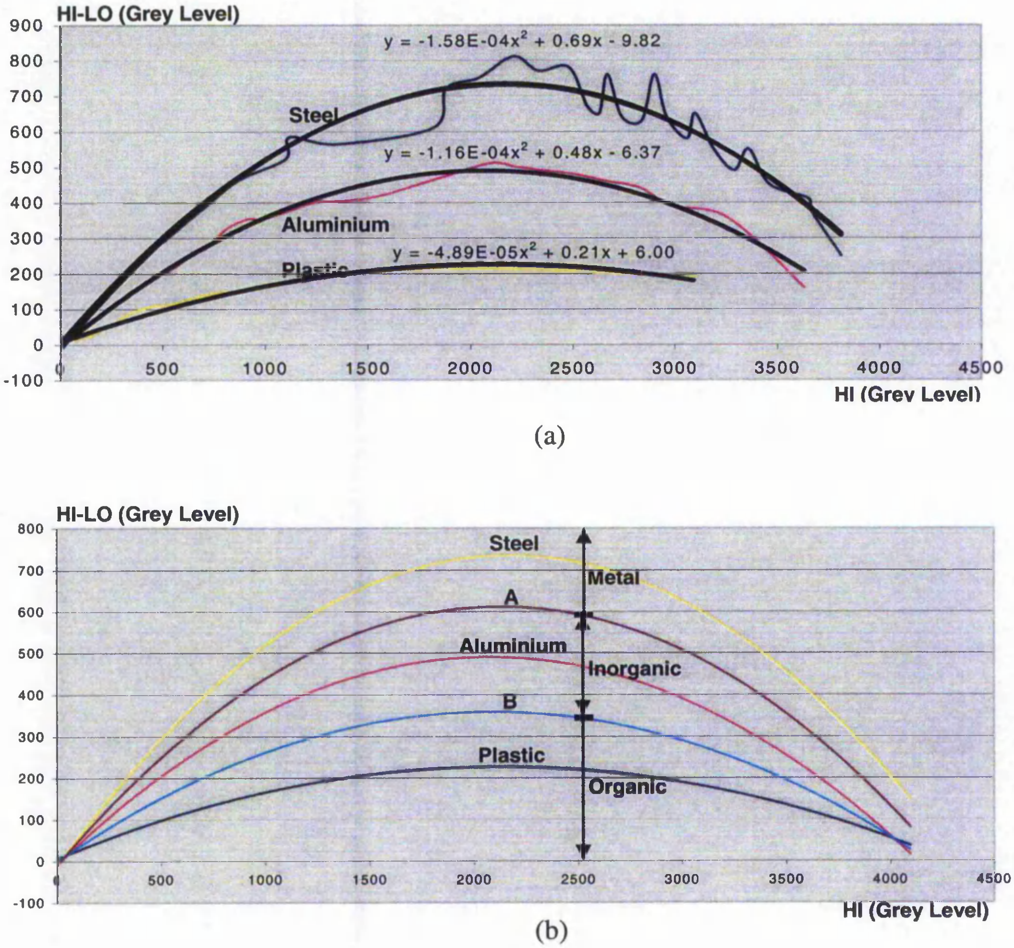

(a)

(b)

Fig. 3.18 The materials discrimination curves for the three stepwedges.

The Y-axis value for the plastic, aluminium and steel curves shown in the Table B-1 of Appendix B were computed using the polynomial fit equations below:

$Y_{plastic} = -4.89\times10^{-5}X^2 + 0.21X + 6.00,$

$Y_{aluminium} = -1.16\times10^{-4}X^2 + 0.48X - 6.37,$

$Y_{steel} = -1.58\times10^{-4}X^2 + 0.69X - 9.82.$

where X=0,1,2,....4095 for the 12-bit grey scale image.

Fig. 3.18(b) illustrates the complete polynomial fit discrimination curves showing the organic, inorganic and metal regions. The Y-axis value for curves A and B were computed using the equations below:

$Y_{Curve\ A} = (Y_{steel} - Y_{aluminium})/2 + Y_{aluminium}$

$Y_{Curve\ B} = (Y_{aluminium} - Y_{plastic})/2 + Y_{plastic}$

3.7 Materials Discrimination Experiments

A series of baggage items was screened to examine the broad materials discrimination capability of the x-ray system. This was accomplished by applying the empirical materials discrimination curves derived in previous section and the industry standard colour palette as explained earlier. The results produced by the experiments have validated the calibration procedure.

The empirical results for the material discrimination capability of the experimental x-ray machine for baggage sample-1, sample-2 and sample-3 are illustrated in Fig. 3.19, Fig. 3.20 and Fig. 3.21 respectively.

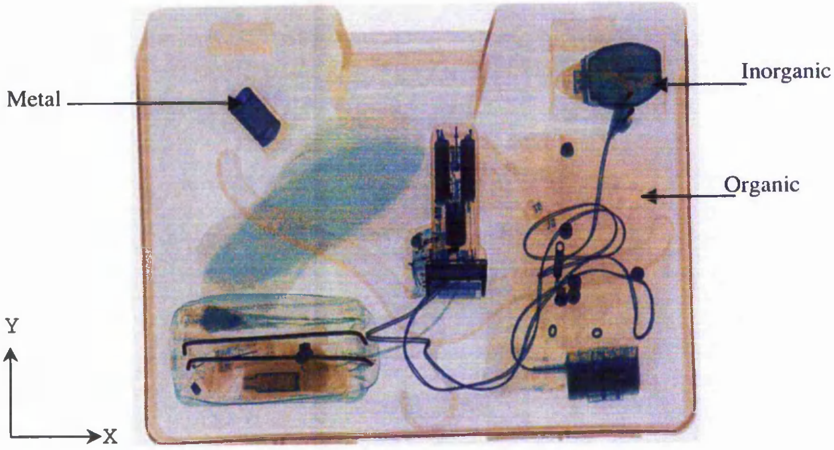

Fig. 3.19 Colour encoded image of baggage sample-1.

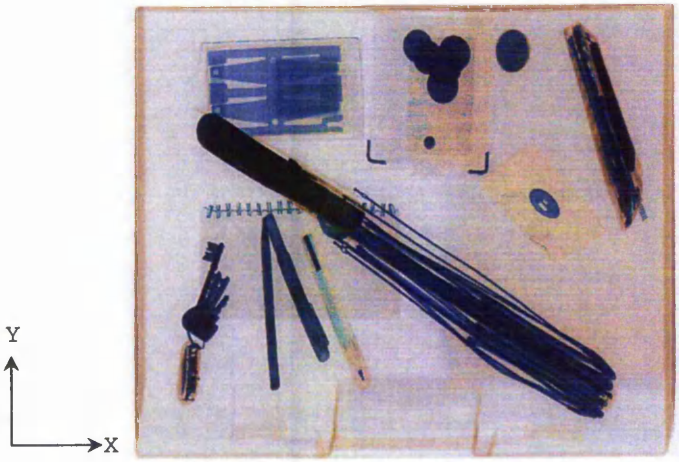

Fig. 3.20 Colour encoded image of baggage sample-2.

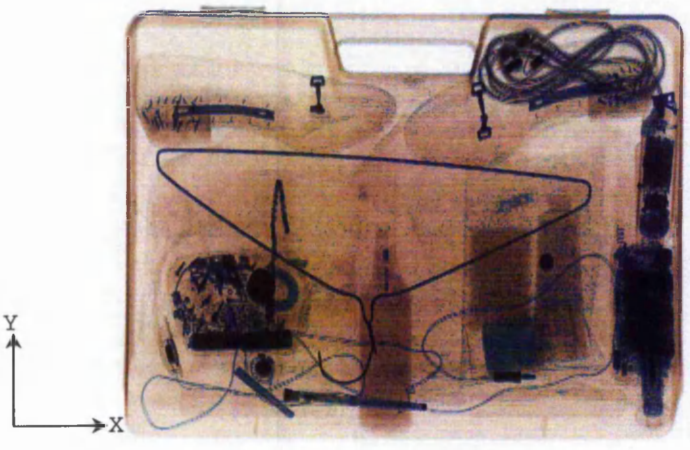

Fig. 3.21 Colour encoded image of baggage sample-3.

3.8 Experiments on System Noise

The analysis of the bright field images (i.e. blank peak white signal images) was conducted to evaluate the noise generated by the whole image acquisition chain of the experimental x-ray system.

Fig. 3.22 illustrates the segregation of the low energy and the high energy images from the original interlaced image. Experiments were carried out to examine each of the pixel columns (i.e. 320 pixel counts in the *Y*-axis) in the low energy and the high energy images.

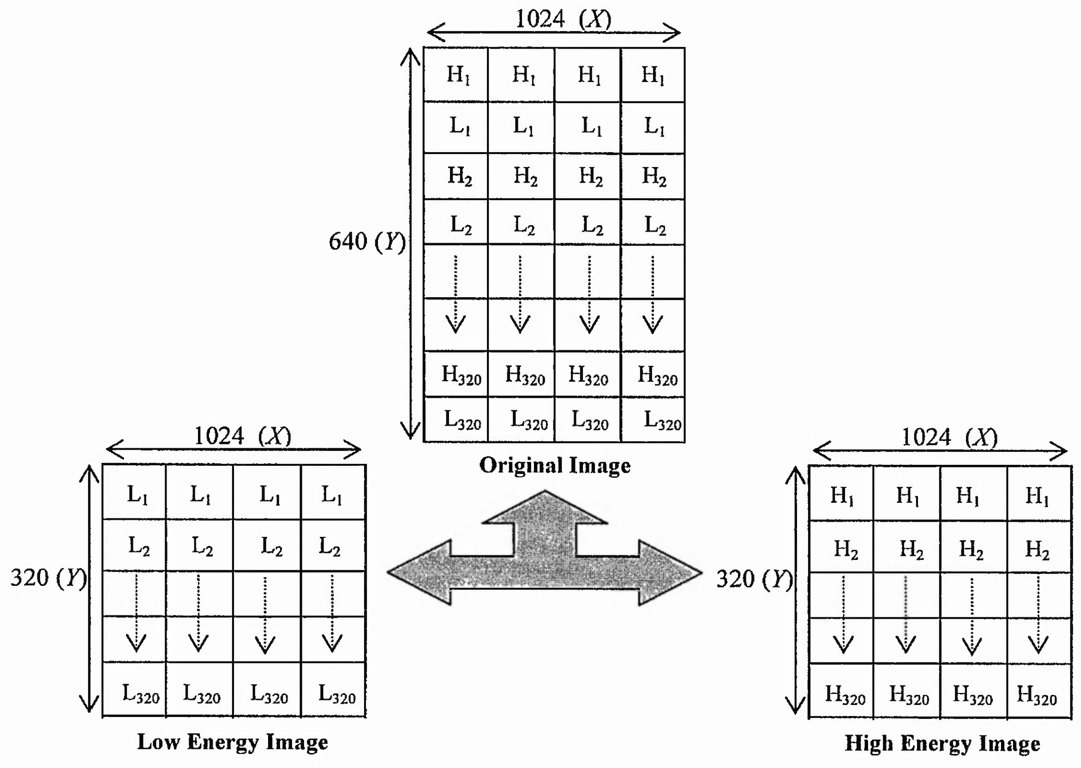

Fig. 3.22 The segregation of the low energy and the high energy images from the original interlaced image.

The theoretical bright field signals for the low energy and the high energy images should ideally exhibit a constant maximum value (i.e. 4095 for a 12-bit grey scale digital image). The experimental results for the noise analysis of the low energy and the high energy images for both the left and right imaging channels (i.e. stereoscopic image pairs) are shown in Fig. 3.23, through to Fig. 3.26. The analysis utilised five adjacent pixel columns (i.e. from X=1 to 5 or pixel column 1 to 5) from each of the low energy and the high energy images. The grey level intensity for every pixel count (i.e. from Y=1 to 320) is plotted in the graphs.

High Energy Data for the Left Perspective Imaging Channel

The noise analysis of the high energy data for the left perspective image is illustrated in graphs plotted in Fig. 3.23 and Fig. C-1 in Appendix C. They are plotted with data obtained from five pixel columns. The standard deviation is of the order of ±49.4 with respect to the mean value of 4063.1.

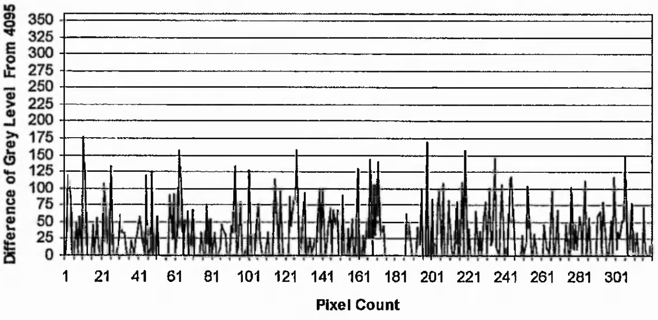

Fig. 3.23 Graph of the noise analysis for the high energy data for the left perspective imaging channel: pixel column 1.

Low Energy Data for the Left Perspective Imaging Channel

The noise analysis of the low energy data for the left perspective image is illustrated in graphs plotted in Fig. 3.24 and Fig. C-2 in Appendix C. They are plotted with data obtained from five pixel columns. The standard deviation is of the order of ±45.1 with respect to the mean value of 4064.4.

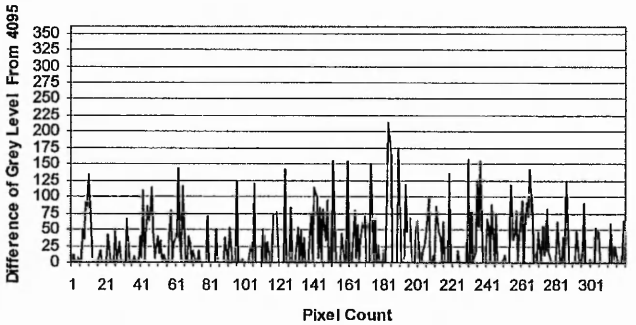

Fig. 3.24 Graph of the noise analysis for the low energy data for the left perspective imaging channel: pixel column 1.

High Energy Data for the Right Perspective Imaging Channel

The noise analysis of the high energy data for the right perspective image is illustrated in graphs plotted in Fig. 3.25 and Fig. C-3 in Appendix C. They are plotted with data obtained from five pixel columns. The standard deviation is of the order of ±46.9 with respect to the mean value of 4064.4.

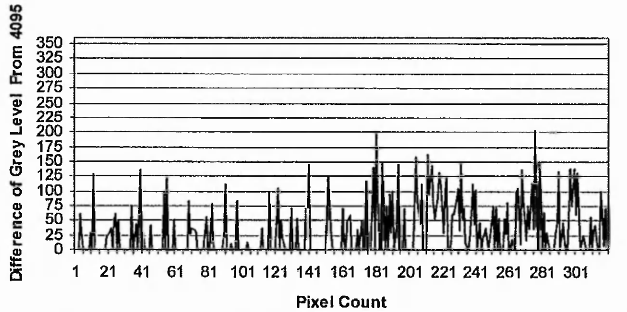

Fig. 3.25 Graph of the noise analysis for the high energy data for the right perspective imaging channel: pixel column 1.

Low Energy Data for the Right Perspective Imaging Channel

The noise analysis of the low energy data for the right perspective image is illustrated in graphs plotted in Fig. 3.26 and Fig. C-4 in Appendix C. They are plotted with data obtained from five pixel columns. The standard deviation is of the order of ±41.4 with respect to the mean value of 4070.5.

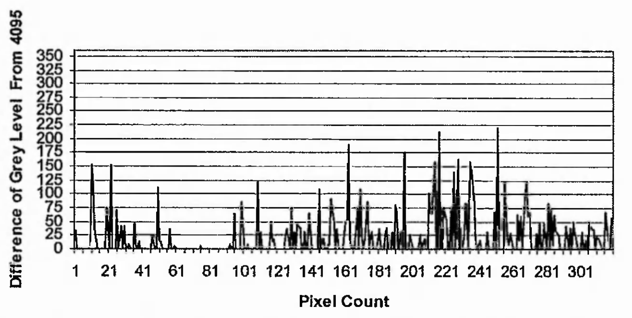

Fig. 3.26 Graph of the noise analysis for the low energy data for the right perspective imaging channel: pixel column 1.

The maximum standard deviation from this series of experiments is ±49.4 from a mean value of 4063.1. Generally, these results are reasonable and indicates that the x-ray source is capable of producing a comparatively constant output.

3.9 Experiments on System Repeatability

A series of experiments to establish system repeatability was conducted. A set of six nominally identical *T-shape* metal objects but with different thickness were scanned 6 times. The purpose of this experiment is to ascertain whether the average grey level intensity for a set of metal objects remains constant for successive scans.

The physical arrangement of the metal objects was scanned 6 times (M_a, M_b, M_c, M_d, M_e and M_f) as shown in Fig. 3.27.

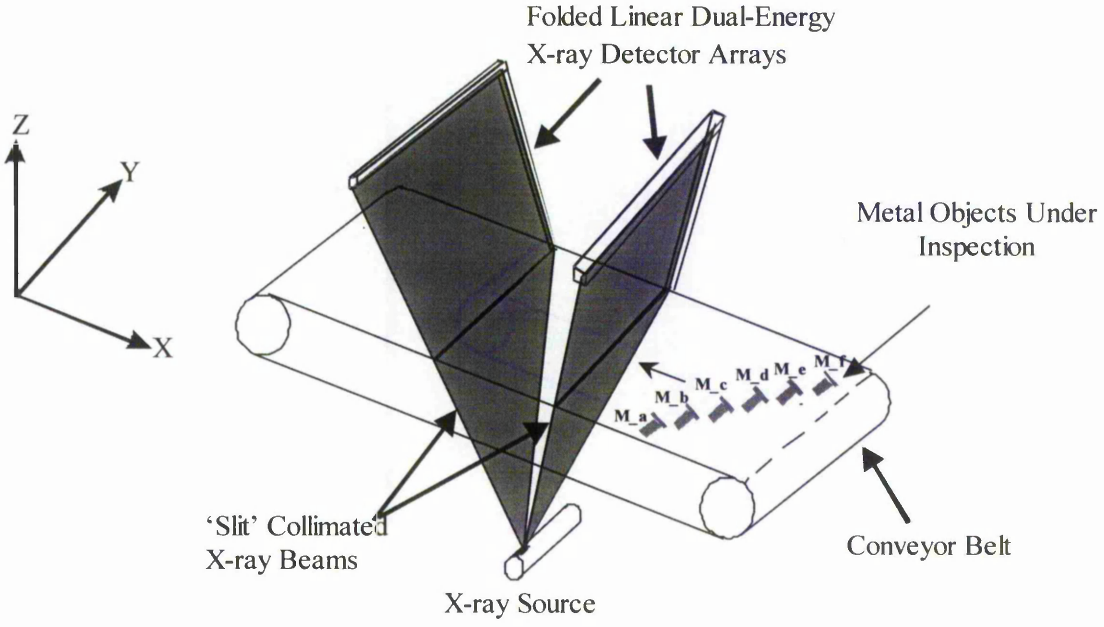

Fig. 3.27 The physical arrangement of the metal objects on the conveyor belt of the experimental system.

Fig. 3.28 illustrates the resultant monochrome high energy and low energy x-ray images (12-bit grey level) for the metal objects.

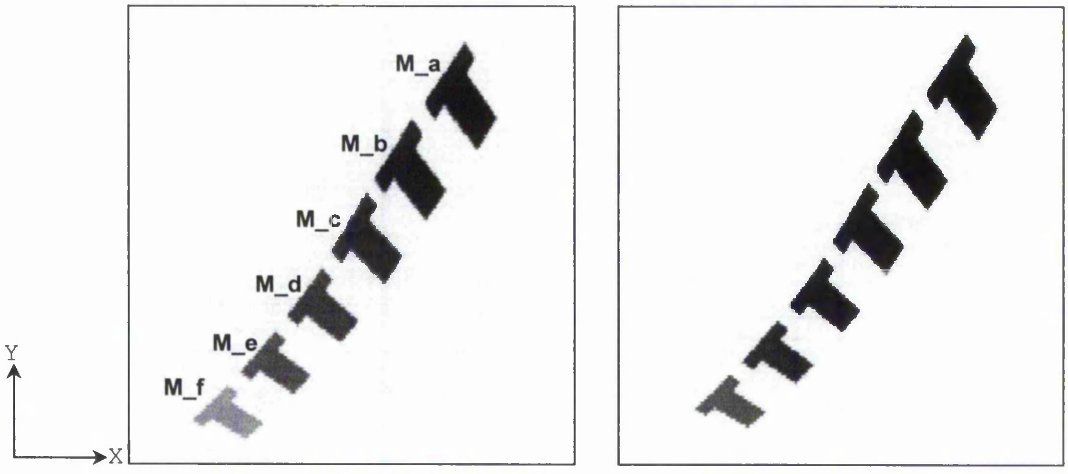

High Energy Image **Low Energy Image**

Fig. 3.28 The monochrome x-ray images for the metal objects arranged as shown in Fig. 3.27.

Table 3-1(a), (b), ...(f) tabulate the average grey level (i.e. average of a 20 x 20 pixel region) for each metal object (M_a, M_b, ...M_f) for the left perspective high energy and low energy images (left HI & left LO), and also for the right perspective high energy and low energy images (right HI & right LO). The average value and the standard deviation (SD) for each data set are calculated. Since the metal objects have uniform thickness, the average grey level was computed for any 20 x 20 pixel portion within each imaged object.

M_a	L LO	L HI	R LO	R HI
1	1888	2661	1919	2553
2	1888	2672	1921	2556
3	1887	2656	1918	2540
4	1885	2664	1926	2553
5	1884	2663	1921	2551
6	1888	2668	1927	2562
Average	1886.7	2664	1922	2552.5
SD	±1.8	±5.6	±3.7	±7.2

Table 3-1(a)

M_b	L LO	L HI	R LO	R HI
1	1194	1970	1198	1948
2	1195	1973	1204	1960
3	1192	1966	1195	1947
4	1198	1974	1200	1958
5	1194	1972	1196	1949
6	1197	1976	1198	1955
Average	1195	1971.8	1198.5	1952.8
SD	±2.2	±3.5	±3.2	±5.6

Table 3-1(b)

M_c	L LO	L HI	R LO	R HI
1	858	1537	895	1525
2	855	1536	897	1526
3	853	1527	894	1519
4	860	1536	897	1527
5	858	1534	900	1525
6	859	1538	902	1530
Average	857.2	1534.7	897.5	1525.3
SD	±2.6	±4.0	±3.0	±3.6

Table 3-1(c)

M_d	L LO	L HI	R LO	R HI
1	663	1226	688	1224
2	665	1225	690	1231
3	662	1221	688	1225
4	663	1222	688	1230
5	663	1226	685	1227
6	664	1226	687	1233
Average	663.3	1224.3	687.6	1228.3
SD	±1.0	±2.3	±1.6	±3.6

Table 3-1(d)

M_e	L LO	L HI	R LO	R HI
1	328	724	337	720
2	325	721	340	727
3	325	723	337	719
4	326	723	339	722
5	328	728	339	722
6	324	725	339	725
Average	326	724	338.5	722.5
SD	±1.7	±2.4	±1.2	±3.0

Table 3-1(e)

M_f	L LO	L HI	R LO	R HI
1	215	476	210	494
2	211	473	208	494
3	213	474	207	492
4	210	474	207	493
5	213	477	209	493
6	210	472	209	494
Average	212	474.3	208.3	493.3
SD	±2.0	±1.9	±1.2	±0.8

Table 3-1(f)

It can be deduced from Table 3-1 that the maximum standard deviation of ±7.2 or better can be achieved.

3.10 Summary

The empirical results indicate that the calibration for the castellated detector array in terms of spatial interlace removal and broad materials discrimination capability are acceptable for visual inspection purposes. Additionally, the experimental results for the system noise and the system repeatability are also generally acceptable.

The experimental results have proved the capability of the castellated detector array in producing monochrome and colour images with comparable visual quality to the conventional approach utilising sandwich detector arrays. However, material discrimination for a single sample (i.e. one pixel) is not achievable with the castellated arrangement. It can be appreciated from Fig. 3.2 on page 35 that the associated x-ray beam paths for the adjacent pixels are slightly different. Therefore, the LO and HI energy signal weightings could be untrue for a pixel size material element. Consequently, this may also effect the material discrimination at the edges of the objects under inspection as illustrated in Fig. 3.29 (i.e. the encoded green and brown colours at the edges of the metal keys).

Nevertheless, the size of threat objects such as explosives in a security screening application will be very large in comparison to single pixel sample. Therefore, the detector array will produce sufficiently high spatial resolution together with materials discrimination capability.

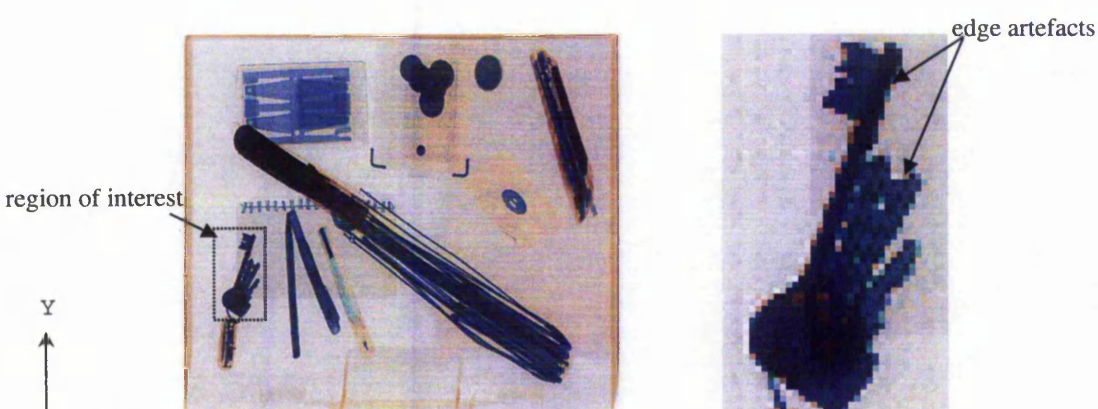

(a) (b)

Fig. 3.29 Baggage sample-2: (a)-Colour image, (b)-Zoomed image of a region of interest in (a) depicting edge artefacts produced by the castellated detector.

The noise analysis indicates that a maximum standard deviation of the order of ±49.4 is produced by the detector element with respect to the mean value of 4063.1. While, the system repeatability test indicated a maximum standard deviation of the order of ±7.2. Generally, these results are reasonable where the resultant grey levels for each successive object scan is within acceptable visual limits. However, the accuracy of the technique developed to detect target materials (described in Chapter 5) is affected by small deviations in system noise and system repeatability[C6]. Therefore, small systematic errors which are not visually significant may result in incorrect target material discrimination when data is quantitatively processed by the techniques presented in the following chapters.

It is strongly believed that the system x-ray source is not sufficiently stable to provide a constant x-ray flux at all times and thus it contributes to the majority of the system noise. Therefore, a more stable type of x-ray source is required to provide a more accurate target material detection performance as investigated in the following chapters.

Additionally, the problem of non-uniform sensor response will also affect the accuracy of the low energy and high energy x-ray transmission signals[F5, K3, L6, T5]. The potential performance of the Thallium doped Caesium Iodide detector (CsI(Tl)) is limited by its long decay time and also its wide variation in afterglow where its afterglow figures is of the order of 0.5 to 5.0% after 6ms[L1]. Afterglow is quoted as a percentage of the emitted light signal intensity at a given time interval after x-rays excitation has ceased. The relatively large variation in afterglow can create large variations in x-ray intensity measurements between individual detector elements in an array. As a result, the detected dual energy signals may vary.

Thus, an ideal scintillator for the purpose of security screening requires the following important features:

- high efficiency for converting x-rays into light signals;
- linear conversion of x-rays into light signals (i.e. emitted light signals is proportional to the deposited x-ray energy);
- short decay time to permit fast sampling of the generated light signals.

Generally, the results obtained from the empirical analysis have proved the validity of the castellated sensor in terms of broad materials discrimination performance. Therefore, this would seem a reasonable result for the purposes of the further investigations reported in Chapter 5 and 6.

The scattered photons are neglected in this research. It is assumed that the distance between the object under inspection and the detectors is long, and the proper slit collimation of the x-ray source and the detector will reduce the scattering effect to negligible levels. Additionally, the application of the mathematical algorithms in the following chapters assumes that the system x-ray spectrum does not change with time. However, the x-ray spectra will randomly fluctuate in practice and will lead to significant error in the calculations.

CHAPTER FOUR

AUTOMATED X-RAY IMAGE SEGMENTATION

4.1 Introduction

This chapter describes the development of an automated image segmentation program to isolate grey level information relating to different layers of baggage contents. This process is a precursor to the investigation of the extraction of the characteristic angle (i.e. effective atomic number) and mass density of overlapping object structures in the resultant images. The mathematical algorithms implemented to extract the characteristic angle and mass density from each successfully segmented layer of overlapping materials are discussed in Chapter 5 and Chapter 6 respectively.

This chapter discusses the following two areas:

- The development of an automated image segmentation program using the wavelet transform.
- The development of automated image categorisation algorithm.

Initially, an automated image segmentation program utilising the wavelet transform technique is applied to segment the overlapping objects in an x-ray image into individual regions or objects.

The work is expanded to extract the low energy and the high energy data for each successfully segmented region in the digital x-ray image. This enables an automated 'overlapping image' categorisation algorithm to be developed. Thus, the segmented regions in an x-ray image can be further categorised into overlapping and non-overlapping objects.

4.2 Automated Image Segmentation using the Wavelet Transform

The wavelet transform technique originally developed by Jean-Christophe Olivo and Stephane Mallat is employed in an automated segmentation program. This technique is based on the detection of the zero-crossings of a wavelet transform when applied to the grey level histogram of the resultant images. In this way, cluster's of pixels with similar grey levels values may be identified and treated as discrete object features. Of particular interest in this work is the delineation of multiple layers of different material types. Therefore, the concept that different configurations of overlapping materials will produce distinct changes in grey level distribution is used, under certain conditions, to extract the grey levels attributable to the individual layers or composite layers.

The flow chart for the automated image segmentation algorithm is illustrated in Fig. 4.1. Initially, the low energy and the high energy x-ray image data is filtered to reduce noise. A median filter employing a 3x3 neighbourhood was identified as having appropriate properties in terms of fast computation time and suppression of impulsive noise while preserving edges[H10].

In this research, only the low energy x-ray image is utilised in the image segmentation process. However, the high-energy image would have been equally applicable for this purpose.

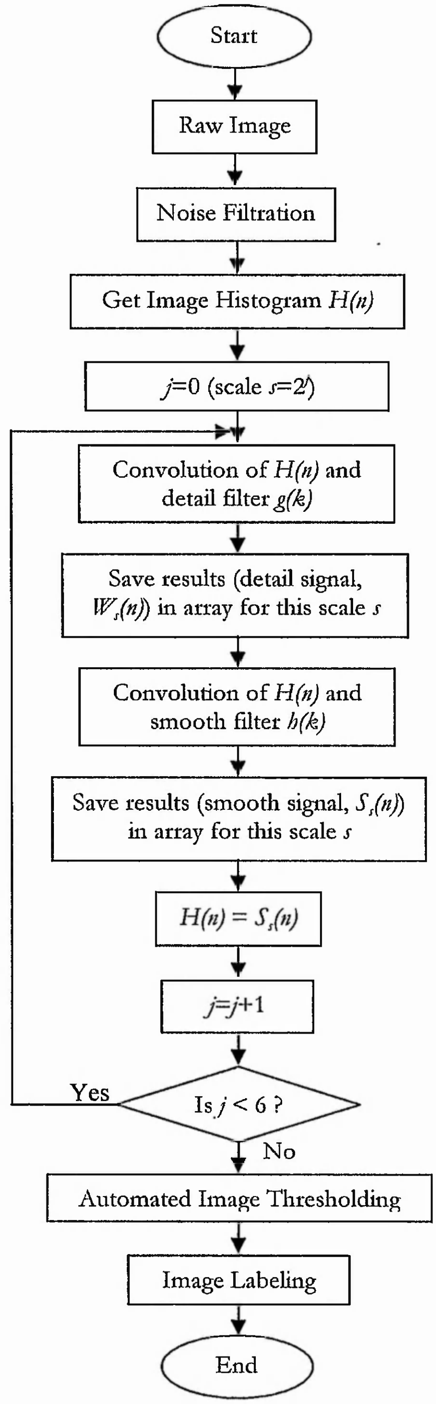

Fig. 4.1 Flow chart for the automated image segmentation program.

A histogram $H(n)$ of the filtered low energy x-ray image is initially obtained. The first wavelet scale s=1 (2^0) is initialised by setting the integer value of j to 0. This is followed by the convolution of the detail wavelet filter $g(k)$ and the image histogram

$H(n)$. The result of this convolution is the detail signal ($W_s(n)$) which is stored in an array.

Convolving $H(n)$ with $g(k)$ computes the total average of the neighbour's intensity of each grey level with the function $g(k)$. As j=0, the convolution is carried out on the neighbours in the interval of s=1 (2^0). When the scale s increases, the convolution is then conducted on the neighbours of each grey level at larger intervals. This therefore explains that the smaller the scale s, the finer the details of the x-ray image that are processed.

The original histogram $H(n)$ is then convolved with the smooth filter $h(k)$ and the result of this convolution which is the smooth signal ($S_s(n)$) is saved in another array. The histogram $H(n)$ is replaced with the new values obtained from the smooth signal $S_s(n)$. This implies that the original x-ray image is smoothed by the smooth filter $h(k)$ and the new histogram data $H(n)$ is convolved again with filters $g(k)$ and $h(k)$ in the next loop at larger scale $s=2^1, 2^2 \ldots 2^5$. All the results of the detail and smooth signal at each scale s are saved in arrays independently.

The automated image thresholding algorithm can be subsequently derived from the results obtained by the wavelet analysis. This is performed by choosing the zero-crossing points from the detail signal $W_s(n)$ at any desired scale s $(s=2^j)$. The detected zero-crossing points are applied for the automatic selection of a set of thresholds describing every segmented region in the x-ray image. Finally, all of the successfully segmented regions (i.e. which can be interpreted as homogeneous grey level areas representing the whole original image) are labelled for next phase of analysis (i.e. automated image categorisation program).

The empirical results shown in Fig. 4.3 best illustrate the detail graphical representation of wavelet transform (i.e. image histogram $H(n)$, detail signal $W_s(n)$ and smooth signal $S_s(n)$) for a segmented x-ray image.

4.2.1 Limitations

The limitation of the wavelet analysis is that unsuccessful segmentation can occur when the region of interest in an x-ray image is small compared to the background or when both the region of interest and the background have a broad range of grey levels[M5, O2].

Therefore, overlapping substances can only be delineated provided that each layer has a discernable shape that can be segmented. As a result, a thin sheet of plastic explosive (≈2 to 5 mm) which is almost transparent in an x-ray image would still present an extremely difficult/impossible scenario.

4.2.2 Experimental Results

A series of experiments has been conducted to evaluate the automated image segmentation algorithm to delineate overlapping objects in the resultant x-ray images. The best wavelet scale s suitable for the segmentation of 'typical' baggage contents is concluded as: $s=2^2$.

Baggage Sample-5

Fig. 4.2 illustrates every region (object) in baggage sample-5 (i.e. Fig. 4.2(a)) with uniform intensity is successfully segmented and represented in different colours as illustrated in Fig. 4.2(b) to Fig. 4.2(f) for wavelet scale $s=2^1$ to 2^5. It can be appreciated that as the scale s reduces the segmented areas increase in number. It can also be deduced from the images in Fig. 4.2 that the best wavelet scale s for the segmentation of baggage sample-5 is 2^2.

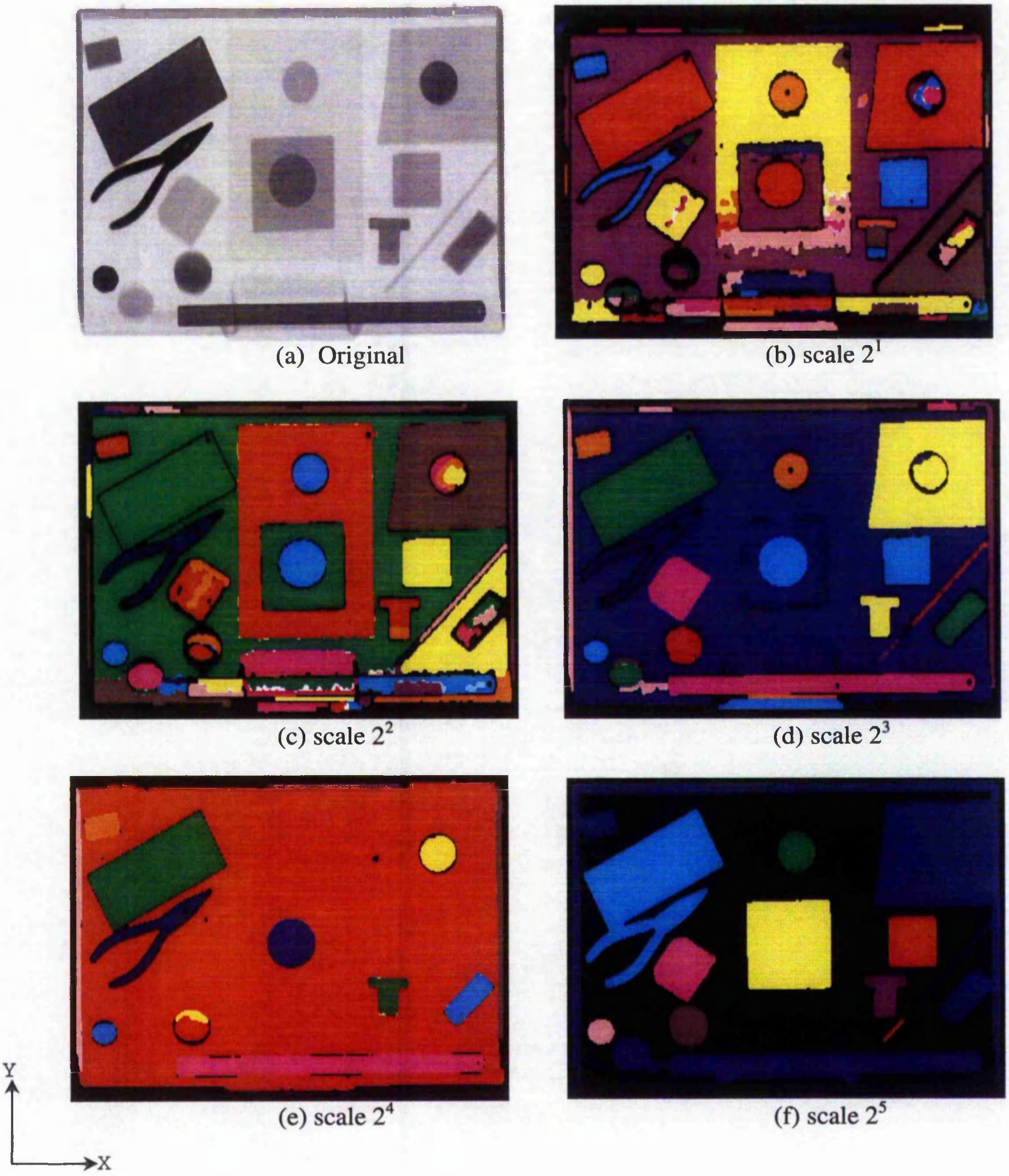

Fig. 4.2 (a)- Original monochrome low energy x-ray image of baggage sample-5, (b)- segmented image at scale 2^1, (c)- segmented image at scale 2^2, (d)- segmented image at scale 2^3, (e)- segmented image at scale 2^4, and (f)- segmented image at scale 2^5.

Fig. 4.3 shows the graphs plotted with the number of pixels versus the respective grey levels (i.e. grey levels from 1 to 91) for baggage sample-5. It can be appreciated from the graphs that the zero-crossing points for the detail signal W_s at a larger scale s is not accurate when compared to the original histogram H. This is due to the fact that at a larger scale s, the smooth signal S_s becomes coarser and crudely approximates the original histogram.

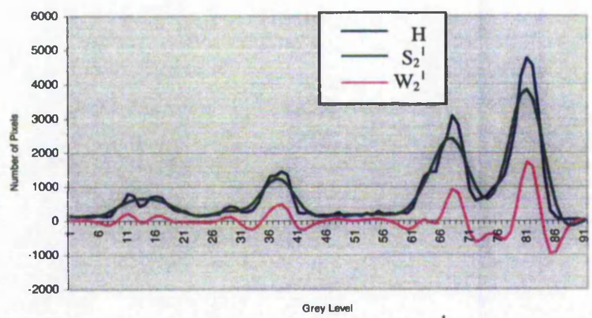

(a) scale 2^1

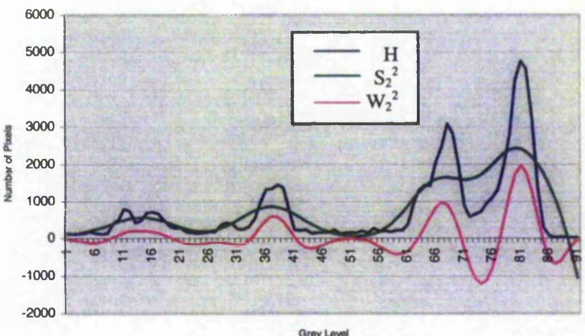

(b) scale 2^2

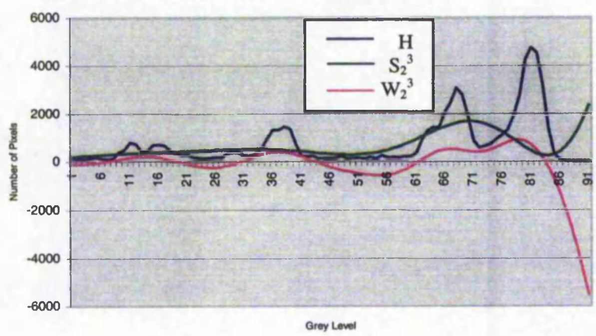

(c) scale 2^3

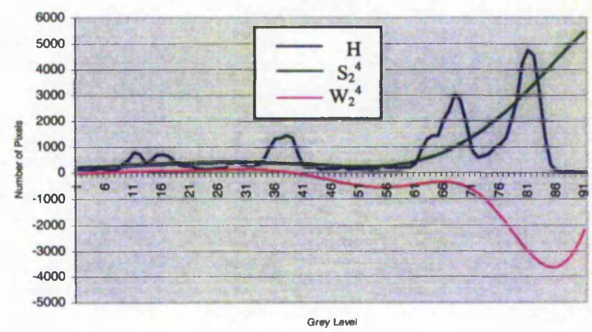

(d) scale 2^4

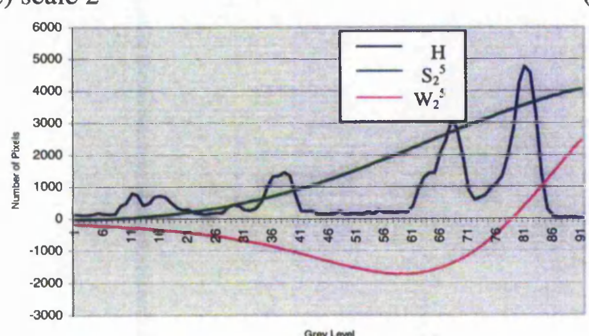

(e) scale 2^5

Fig. 4.3 Finite scale wavelet transform representation of baggage sample-5 (Fig. 4.2(a)) for scales $s=2^1, \ldots, 2^5$. In the corresponding figures (a)-(e), the original image histogram H, the smooth signal S_s, and the detail signal W_s are plotted at every scale s.

Baggage sample-6

Fig. 4.4 illustrates that the objects in baggage sample-6 exhibiting uniform intensity are successfully segmented and represented in different colours for wavelet scale $s=2^2$.

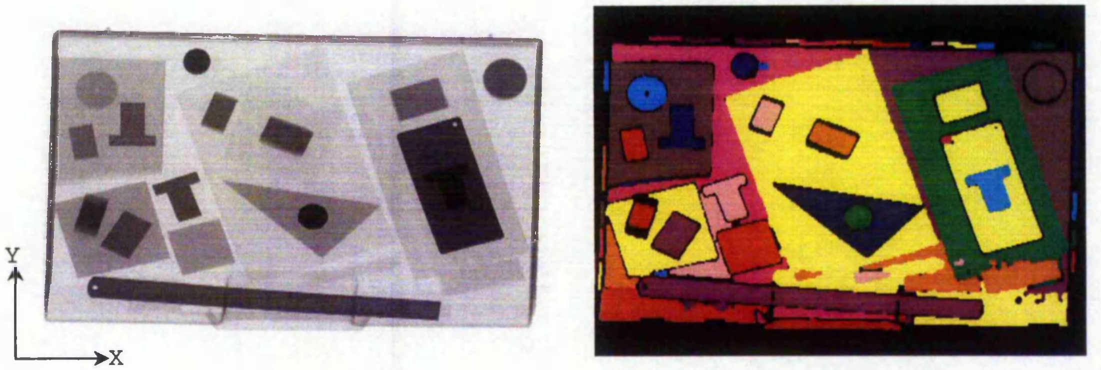

(a) Original (b) scale 2^2

Fig. 4.4 (a)- Original monochrome low energy x-ray image of baggage sample-6 and (b)- segmented image at scale 2^2.

Baggage sample-7

Fig. 4.5 illustrates that the objects in baggage sample-7 exhibiting uniform intensity are successfully segmented for wavelet scale $s=2^2$.

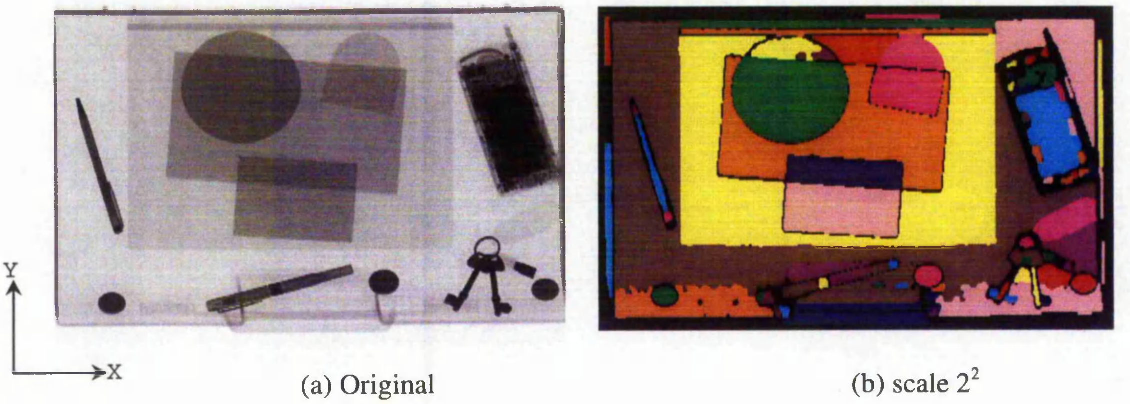

(a) Original (b) scale 2^2

Fig. 4.5 (a)- Original monochrome low energy x-ray image of baggage sample-7 and (b)- segmented image at scale 2^2.

Baggage sample-3

Fig. 4.6 illustrates objects in baggage sample-3 with non-uniform intensity are segmented into many individual regions represented in different colours for wavelet scale $s=2^2$ and $s=2^3$. It can be appreciated from the results that there are many successfully segmented regions for both wavelet scales $s=2^2$ and $s=2^3$. This approach requires intensive image processing and may not be appropriate for real time applications.

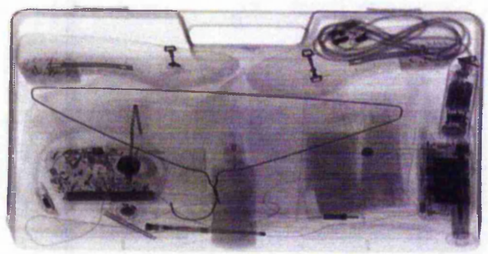

(a) Original

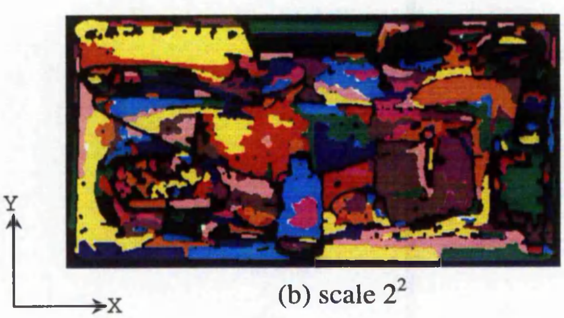

(b) scale 2^2

(c) scale 2^3

Fig. 4.6 (a)- Original monochrome low energy x-ray image of baggage sample-3, (b)- segmented image at scale 2^2 and (c)- segmented image at scale 2^3.

Baggage sample-4

Fig. 4.7 illustrates objects in baggage sample-4 with non-uniform intensity are successfully segmented into individual regions for wavelet scales $s=2^2$ and $s=2^3$. Hence, it requires intensive image processing and the result is unsuitable for real time application.

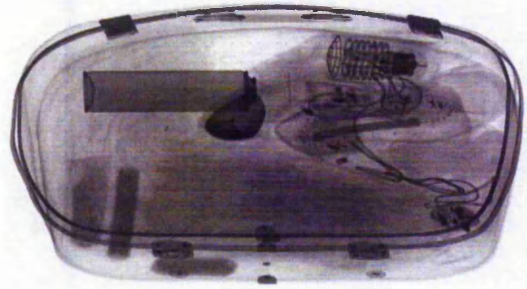

(a) Original

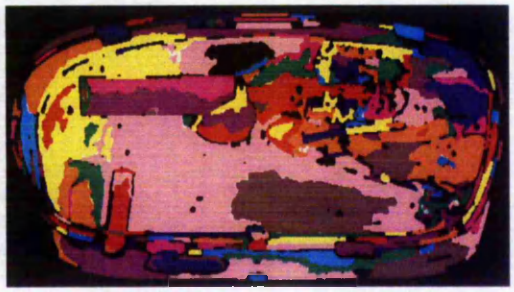

(b) scale 2^2 (c) scale 2^3

Fig. 4.7 (a)- Original monochrome low energy x-ray image of baggage sample-4, (b)- segmented image at scale 2^2 and (c)- segmented image at scale 2^3.

4.3 Categorisation of Overlapping Image Structure

The results from the wavelet image segmentation algorithm are used to categorise the overlapping image structure. This is accomplished by consideration of the average grey level of a particular segment in relationship to its neighbouring segments. This enables the delineation of layered structures to be accomplished by applying the *basis materials subtraction* technique described in Chapter 5. However, the following text describes the initial method employed to categorise overlapping image structure.

Generally, the segmented objects in an x-ray image can be categorised into overlapping and non-overlapping objects. Fig. 4.8(a) illustrates a set of hypothetical objects (A, B, C and D) that are x-rayed. The hypothetical grey scale x-ray image of this arrangement is shown in Fig. 4.8(b). The segmented regions in the resultant image are labelled (from 1 to 6) for further analysis. Fig. 4.8(b) also indicates the grey levels for all the segmented regions.

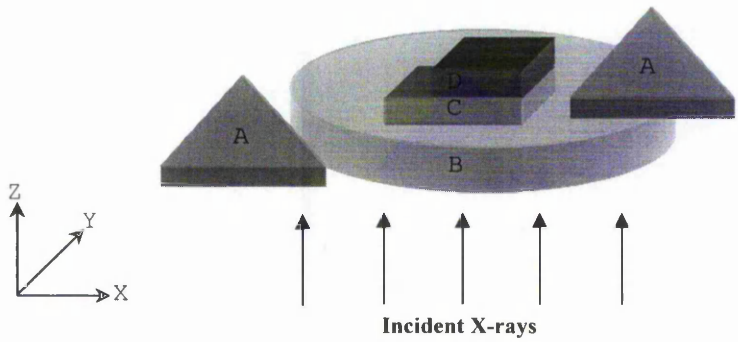

Fig. 4.8(a) Hypothetical inspected objects.

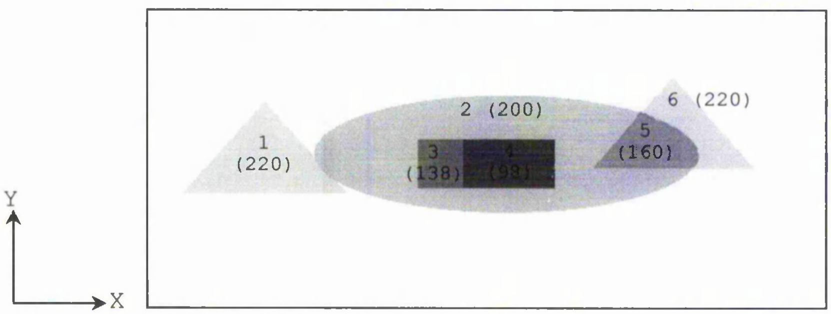

Fig. 4.8(b) Hypothetical grey level x-ray image for the set of objects arranged in Fig. 4.8(a).

The automated image categorisation algorithm initially locates the neighbour regions of each segmented object in the image. Additionally, the algorithm determines the average grey levels for the neighbour regions. For example, region 3 is overlapped by region 2, thus the average grey level for region 3 must be lower than the average grey level for region 2. Therefore, these assumptions are applied to determine the overlapping regions in the segmented image.

Table 4-1 shows an example of the results for the hypothetical grey level image shown in Fig. 4.8(b). It can be appreciated that the segmented regions 1 and 6 are categorised as non-overlapping objects even though they are connected to region 2 and 5 respectively. This is due to the fact that their average grey levels are greater than the average grey levels of their neighbouring regions. While, the results shown for segmented region 3 and 5 are true, since these regions are formed by the object C overlapping object B and, also the overlapping of object B and object A.

However, it is inevitable that the results for the segmented regions 2 and 4 could be overlapping more than one region as shown in Fig 4.8(a). For instance, if the objects are arranged as shown in Fig. 4.9 (i.e. where the whole area of object B is overlapped by object A', and the object D is overlapped by object B), the false results obtained for regions 2 and 4 are now valid. This is because both arrangements shown in Fig 4.8(a) and Fig. 4.9 will exhibit identical spatial x-ray image formation as illustrated in Fig. 4.8(b). Therefore, it would be better if the cases illustrated in Fig. 4.8(a) and Fig. 4.9 are considered by the image categorisation algorithm. As a result, the automated image categorisation algorithm may produce invalid information under certain circumstances.

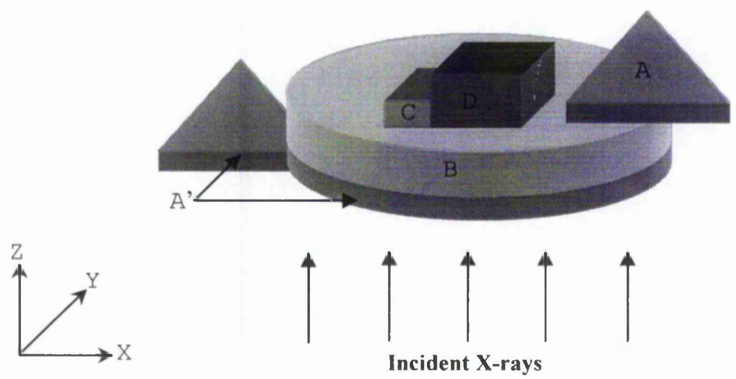

Fig. 4.9 Hypothetical inspected objects.

Segmented Region	Connected Regions	Overlapping Regions
1	2	None (true)
2	1, 3, 4, 5	1 (false)
3	2, 4	2 (true)
4	2, 3	2(false), 3(true)
5	2, 6	2(true), 6(true)
6	5	None (true)

Table 4-1 Automated image categorisation results.

The Fig. 4.10 details the flow chart for the automated image categorisation algorithm. This algorithm is the continuation of the flow chart shown in Fig. 4.1 on page 62. All the successfully segmented regions are labelled (n=m=1,2,3....N, where N=last labelled region) by the program.

Initially, the high energy and the low energy data (i.e. average grey levels in a monochrome digital image format) for each successfully segmented region are obtained from the resultant image. Each of the segmented regions (n) is examined together with all other neighbour regions (m, where $m \neq n$). If region n has an average grey level which is less than a neighbour region m, it is therefore deduced that region n is overlapping region m.

Finally, these results are stored in a database for the quantitative analysis of characteristic angle for each discriminated object in the baggage.

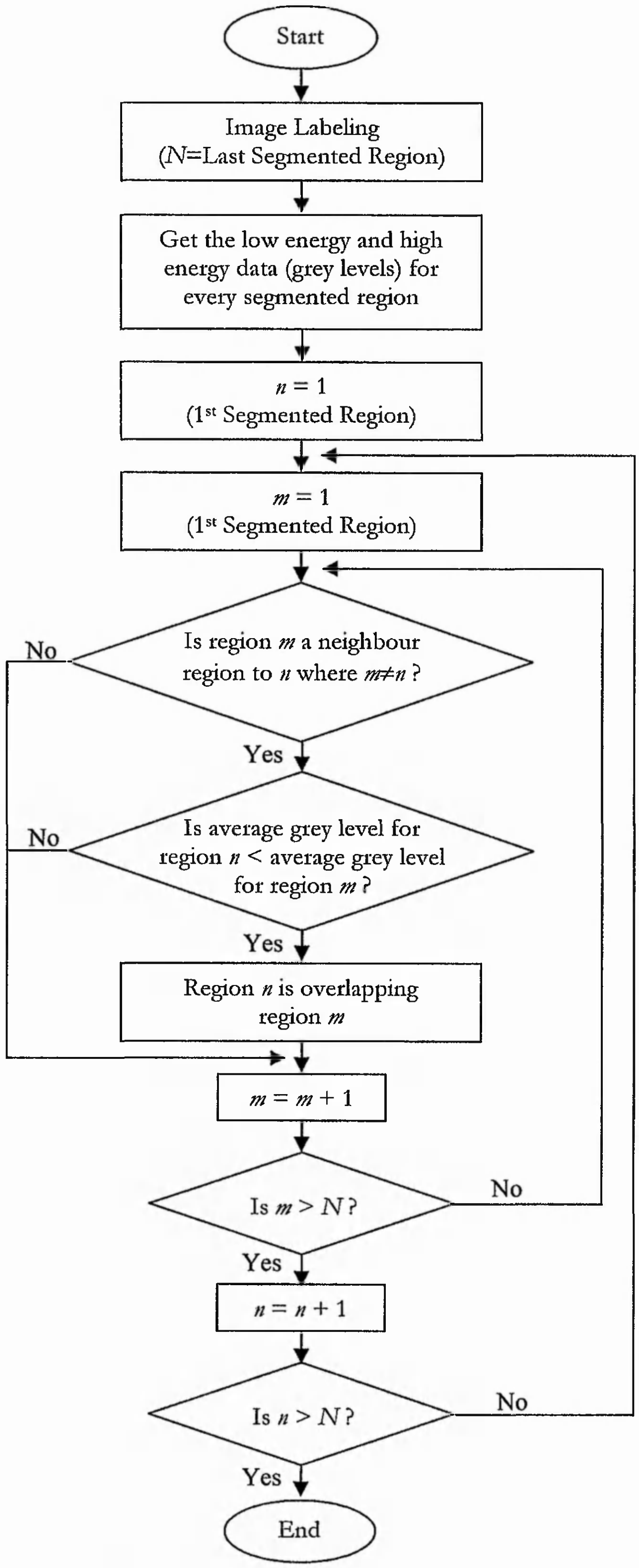

Fig. 4.10 Flow chart for the automated image categorisation algorithm (i.e. categorisation of overlapping image structure).

4.3.1 Limitations

In general, the limitations of the automated image categorisation algorithm can be described by the two scenarios presented below.

Scenario 1:

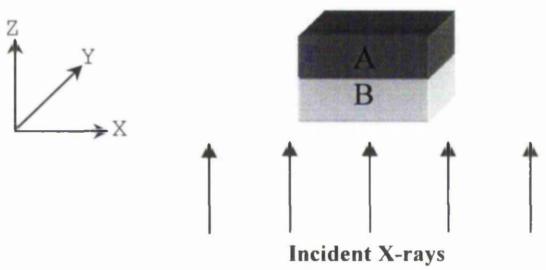

Fig. 4.11 Hypothetical inspected objects.

It is impossible to detect an overlapping object that has the same dimension (except thickness) as the object that it is attached to. This is because both overlapping objects will be displayed as a single object in the resultant x-ray image as illustrated in Fig. 4.11 where object A perfectly overlaps object B. It is therefore suggested for future work that a *multiple-view x-ray system*[H12] could be used to resolve this problem (this is further described in Chapter 7).

Scenario 2:

Object C is placed in a void located in object B. Thus the technique would assume (incorrectly) that object C is overlapped by object A and B.

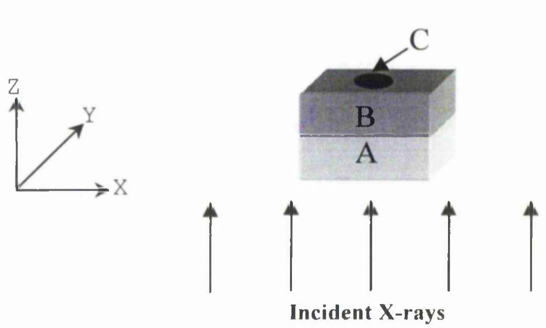

Fig. 4.12 Hypothetical inspected objects.

4.3.2 Experimental Results

A series of experiments has been conducted to evaluate the automated image categorisation algorithm. The image categorisation results were obtained using a wavelet scale set to $s=2^2$. It can be concluded that the algorithm successfully operates within the limits which have been previously described. The results presented in the following subsections indicate the major segmented and labelled features in the resultant images. The detail analysis results are recorded in Appendix D.

Baggage sample-6

Fig. 4.13(a) and (b) illustrate the grey scale high energy and low energy x-ray images for baggage sample-6. Fig. 4.13(c) illustrates each segmented and labelled region in baggage sample-6.

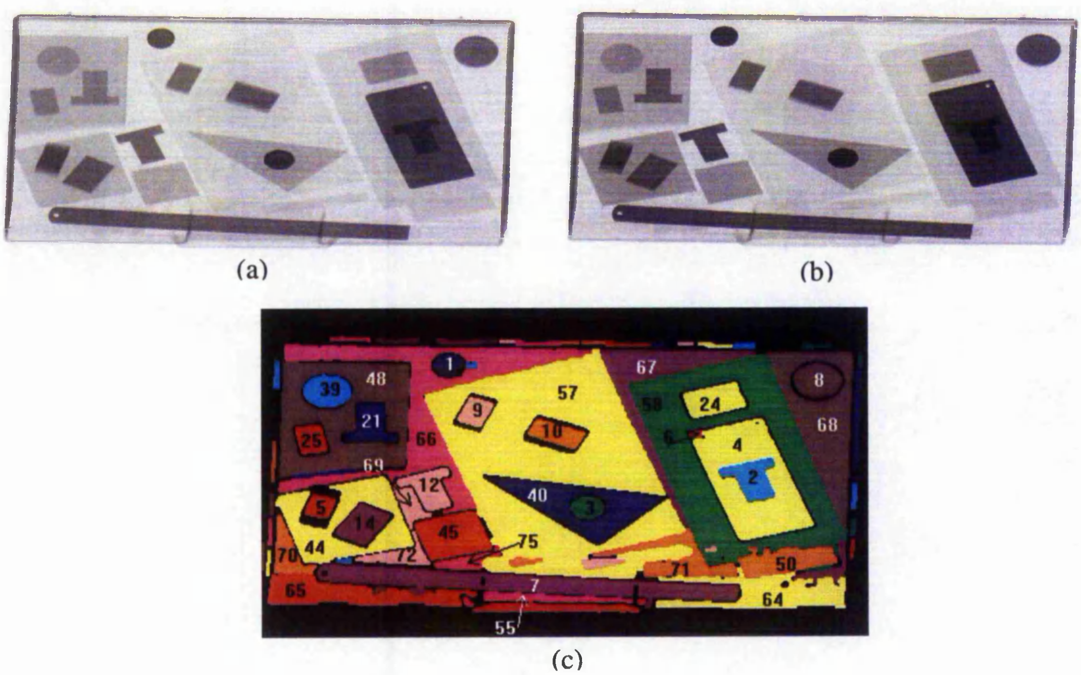

Fig. 4.13 (a)- High energy x-ray image of baggage sample-6, (b)- low energy x-ray image of baggage sample-6 and (c)- segmented and labelled image at scale 2^2.

Table 4-2 presents the automated image categorisation results for baggage sample-6. The average low energy and high energy data for each of the successfully segmented regions are also tabulated. The detail results for the labelled regions are presented in

Appendix D Fig. D-1. The maximum standard deviation of grey levels for a segmented region after the noise filtering process is ±8.

Segmented Region	Average Low and High Energy Grey Level	Standard Deviation	Overlapping Regions
1	39, 74	±3, ±3	66
2	23, 50	±1, ±6	4
3	28, 57	±1, ±5	40
4	51, 87	±3, ±4	6, 58
5	49, 73	±1, ±2	44
6	58, 89	±1, ±1	58
7	64, 104	±3, ±8	55, 57, 64, 65, 75
8	85, 113	±2, ±4	68
9	85, 114	±2, ±2	57
10	77, 103	±2, ±5	57
12	80, 125	±2, ±3	66, 69
14	77, 115	±2, ±3	44
21	104, 140	±2, ±6	48
24	117, 155	±2, ±3	58
25	114, 137	±2, ±3	48
39	145, 156	±1, ±3	48
40	147, 179	±2, ±3	57
44	167, 195	±3, ±4	66, 69, 70, 72
45	161, 184	±3, ±3	57, 66, 69, 72, 75
48	184, 193	±3, ±3	66

Table 4-2 Automated image categorisation results for baggage sample-6.

Baggage sample-7

Fig. 4.14(a) and (b) illustrate the grey scale high energy and low energy x-ray images for baggage sample-7. Fig. 4.14(c) further illustrates each segmented and labelled region in baggage sample-7.

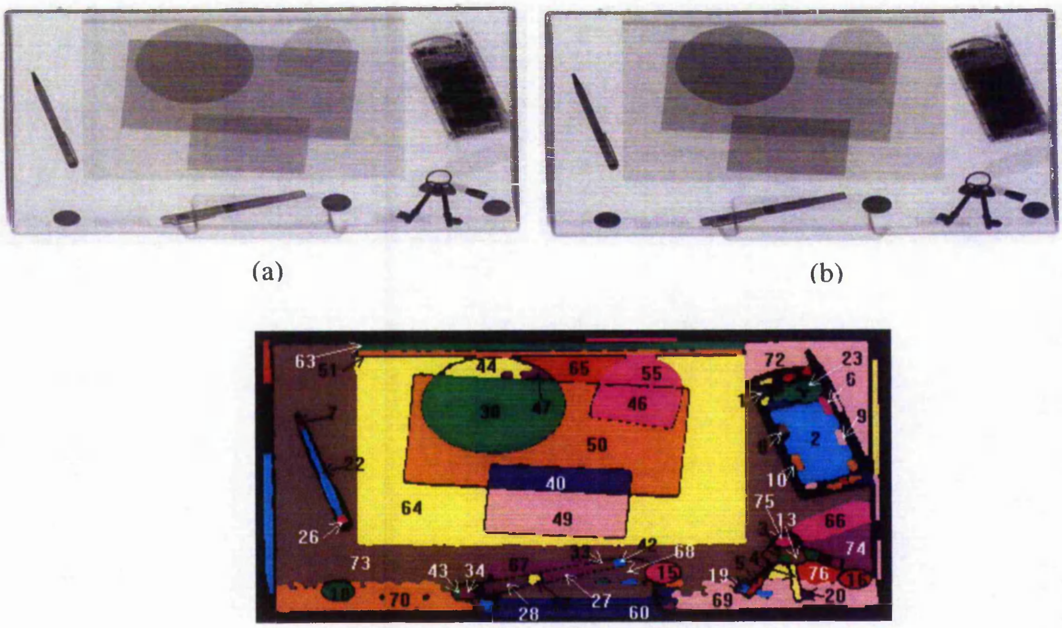

(a) (b)

(c)

Fig. 4.14 (a)- High energy x-ray image of baggage sample-7, (b)- low energy x-ray image of baggage sample-7 and (c)- segmented and labelled image at scale 2^2.

Table 4-3 shows the image categorisation results for baggage sample-7. The average low energy and high energy data for each of the successfully segmented regions are also tabulated. The detail results for all the labelled regions are presented in Appendix D Fig. D-2. The maximum standard deviation of grey levels for a segmented region is ±8.

Segmented Region	Average Low and High Energy Grey Level	Standard Deviation	Overlapping Regions
2	8, 21	±2, ±3	6, 8, 9, 10
7	13, 30	±4, ±7	73
15	30, 60	±2, ±5	68, 73
16	33, 63	±2, ±2	69
18	32, 62	±2, ±1	70
22	49, 89	0, 0	73
38	101, 122	±2, ±2	44, 47, 50
40	107, 133	±1, ±3	49, 50
44	132, 156	±2, ±2	47, 51, 64
46	131, 143	±1, ±1	50, 55
47	135, 157	±1, ±2	65
49	139, 169	±2, ±2	64
50	149, 161	±2, ±2	64, 65
55	176, 185	±3, ±3	64, 65
64	199, 208	±2, ±2	72, 73
70	207, 211	±8, ±7	73

Table 4-3 Automated image categorisation results for baggage sample-7.

Baggage sample-8

Fig. 4.15(a) and (b) illustrate the grey scale high energy and low energy x-ray images for baggage sample-8. Fig. 4.15(c) further illustrates each segmented and labelled region in baggage sample-8.

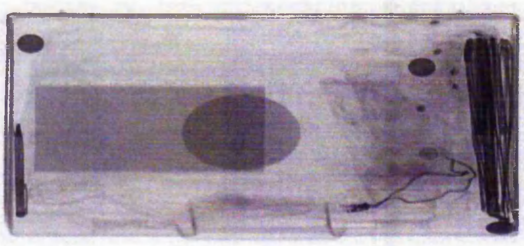

(a)

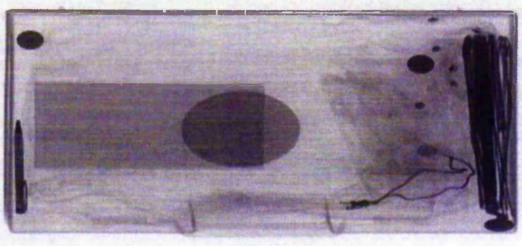

(b)

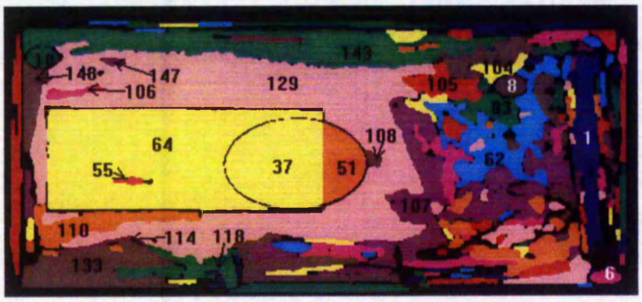

(c)

Fig. 4.15 (a)- High energy x-ray image of baggage sample-8, (b)- low energy x-ray image of baggage sample-8 and (c)- segmented and labelled image at scale 2^2.

Segmented Region	Average Low and High Energy Grey Level	Standard Deviation	Overlapping Regions
8	31, 61	±2, ±3	62, 104
18	42, 75	±2, ±3	129, 143, 148
37	95, 116	±3, ±3	51, 64
51	127, 151	±3, ±3	108, 129
55	135, 148	±1, ±1	64
64	146, 157	±4, ±3	110, 129
105	183, 191	±6, ±5	129
106	188, 195	±2, ±2	129
107	182, 190	±5, ±5	129
108	190, 197	±2, ±2	129
110	186, 193	±5, ±4	129
114	186, 194	±2, ±3	129, 133
118	184, 192	±6, ±6	129, 133
129	201, 207	±4, ±4	143, 147, 148

Table 4-4 Automated image categorisation results for baggage sample-8.

Table 4-4 presents the automated image categorisation results for baggage sample-8. The average low energy and high energy data for each of the successfully segmented regions are also tabulated. The detail results for the labelled regions are presented in Appendix D Fig. D-3. The maximum standard deviation of grey levels for a segmented region is ±6.

Baggage sample-9

Fig. 4.16(a) and (b) illustrate the grey scale high energy and low energy x-ray images for baggage sample-9. Fig. 4.16(c) further illustrates each segmented and labelled region in baggage sample-9.

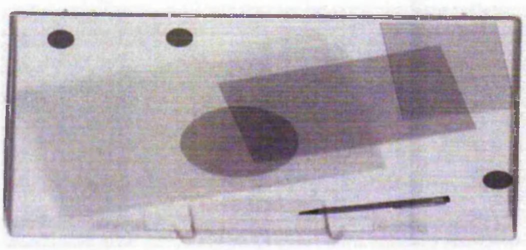

(a)

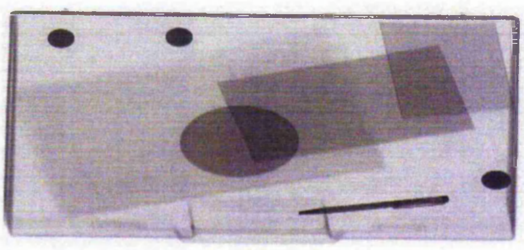

(b)

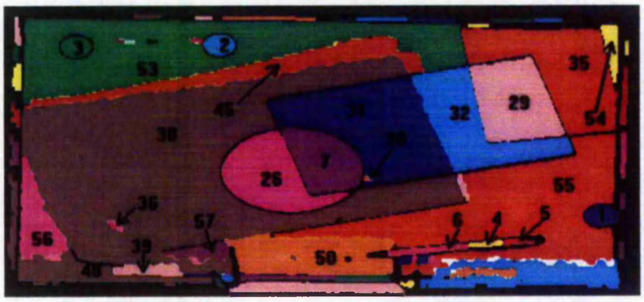

(c)

Fig. 4.16 (a)- High energy x-ray image of baggage sample-9, (b)- low energy x-ray image of baggage sample-9 and (c)- segmented and labelled image at scale 2^2.

Table 4-5 presents the automated image categorisation results for baggage sample-9. The average low energy and high energy data for each of the successfully segmented regions are also tabulated. The detail results for the labelled regions are presented in

Appendix D Fig. D-4. The maximum standard deviation of grey levels for a segmented region in the order of ±10 is obtained.

Segmented Region	Average Low and High Energy Grey Level	Standard Deviation	Overlapping Regions
1	31, 64	±2, ±4	55
2	42, 75	±2, ±2	53
3	42, 76	±2, ±2	53
4	44, 81	±1, ±2	55
5	60, 103	±10, ±10	55
6	58, 95	±5, ±8	55
7	91, 112	±2, ±2	26, 31
26	121, 145	±2, ±2	38
29	134, 146	±2, ±2	32, 35
31	143, 153	±2, ±2	32, 38
32	163, 172	±4, ±3	53, 55
35	180, 188	±2, ±2	53, 54
36	184, 192	±1, ±1	38
38	192, 199	±3, ±3	45, 48, 50, 55, 57
39	190, 196	±3, ±4	48
45	208, 212	±3, ±3	53
48	210, 214	±4, ±4	56, 57
50	209, 212	±5, ±4	55

Table 4-5 Automated image categorisation results for baggage sample-9.

4.4 Summary

The automated x-ray image segmentation and categorisation program has been evaluated with a series of different baggage contents. The results obtained are encouraging for overlapping materials with uniform thickness. The optimum wavelet scale for segmenting a large amount of 'average' baggage contents has been empirically determined as 2^2. The maximum standard deviation of the grey levels for a segmented region computed from the experiments is ±10 indicating a satisfactory image segmentation process.

It can be appreciated from the results that the segmentation for a complex object of non-uniform thickness requires intensive processing and is unsuitable for real time applications. On the other hand, the limitation of the wavelet analysis occurs when the region of interest in an x-ray image is small compared to the background or when both the region of interest and the background have a broad range of grey levels. As a result, the region of interest cannot be segmented successfully.

In realistic conditions, the aforementioned problems can be resolved by isolating the potential threat regions of the x-ray image as a function of grey level. Typically, threat items such as plastic explosives are very dense and will be displayed in low grey levels in the resultant x-ray image.

Additionally, the ability to segment objects with non-uniform structure is problematic in terms of overlapping structure categorisation. Therefore, a more sophisticated approach than that adopted in this research is required. This problem can only be resolved if the three-dimensional information at every image point of the objects are known automatically.

The automated image segmentation program, the extraction of the high energy and the low energy data, and also the information from the automatic image categorisation algorithm will be utilised in the following chapters to extract the characteristic angle for successfully segmented objects.

CHAPTER FIVE

TARGET MATERIAL CALIBRATION AND RECOGNITION

5.1 Introduction

This chapter describes a series of experiments to establish the feasibility of a basis materials subtraction (BMS) technique developed to extract the characteristic angle of overlapping objects. This approach is subsequently combined with the image segmentation and categorisation program described in Chapter 4 to enable automated target material discrimination. Some successful experiments on discriminating a plastic target in several different 'realistic' luggage scenarios are also discussed.

5.2 Development of a Basis Materials Subtraction Technique

Basis materials subtraction (BMS) enables the characteristic angle from overlapping objects to be extracted. The BMS technique is a derivative of the basis materials decomposition (BMD) technique. It is capable of extracting the two energy independent constants (i.e. t_1 and t_2) that characterise the integrated photoelectric and Compton scattering attenuation coefficients (i.e. a_c and a_p) from layers of overlapping substances. Consequently, the characteristic angle θ (i.e. $\tan^{-1}[t_2/t_1]$) for the attenuated material can be obtained. Where t_1 and t_2 are the equivalent basis materials thickness for any attenuated material as determined by using one of the techniques described in Section 2.5.2 (page 26). The research work presented in this chapter utilises the direct approximation method, as it enables a relatively faster computation time in comparison to the non-linear approach. Additionally, the subregion direct approximation method is not employed by the author because it is more sensitive to system noise[C6].

Consider the overlapping materials A, B and C as illustrated in Fig. 5.1, the equivalent basis materials thicknesses (i.e. t_1 and t_2) where the x-rays propagate through distance L_1 of layer A (i.e. t_{1A} and t_{2A}), distance $L_1 + L_2$ of layer A-B (i.e. t_{1AB}

and t_{2AB}) and distance $L_1 + L_2 + L_3$ of layer A-B-C (i.e. t_{1ABC} and t_{2ABC}) can be computed from the direct approximation method described in Section 2.5.2 (page 26). From Equations 2-10 and 2-11 on page 27:

$$t_{1A} = \frac{\rho_A}{\rho_1} a_{1A} L_1 \quad ; \quad t_{2A} = \frac{\rho_A}{\rho_2} a_{2A} L_1 \qquad \text{Equation 5-1(a)}$$

$$t_{1B} = \frac{\rho_B}{\rho_1} a_{1B} L_2 \quad ; \quad t_{2B} = \frac{\rho_B}{\rho_2} a_{2B} L_2 \qquad \text{Equation 5-1(b)}$$

$$t_{1C} = \frac{\rho_C}{\rho_1} a_{1C} L_3 \quad ; \quad t_{2C} = \frac{\rho_C}{\rho_2} a_{2C} L_3 \qquad \text{Equation 5-1(c)}$$

where (t_{1A} , t_{2A}), (t_{1B} , t_{2B}) and (t_{1C} , t_{2C}) are the basis materials thicknesses for target materials A, B and C respectively.

And,

$$t_{1AB} = \frac{\rho_A}{\rho_1} a_{1A} L_1 + \frac{\rho_B}{\rho_1} a_{1B} L_2 \quad ; \quad t_{2AB} = \frac{\rho_A}{\rho_2} a_{2A} L_1 + \frac{\rho_B}{\rho_2} a_{2B} L_2$$

Equation 5-1(d)

$$t_{1ABC} = \frac{\rho_A}{\rho_1} a_{1A} L_1 + \frac{\rho_B}{\rho_1} a_{1B} L_2 + \frac{\rho_C}{\rho_1} a_{1C} L_3 \quad ; \quad t_{2ABC} = \frac{\rho_A}{\rho_2} a_{2A} L_1 + \frac{\rho_B}{\rho_2} a_{2B} L_2 + \frac{\rho_C}{\rho_2} a_{2C} L_3$$

Equation 5-1(e)

Equations 5-1(d) and 5-1(e) can be solved by substituting values of t_{1A}, t_{2A}, t_{1B}, t_{2B}, t_{1C} and t_{2C} from Equations 5-1(a), 5-1(b) and 5-1(c):

$$t_{1B} = t_{1AB} - t_{1A} \quad ; \quad t_{2B} = t_{2AB} - t_{2A} \qquad \text{Equation 5-1(f)}$$

$$t_{1C} = t_{1ABC} - t_{1AB} \quad ; \quad t_{2C} = t_{2ABC} - t_{2AB} \qquad \text{Equation 5-1(g)}$$

As a result, the materials B and C can be discriminated since the (t_{1B} , t_{2B}) and (t_{1C} , t_{2C}) can be theoretically calculated by using the BMS equations shown above (i.e. Equations 5-1(f) and 5-1(g)). It can be deduced from Equations 5-1(f) and 5-1(g), that the thickness of each of the materials A, B and C is not required for the computation of (t_{1B} , t_{2B}) and (t_{1C} , t_{2C}). This is because the values of (t_{1A}, t_{2A}), (t_{1AB}, t_{2AB}) and (t_{1ABC}, t_{2ABC}) can be obtained from the direct approximation method described in Section 2.5.2 (page 26).

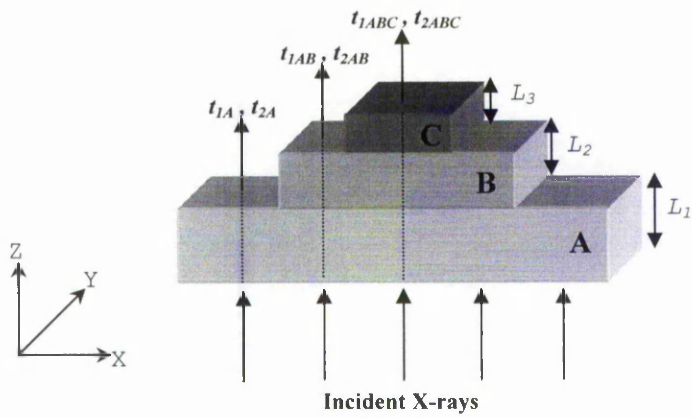

Fig. 5.1 Overlapping materials A, B and C.

The characteristic angle θ (i.e. $\tan^{-1}[t_{2A}/t_{1A}]$ for target material A, $\tan^{-1}[t_{2B}/t_{1B}]$ for target material B, and $\tan^{-1}[t_{2C}/t_{1C}]$ for target material C) is applied for the detection of target materials in this research programme. The basis materials thicknesses for the overlapping layers can be computed by subtracting the equivalent basis materials thickness of the 'nearest' overlapping layer (i.e. t_{1AB}, t_{2AB}) from the equivalent basis materials thicknesses of the target layer (i.e. t_{1ABC}, t_{2ABC}). Consequently, it is not required to determine the number of layers involved for the purpose of target materials detection.

5.3 Calibration of the Direct Approximation Equations

An aluminium stepwedge (AL, $\rho_1 = 2.702$ g/cm^3, Z=13) and a plastic stepwedge (PL, $H_8C_{13}O_7$, ρ_2=1.4 g/cm^3, Z=6.6) were used for the calibration of the direct approximation equations (i.e. Equations 2-14 and Equation 2-15 on page 29).

The experimental x-ray machine was calibrated using the following procedure. The aluminium and plastic stepwedges with various known thickness combinations are imaged as illustrated in Fig. 5.2.

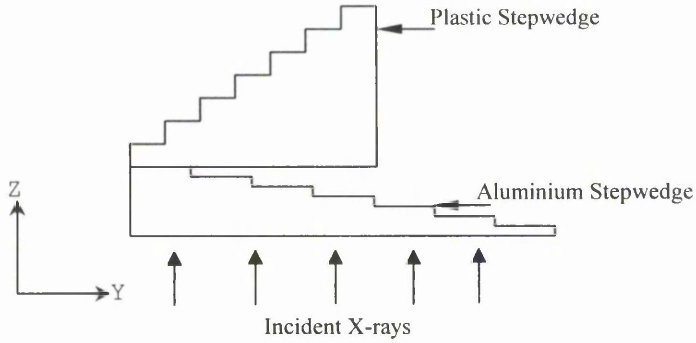

Fig. 5.2 The arrangement of aluminium and plastic stepwedges for the calibration procedure.

The stepwedges were positioned such that the low energy and the high energy transmission signals for each step were produced by the detector modules shown in Fig. 5.3(b) (highlighted in grey). This is to produce a symmetrical image about the *X*-axis (motion axis). Thus, the changes in ray path through the stepwedge in the *Y*-axis is minimised. As a result, the effective thickness t_{eff} of each step t as a function of the x-ray beam convergence angle is:

$$t_{eff} = \frac{t}{\cos\sigma}$$

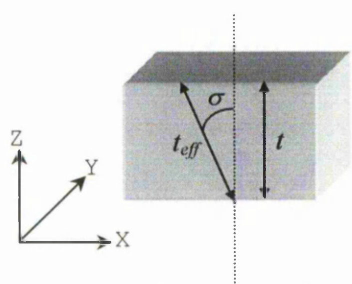

where t is the true thickness for each aluminium or plastic step and the convergence angle $\sigma = 3.75°$ (i.e. inclination of the slit collimated x-ray beam from the normal to the conveyer belt). The collection of calibration data is repeated to enable each step of the plastic stepwedge to be imaged with each step of the aluminium stepwedge. This process requires rescanning each new arrangement of the two stepwedges.

The logarithmic transmission T_H and T_L (i.e. $T_H = \ln(\frac{I_o}{I})_H$, $T_L = \ln(\frac{I_o}{I})_L$) together with all known basis materials thickness combinations (aluminium and plastic steps) were applied to derive the coefficients for the direct approximation equations as shown below (i.e. c_i and d_i, $i = 0, 1, 2 \ldots, 8$):

$$t_1 = c_0 + c_1T_L + c_2T_H + c_3T_LT_H + c_4T_L^{2} + c_5T_H^{2} + c_6T_L^{2}T_H^{2} + c_7T_L^{3} + c_8T_H^{3}$$

$$t_2 = d_0 + d_1T_L + d_2T_H + d_3T_LT_H + d_4T_L^{\ 2} + d_5T_H^{\ 2} + d_6T_L^{\ 2}T_H^{\ 2} + d_7T_L^{\ 3} + d_8T_H^{\ 3}$$

The coefficients c_i and d_i, i = 0, 1, 2 ..., 8, were determined by using *Levenberg-Marquardt*[W6] polynomial least square fitting algorithm.

Consequently, from the equivalent amounts of t_1 and t_2, the characteristic angle for each overlapping object can be determined by applying the BMS technique.

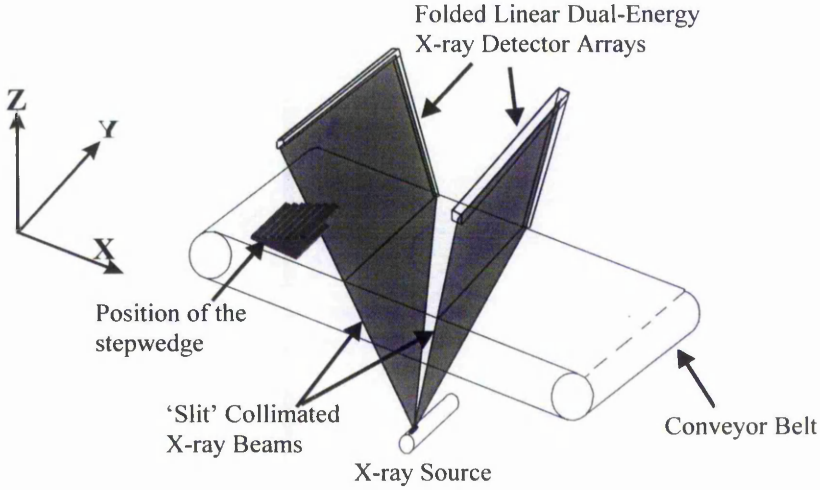

Fig. 5.3(a) The position of the stepwedges for the calibration procedure.

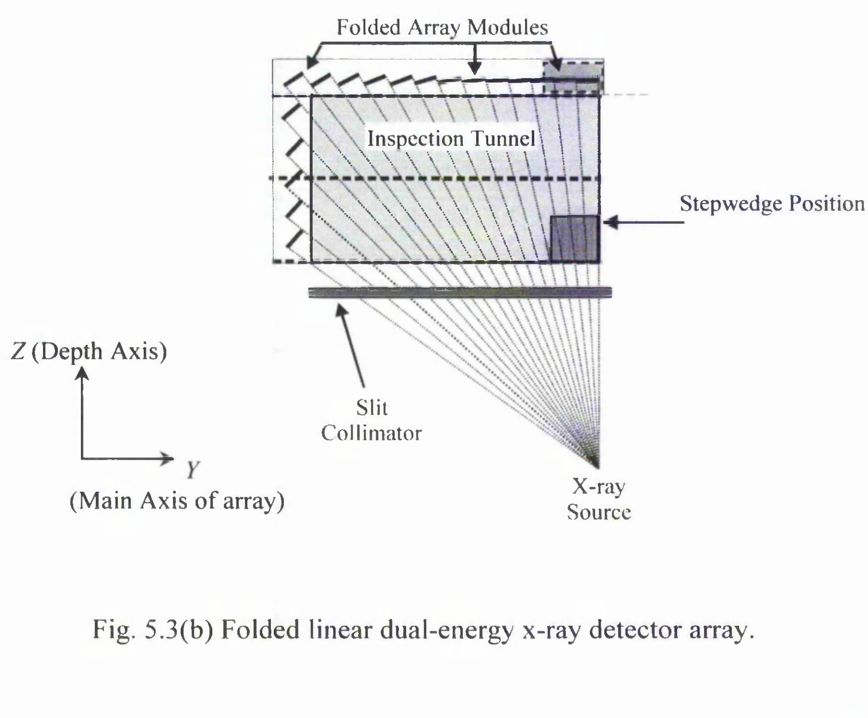

Fig. 5.3(b) Folded linear dual-energy x-ray detector array.

5.3.1 Calibration Results

The calibration procedure utilised an aluminium stepwedge comprised of ten 1mm steps and a plastic stepwedge comprised of fifteen 10 mm steps. The results for the high energy and the low energy calibration data were obtained by scanning the aluminium and plastic stepwedges with all possible thickness combinations. The results are tabulated in Table 5-1 and Table 5-2 in the form of the logarithmic transmission T_H and T_L as a function of AL and PL thickness (mm).

		AL										
	Steps	0	1	2	3	4	5	6	7	8	9	10
PL	0	0	0.059	0.118	0.180	0.235	0.291	0.345	0.399	0.455	0.509	0.565
	1	0.253	0.311	0.375	0.436	0.488	0.545	0.599	0.658	0.748	0.764	0.850
	2	0.512	0.570	0.648	0.684	0.749	0.801	0.844	0.912	0.998	1.044	1.059
	3	0.777	0.819	0.878	0.941	0.992	1.044	1.126	1.169	1.259	1.300	1.363
	4	1.030	1.084	1.135	1.180	1.229	1.293	1.383	1.455	1.501	1.533	1.602
	5	1.277	1.304	1.390	1.431	1.478	1.555	1.593	1.697	1.735	1.776	1.846
	6	1.539	1.567	1.629	1.666	1.728	1.780	1.858	1.943	1.988	2.017	2.086
	7	1.798	1.831	1.906	1.957	1.989	2.029	2.065	2.187	2.238	2.274	2.336
	8	2.042	2.060	2.146	2.193	2.213	2.309	2.341	2.451	2.465	2.541	2.583
	9	2.302	2.328	2.351	2.404	2.469	2.556	2.617	2.682	2.720	2.775	2.850
	10	2.554	2.564	2.632	2.646	2.690	2.793	2.803	2.864	2.943	3.020	3.104
	11	2.804	2.830	2.853	2.900	2.952	3.042	3.069	3.130	3.193	3.250	3.328
	12	3.003	3.026	3.072	3.089	3.193	3.237	3.313	3.374	3.420	3.480	3.667
	13	3.303	3.335	3.342	3.368	3.385	3.516	3.567	3.647	3.711	3.746	3.896
	14	3.535	3.547	3.569	3.582	3.661	3.743	3.812	4.025	4.065	4.089	4.105
	15	3.768	3.776	3.811	3.857	3.874	4.005	4.103	4.125	4.133	4.152	4.225

Table 5-1 Calibration table T_H for the high energy x-ray spectrum. Step sizes of the aluminium and the plastic wedges are 1 mm and 10 mm, respectively.

		AL										
	Steps	0	1	2	3	4	5	6	7	8	9	10
PL	0	0	0.103	0.199	0.290	0.373	0.454	0.538	0.613	0.689	0.757	0.832
	1	0.290	0.392	0.490	0.577	0.666	0.732	0.822	0.897	0.964	1.034	1.100
	2	0.574	0.687	0.769	0.857	0.931	1.001	1.091	1.163	1.241	1.307	1.367
	3	0.853	0.976	1.062	1.141	1.209	1.303	1.357	1.417	1.507	1.581	1.634
	4	1.134	1.263	1.344	1.414	1.481	1.566	1.633	1.707	1.770	1.834	1.908
	5	1.403	1.531	1.602	1.682	1.740	1.833	1.914	1.969	2.033	2.124	2.151
	6	1.699	1.828	1.897	1.975	2.039	2.115	2.158	2.240	2.312	2.367	2.435
	7	1.965	2.089	2.156	2.244	2.316	2.381	2.419	2.516	2.563	2.641	2.726
	8	2.197	2.342	2.403	2.504	2.565	2.617	2.673	2.785	2.817	2.907	2.989
	9	2.469	2.572	2.710	2.781	2.833	2.931	2.965	3.017	3.132	3.193	3.229
	10	2.720	2.858	2.984	3.051	3.121	3.191	3.232	3.317	3.364	3.458	3.520
	11	2.960	3.085	3.207	3.291	3.375	3.445	3.483	3.578	3.630	3.737	3.758
	12	3.217	3.418	3.516	3.559	3.654	3.696	3.762	3.804	3.892	3.947	4.238
	13	3.486	3.700	3.745	3.792	3.891	3.991	4.009	4.149	4.165	4.196	4.426
	14	3.727	3.938	4.007	4.042	4.198	4.226	4.390	4.404	4.424	4.434	4.451
	15	3.973	4.195	4.337	4.386	4.433	4.585	4.663	4.716	4.769	4.828	4.848

Table 5-2 Calibration table T_L for the low energy x-ray spectrum. Step sizes of the aluminium and the plastic wedges are 1 mm and 10 mm, respectively.

The coefficients c_i and d_i, i = 0, 1, 2 ..., 8, are determined from the polynomial least square fitting *Levenberg-Marquardt* algorithm. The results are listed in Table 5-3 and Table 5-4.

Variable	**Value**
c_0	0.212
c_1	37.524
c_2	-47.659
c_3	-64.823
c_4	37.530
c_5	33.072
c_6	0.259
c_7	-2.448
c_8	0.704

Table 5-3 Empirical results for the coefficients c_i, i = 0, 1, 2 ...,8.

Variable	**Value**
d_0	-0.613
d_1	-87.185
d_2	150.051
d_3	94.930
d_4	-61.847
d_5	-47.197
d_6	-0.695
d_7	6.136
d_8	-1.520

Table 5-4 Empirical results for the coefficients d_i, i = 0, 1, 2 ...,8.

The following equations enable the computation of the amount of $[t_1, t_2]$ for a material in the inspected object. These equations are utilised to evaluate the basis materials subtraction technique described in Section 5.2.

$$t_1 = 0.212 + 37.524T_L - 47.659T_H - 64.823T_LT_H + 37.53T_L^2 + 33.072T_H^2 + 0.259T_L^2T_H^2 - 2.448T_L^3 + 0.704T_H^3$$

Equation 5-2(a)

$$t_2 = -0.613 - 87.185T_L + 150.051T_H + 94.93T_LT_H - 61.847T_L^2 - 47.197T_H^2 - 0.695T_L^2T_H^2 + 6.136T_L^3 - 1.52T_H^3$$

Equation 5-2(b)

Fig. 5.4 and Fig. 5.5 illustrate the deviation of calculated plastic and aluminium thicknesses (i.e. obtained from the derived polynomial fit curves for plastic t_2 and aluminium t_1 as basis materials: Equations 5-2(a) and 5-2(b)) from the true thickness of the basis materials. The minimum and maximum residuals for the estimation of basis materials thickness t_1 and t_2 can be summarised as being of the order of {-4.20, +5.26} mm and {-13.93, +10.92} mm respectively.

It can be deduced that the polynomial curves for the estimation of the aluminium and plastic basis materials do not approximate the input experimental data closely.

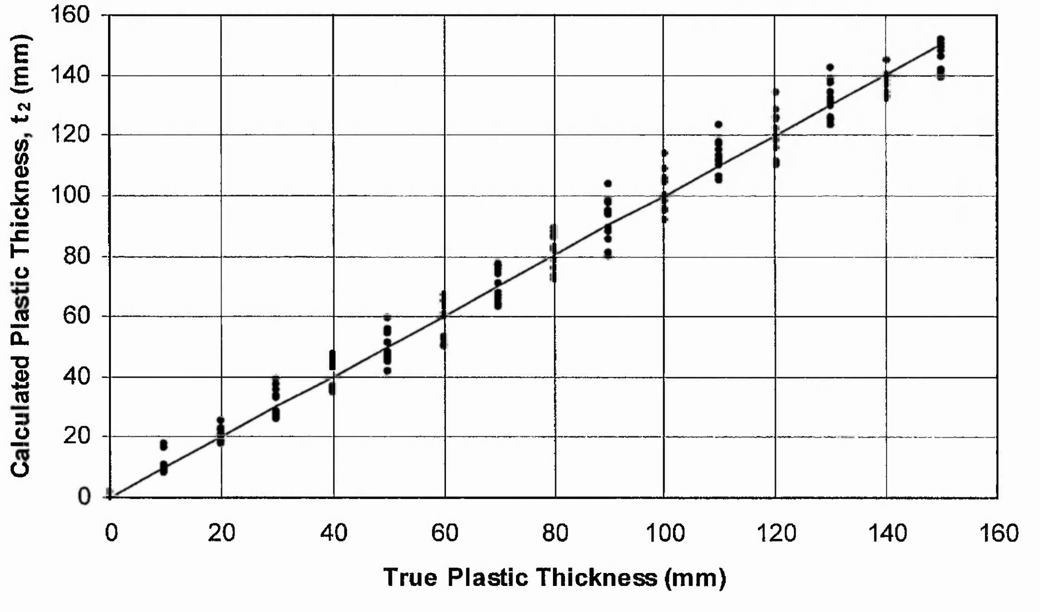

Fig. 5.4 The deviation of the calculated plastic thickness from the true value.

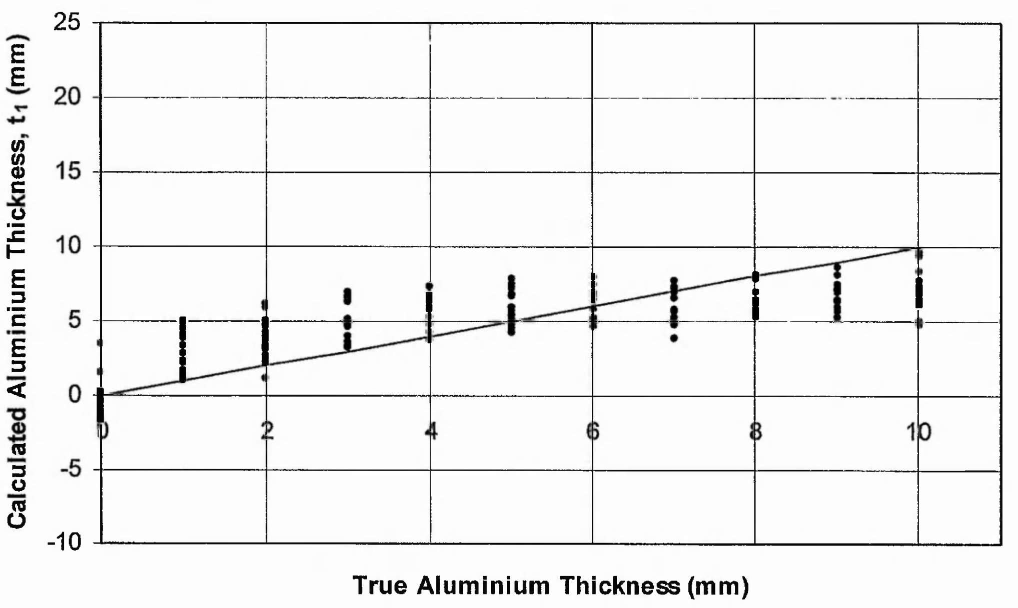

Fig. 5.5 The deviation of the calculated Aluminium thickness from the true value.

5.4 Experiments on the Extraction of the Characteristic Angle from Overlapping Materials

The target was arranged under several layers of masking materials as illustrated in Fig. 5.6. The overlapping effect is accounted for by applying the basis materials subtraction technique. This phase of experimental work was conducted manually to validate the basis materials subtraction technique.

Initially, the equivalent amount of aluminium and plastic basis materials (t_1 and t_2) for the target material shown in Fig. 5.6 is calculated from:

$$t_{1\,target} = t_1 - t_{1'}$$

$$t_{2\,target} = t_2 - t_{2'}$$

where t_1 and t_2 are the basis materials thicknesses for the overlapping layers including the target layer, while $t_{1'}$ and $t_{2'}$ are the equivalent basis materials thickness for the 'nearest' overlapping layer to the target layer. The characteristic angle for the target material is $\theta = tan^{-1}[t_{2target}/t_{1target}]$.

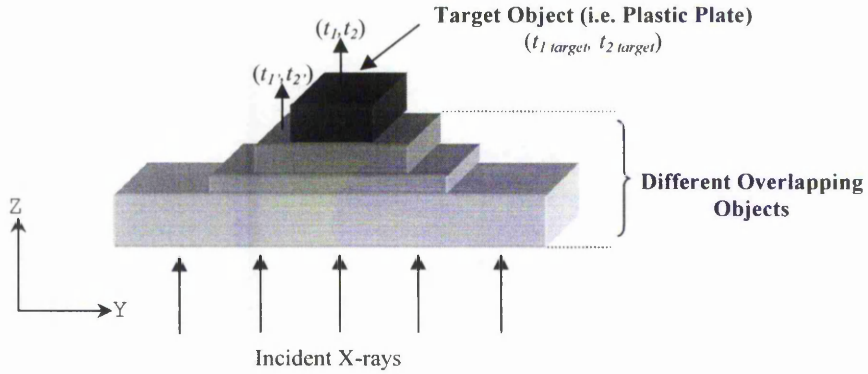

Fig. 5.6 Illustration of the target object (Plastic Plate) arranged on different overlapping materials.

The overlapping materials with their respective thicknesses utilised in the following experiments are listed in Table 5-5.

Object	Material
A	Leather (5.3 mm)
B	Book (5.8 mm)
C	PVC Plate (6.0 mm)
D	Sugar (50.0 mm)
E	Glass (4.6 mm)
F	Carpet with 80% Wool and 20% Nylon (9.0 mm)
G	Wood (39.2 mm)
H	Unpopulated Printed Circuit Board (1.6 mm)
PL	Plastic Plate (10 mm)

Table 5-5 Overlapping materials.

5.4.1 Target: Plastic Plate

A plastic plate (PL) was arranged under one, two, …., five layers of various combinations of overlapping materials as illustrated in Fig. 5.6. The equivalent amounts of aluminium and plastic basis materials (t_1 and t_2) for the target material are calculated by utilising the 3rd-order polynomial fit equations and the basis materials subtraction technique. The characteristic angle for the target material is computed from $tan^{-1}[t_{2PL}/t_{1PL}]$. In this case the target material is the plastic basis material. Therefore, by definition it can be stated that the true value for (t_{1PL} , t_{2PL}) is (0 mm , 10.02 mm) producing a characteristic angle of 90°.

5.4.1.1 One Layer of Overlapping Material

The calculated (t_{1PL} , t_{2PL}) and characteristic angle θ for the plastic target, (PL) for each configuration of layers is listed in Table 5-6.

	Calculated t_{1PL}, t_{2PL} (mm)			Calculated angle θ (degrees)	Error in calculated angle (%)
PL overlapping A	t_{1APL}, t_{2APL}	0.1	14.9	91.0	1.11
	t_{1A}, t_{2A}	0.3	3.4		
	t_{1PL}, t_{2PL}	-0.2	11.5		
PL overlapping B	t_{1BPL}, t_{2BPL}	3.5	23.3	88.7	-1.44
	t_{1B} t_{2B}	3.3	14.4		
	t_{1PL}, t_{2PL}	0.2	8.9		
PL overlapping C	t_{1CPL}, t_{2CPL}	-0.3	15.2	91.7	1.89
	t_{1C}, t_{2C}	0	4.9		
	t_{1PL}, t_{2PL}	-0.3	10.3		
PL overlapping D	t_{1DPL}, t_{2DPL}	2.3	49.6	85.5	-5.00
	t_{1D}, t_{2D}	1.4	38.1		
	t_{1PL}, t_{2PL}	0.9	11.5		
PL overlapping E	t_{1EPL}, t_{2EPL}	9.0	16.8	83.9	-6.78
	t_{1E}, t_{2E}	8.0	7.5		
	t_{1PL}, t_{2PL}	1.0	9.3		

Table 5-6 The calculated (t_{1PL} , t_{2PL}) and resultant characteristic angle for the plastic target (PL) for different overlapping materials.

Fig. 5.7 shows an example of the low energy and the high energy x-ray image for the plastic plate overlapping a book (object B).

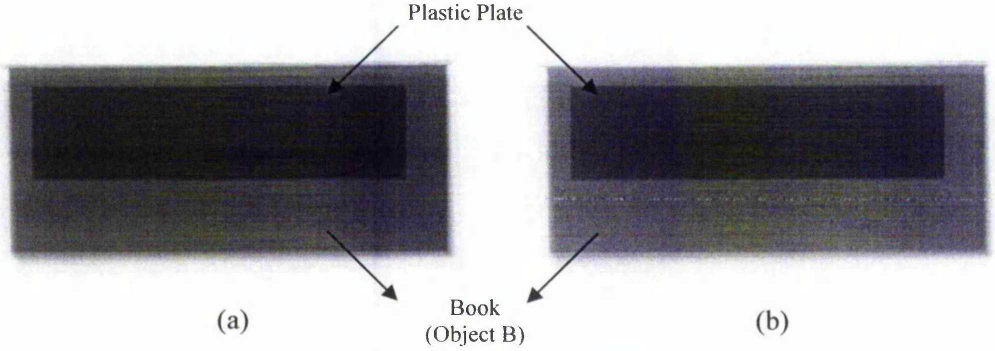

Fig. 5.7 Low (a) and high (b) energy x-ray images for plastic plate overlapping a book (object B).

5.4.1.2 Two Layers of Overlapping Materials

The calculated (t_{1PL} , t_{2PL}) and characteristic angle θ for the plastic target, (PL) for different arrangements of two overlapping materials is listed in Table 5-7.

	Calculated t_{1PL}, t_{2PL} (mm)			Calculated angle θ (degrees)	Error in calculated angle (%)
PL overlapping C,F	t_{1CFPL}, t_{2CFPL}	0.6	18.2	88.9	-1.22
	t_{1CF}, t_{2CF}	0.4	7.7		
	t_{1PL}, t_{2PL}	0.2	10.5		
PL overlapping B,F	t_{1BFPL}, t_{2BFPL}	1.0	15.0	88.9	-1.22
	t_{1BF}, t_{2BF}	0.8	4.5		
	t_{1PL}, t_{2PL}	0.2	10.5		
PL overlapping B,C	t_{1BCPL}, t_{2BCPL}	6.1	29.1	87.8	-2.40
	t_{1BC}, t_{2BC}	5.7	18.5		
	t_{1PL}, t_{2PL}	0.4	10.6		
PL overlapping E,F	t_{1EFPL}, t_{2EFPL}	6.0	13.1	86.5	-3.89
	t_{1EF}, t_{2EF}	5.4	3.4		
	t_{1PL}, t_{2PL}	0.6	9.7		
PL overlapping A,B	t_{1ABPL}, t_{2ABPL}	5.2	30.0	86.1	-4.33
	t_{1AB}, t_{2AB}	4.5	19.6		
	t_{1PL}, t_{2PL}	0.7	10.4		

Table 5-7 The calculated (t_{1PL} , t_{2PL}) and characteristic angle for the plastic target, (PL) for different combinations of two overlapping materials.

5.4.1.3 Three Layers of Overlapping Materials

The calculated (t_{1PL} , t_{2PL}) and characteristic angle θ for the plastic target, (PL) for different arrangements of three overlapping materials is listed in Table 5-8.

	Calculated t_{1PL}, t_{2PL} (mm)			Calculated angle θ (degrees)	Error in calculated angle (%)
PL overlapping C,E,F	t_{1CEFPL}, t_{2CEFPL}	4.20	19.5	90.0	0
	t_{1CEF}, t_{2CEF}	4.20	10.3		
	t_{1PL}, t_{2PL}	0	9.2		
PL overlapping A,B,F	t_{1ABFPL}, t_{2ABFPL}	1.6	18.1	91.1	1.22
	t_{1ABF}, t_{2ABF}	1.8	7.6		
	t_{1PL}, t_{2PL}	-0.2	10.5		
PL overlapping B,C,F	t_{1BCFPL}, t_{2BCFPL}	0.9	19.2	88.8	-1.33
	t_{1BCF}, t_{2BCF}	0.7	9.8		
	t_{1PL}, t_{2PL}	0.2	9.4		
PL overlapping A,E,F	t_{1AEFPL}, t_{2AEFPL}	4.3	18.2	93.0	3.33
	t_{1AEF}, t_{2AEF}	4.9	6.8		
	t_{1PL}, t_{2PL}	-0.6	11.4		
PL overlapping B,E,F	t_{1BEFPL}, t_{2BEFPL}	5.8	18.3	81.2	-9.78
	t_{1BEF}, t_{2BEF}	4.5	9.9		
	t_{1PL}, t_{2PL}	1.3	8.4		

Table 5-8 The calculated (t_{1PL} , t_{2PL}) and characteristic angle for the plastic target, (PL) for different combinations of three overlapping materials.

5.4.1.4 Four Layers of Overlapping Materials

The calculated (t_{1PL} , t_{2PL}) and characteristic angle θ for the plastic target, (PL) for different arrangements of four overlapping materials is listed in Table 5-9.

	Calculated t_{1PL}, t_{2PL} (mm)			Calculated angle θ (degrees)	Error in calculated angle (%)
PL overlapping B,E,F,G	$t_{1BEFGPL}$, $t_{2BEFGPL}$	4.8	29.9	88.7	-1.44
	t_{1BEFG}, t_{2BEFG}	4.6	20.8		
	t_{1PL}, t_{2PL}	0.2	9.1		
PL overlapping B,D,E,F	$t_{1BDEFPL}$, $t_{2BDEFPL}$	6.0	49.6	88.3	-1.89
	t_{1BDEF}, t_{2BDEF}	5.7	39.4		
	t_{1PL}, t_{2PL}	0.3	10.2		
PL overlapping B,C,E,F	$t_{1BCEFPL}$, $t_{2BCEFPL}$	6.4	22.5	87.4	-2.89
	t_{1BCEF}, t_{2BCEF}	5.9	11.4		
	t_{1PL}, t_{2PL}	0.5	11.1		
PL overlapping A,B,C,F	$t_{1ABCFPL}$, $t_{2ABCFPL}$	0.8	25.8	86.1	-4.33
	t_{1ABCF}, t_{2ABCF}	0.2	16.9		
	t_{1PL}, t_{2PL}	0.6	8.9		
PL overlapping A,B,E,F	$t_{1ABEFPL}$, $t_{2ABEFPL}$	9.4	39.2	86.0	-4.44
	t_{1ABEF}, t_{2ABEF}	8.6	27.8		
	t_{1PL}, t_{2PL}	0.8	11.4		

Table 5-9 The calculated (t_{1PL} , t_{2PL}) and characteristic angle for the plastic target, (PL) for different combinations of four overlapping materials.

5.4.1.5 Five Layers of Overlapping Materials

The calculated (t_{1PL} , t_{2PL}) and characteristic angle θ for the plastic target, (PL) for different arrangements of five overlapping materials is listed in Table 5-10.

	Calculated t_{1PL}, t_{2PL} (mm)			Calculated angle θ (degrees)	Error in calculated angle (%)
PL overlapping B,C,E,F,G	$t_{1BCEFGPL}$, $t_{2BCEFGPL}$	4.9	27.7	88.1	-2.11
	t_{1BCEFG}, t_{2BCEFG}	4.6	18.8		
	t_{1PL}, t_{2PL}	0.3	8.9		
PL overlapping B,C,E,F,H	$t_{1BCEFHPL}$, $t_{2BCEFHPL}$	9.5	17.7	87.8	-2.44
	t_{1BCEFH}, t_{2BCEFH}	9.1	7.1		
	t_{1PL}, t_{2PL}	0.4	10.6		
PL overlapping A,B,C,E,F	$t_{1ABCEFPL}$, $t_{2ABCEFPL}$	7.7	24.2	81.3	-9.67
	t_{1ABCEF}, t_{2ABCEF}	6.3	15.0		
	t_{1PL}, t_{2PL}	1.4	9.2		

Table 5-10 The calculated (t_{1PL} , t_{2PL}) and characteristic angle for the plastic target, (PL) for different combinations of five overlapping materials.

5.4.2 Target: Leather

A leather layer (Object A) was arranged under one, two and three layers of overlapping materials. The true value for (t_{1A} , t_{2A}) is (0.1 mm , 3.8 mm) producing a characteristic angle of 88.5°. The true characteristic angle was computed from the image data produced by screening Object A independently without any masking materials. The calculated (t_{1A} , t_{2A}) and characteristic angle θ for Object A for each arrangement of overlapping materials is listed in Table 5-11.

	Calculated t_{1A}, t_{2A} (mm)			Calculated angle θ (degrees)	Error in calculated angle (%)
A overlapping PL	t_{1APL}, t_{2APL}	0.1	14.9	90.0	1.69
	t_{1PL}, t_{2PL}	0.1	10.5		
	t_{1A}, t_{2A}	0	4.4		
A overlapping B,PL	t_{1ABPL}, t_{2ABPL}	5.2	30.0	91.1	2.94
	t_{1BPL}, t_{2BPL}	5.3	24.8		
	t_{1A}, t_{2A}	-0.1	5.2		
A overlapping E,F,PL	t_{1AEFPL}, t_{2AEFPL}	4.7	17.5	86.6	-2.15
	t_{1EFPL}, t_{2EFPL}	4.5	14.1		
	t_{1A}, t_{2A}	0.2	3.4		

Table 5-11 The calculated (t_{1A} , t_{2A}) and characteristic angle for a leather target, (Object A) for various combinations of overlapping materials.

5.4.3 Target: Book

A book (Object B) was arranged under one, two and three layers of overlapping materials. The true value for (t_{1B} , t_{2B}) is (0.5 mm , 2.5 mm), thus producing a characteristic angle of 78.7°. The true characteristic angle was computed from the image data produced by screening the book independently without any masking materials. The calculated (t_{1B} , t_{2B}) and characteristic angle θ for Object B for various arrangements of overlapping materials is listed in Table 5-12.

	Calculated t_{1B}, t_{2B} (mm)			Calculated angle θ (degrees)	Error in calculated angle (%)
B overlapping PL	t_{1BPL}, t_{2BPL}	0.7	12.6	74.1	-5.84
	T_{1PL}, t_{2PL}	0.1	10.5		
	t_{1B}, t_{2B}	0.6	2.1		
B overlapping F,PL	t_{1BFPL}, t_{2BFPL}	1.1	14.9	76.0	-3.43
	T_{1FPL}, t_{2FPL}	0.6	12.9		
	t_{1B}, t_{2B}	0.5	2.0		
B overlapping C,F,PL	t_{1BCFPL}, t_{2BCFPL}	0.9	19.2	73.3	-6.86
	t_{1CFPL}, t_{2CFPL}	0.6	18.2		
	t_{1B}, t_{2B}	0.3	1.0		

Table 5-12 The calculated (t_{1B} , t_{2B}) and characteristic angle for a book target, (Object B) for different combinations of overlapping materials.

5.4.4 Target: PVC Plate

A PVC plate (Object C) was arranged under one, two and three layers of overlapping materials. The true value for (t_{1C} , t_{2C}) is (-0.4 mm , 6.4 mm) producing a characteristic angle of 93.6°. The true characteristic angle was computed from the image data produced by screening the PVC plate independently without any masking materials. The calculated (t_{1C} , t_{2C}) and characteristic angle θ for the target Object C for each arrangement of overlapping materials is listed in Table 5-13.

	Calculated t_{1C}, t_{2C} (mm)			Calculated angle θ (degrees)	Error in calculated angle (%)
C overlapping PL	t_{1CPL}, t_{2CPL}	-0.7	16.4	93.1	-0.53
	t_{1PL}, t_{2PL}	-0.4	10.9		
	t_{1C}, t_{2C}	-0.3	5.5		
C overlapping F,PL	t_{1CFPL}, t_{2CFPL}	0.6	18.2	90.0	-3.85
	t_{1FPL}, t_{2FPL}	0.6	12.9		
	t_{1C}, t_{2C}	0	5.3		
C overlapping E,F,PL	t_{1CEFPL}, t_{2CEFPL}	4.2	19.5	99.2	5.98
	t_{1EFPL}, t_{2EFPL}	5.4	12.1		
	t_{1C}, t_{2C}	-1.2	7.4		

Table 5-13 The calculated (t_{1C} , t_{2C}) and characteristic angle for the PVC target, (Object C) for different combinations of overlapping materials.

5.4.5 Summary

The empirical results have validated the basis materials subtraction technique developed to calculate the characteristic angle for various layers of overlapping materials. The maximum errors recorded for the experiments in the calculated characteristic angle is {+5.98%, -9.78%}.

It can also be deduced from the experimental results that leather, PVC plate and the plastic plate have very similar characteristic angles. Indeed, all these materials have similar chemical compositions. Therefore, to discriminate materials with identical or similar characteristic angle or Z_{eff} requires determination of their mass density which is presented in Chapter 6.

5.5 Experiments on Other Materials

The following experiments were conducted to evaluate the characteristic angle for target materials which lie outside the window defined by aluminium and plastic basis materials (i.e. characteristic angle > 90° or characteristic angle < 0°).

5.5.1 Target: Wax Candle

A set of nominally identical wax candles (each 14.5 mm thick) were arranged on an aluminium stepwedge (10 steps, each step 1 mm thick) as illustrated in the high energy and the low energy x-ray images in Fig. 5.8. The calculated characteristic angle θ for the wax candles on each step is listed in Table 5-14. The standard deviation for the characteristic angle is ±2.73 with respect to the mean value of 94.7.

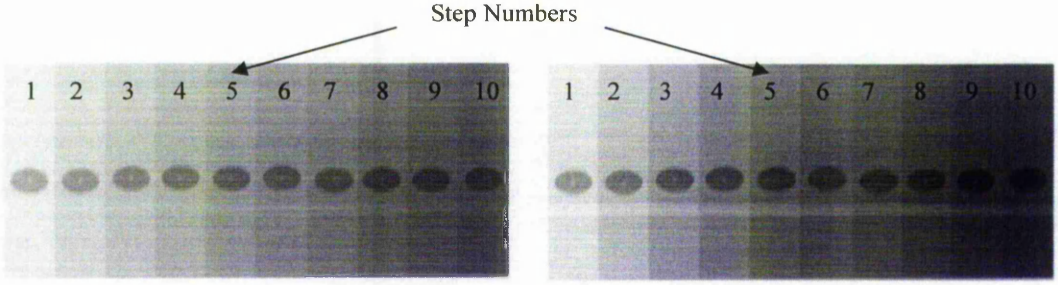

Fig. 5.8 (a) High energy (b) low energy x-ray images.

Step	Calculated Characteristic Angle
1	97.2°
2	95.2°
3	92.6°
4	97.0°
5	92.4°
6	90.7°
7	99.5°
8	93.0°
9	96.1°
10	93.5°

Table 5-14 The calculated characteristic angle for the wax candles placed on an aluminium stepwedge.

5.5.2 Target: Steel Plate

A set of nominally identical *T-shape* steel plates (each 0.5 mm thick) were arranged on an aluminium stepwedge (10 steps, each step 1 mm thick) as illustrated in the high energy and the low energy x-ray images in Fig. 5.9. The calculated characteristic angle θ for the steel plate on each step is listed in Table 5-15. The standard deviation for characteristic angle is ±7.16 with respect to the mean value of -33.6.

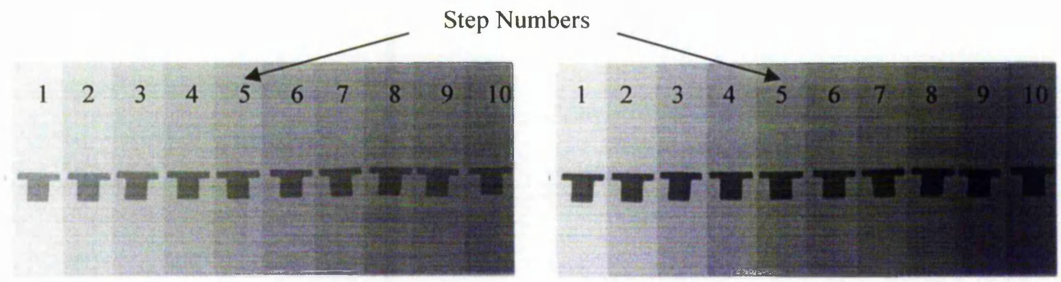

(a) (b)

Fig. 5.9 (a) High energy (b) low energy x-ray images.

Step	Calculated Characteristic Angle
1	-43.5°
2	-41.1°
3	-39.9°
4	-38.6°
5	-35.8°
6	-31.2°
7	-25.4°
8	-30.0°
9	-26.6°
10	-23.5°

Table 5-15 The calculated characteristic angle for the steel targets placed on an aluminium stepwedge.

5.5.3 Summary

The empirical results obtained for the organic wax candle has a characteristic angle marginally greater than 90° are acceptable. The standard deviation for the characteristic angle calculations is ±2.73 which is low. This is because the wax candle has a characteristic angle that is close to the plastic basis material.

On the other hand, the experimental results for the steel plate has a standard deviation of ±7.16 for the characteristic angle. This large error occurs because the steel target has a much higher effective atomic number (i.e. a characteristic angle << 0°) than the aluminium basis material.

The empirical determination of the characteristic angle is limited to experimental objects that have effective atomic number lying within or close to the window defined by the aluminium and plastic basis materials (i.e. $6.6 \leq Z_{eff} \leq 13$ or 0°≤characteristic angle≤90°). The error in characteristic angle calculation will increase as the target's effective atomic number increasingly falls out of this range. Nevertheless, it is envisaged that this problem can be alleviated by careful selection of new basis materials that best mimic the normal materials present in baggage and by applying the *Basis Material Coefficients Transformation Method*[G11, G12]. This technique is further discussed in the summary of this chapter.

5.6 Experiments on Automated Target Material Detection for 'Real Baggage'

The automated x-ray image segmentation and categorisation programs described in Chapter 4 are combined with the basis materials subtraction equations to produce an automated system. The flow chart for the resultant software program is illustrated in Fig. 5.12. This was used to discriminate targets in 'real' baggage scenarios. The complete software for the automated target material detection program is included in Appendix E.

The program displays the discriminated target material in red, provided that the calculated characteristic angle lies within the predefined window (i.e. 87.0<ϑ<92.0, for a plastic target).

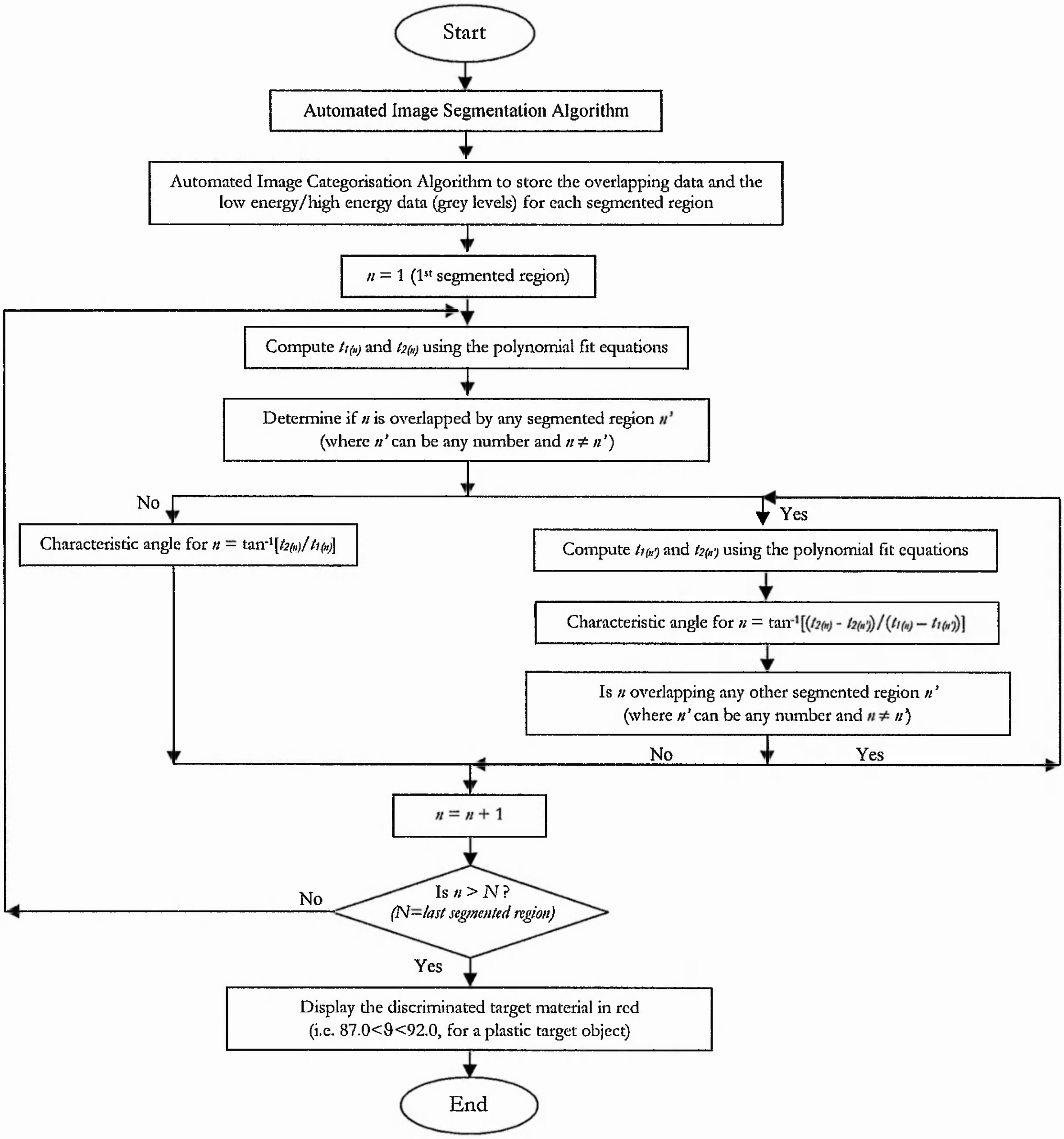

Fig. 5.10 Flow chart for the automated target material detection program.

5.6.1 Baggage Sample-7

Fig. 5.11 illustrates the detection of a plastic plate (PL) in baggage sample-7, which comprises of various overlapping materials including a book, glass sheet, PVC plate, keys, and coins. The area of target material is highlighted in Fig. 5.11(b). The segmented and labelled image resulting from the automated image segmentation and categorisation programs is shown in Fig. 5.11(c). Thus, the segmented regions 38, 40, 46 and 50 in the labelled image constitute the area of the plastic target.

Table 5-16 tabulates the results produced by the automated target material detection program. The characteristic angle calculation for each of the segmented regions in baggage sample-7 is recorded in Appendix F.

Segmented Region	Calculated t_{1PL}, t_{2PL} (mm)	Calculated angle θ (degrees)	Error in calculated angle (%)
38	0.23, 8.93	88.5	-1.63
40	-0.27, 9.99	91.6	1.72
46	0.33, 9.23	88.0	-2.26
50	-0.1, 10.17	90.6	0.62

Table 5-16 The calculated (t_{1PL} , t_{2PL}) and characteristic angle for the plastic target, (PL) in baggage sample-7.

The calculated characteristic angle for the plastic plate is very close to its true value of 90°. It can be appreciated from Fig. 5.11 (d) that several other regions of the baggage have characteristic angles close to that of plastic. Thus, these are false positive detections produced by the inaccuracy of the polynomial curve fitting and also the limitations of the automated image categorisation program as discussed in Chapter 4.

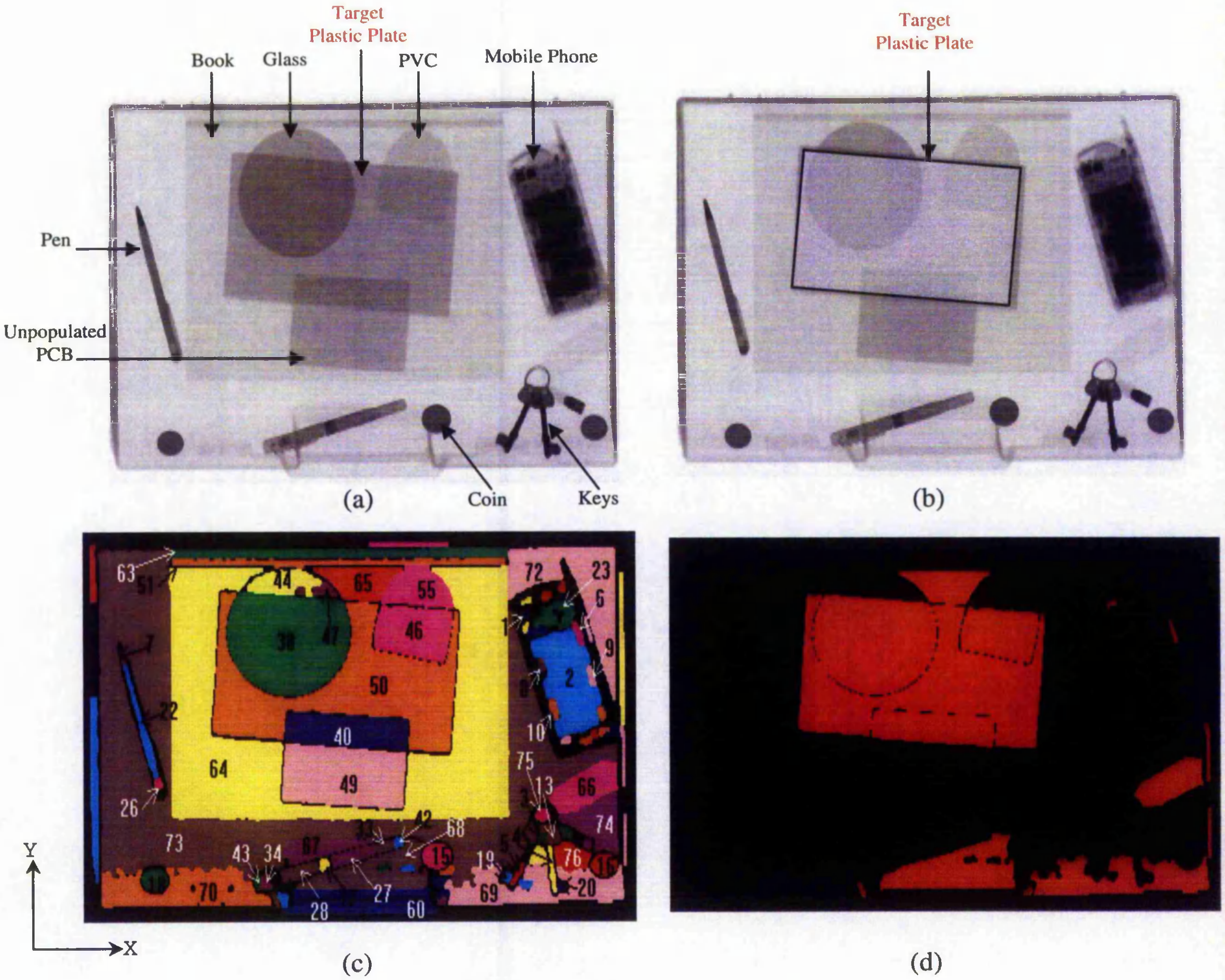

Fig. 5.11 Discriminating a plastic target in baggage sample-7.

5.6.2 Baggage Sample-8

Fig. 5.12 depicts the detection of a plastic plate (PL) in baggage sample-8, which comprises of various overlapping objects including a glass sheet, coins, clothing and an umbrella. The target object is highlighted in Fig. 5.12(b). The segmented and labelled image resulting from the automated image segmentation and categorisation programs is shown in Fig. 5.12(c). Therefore, the segmented regions 37 and 64 in the labelled image compose the area of the plastic target.

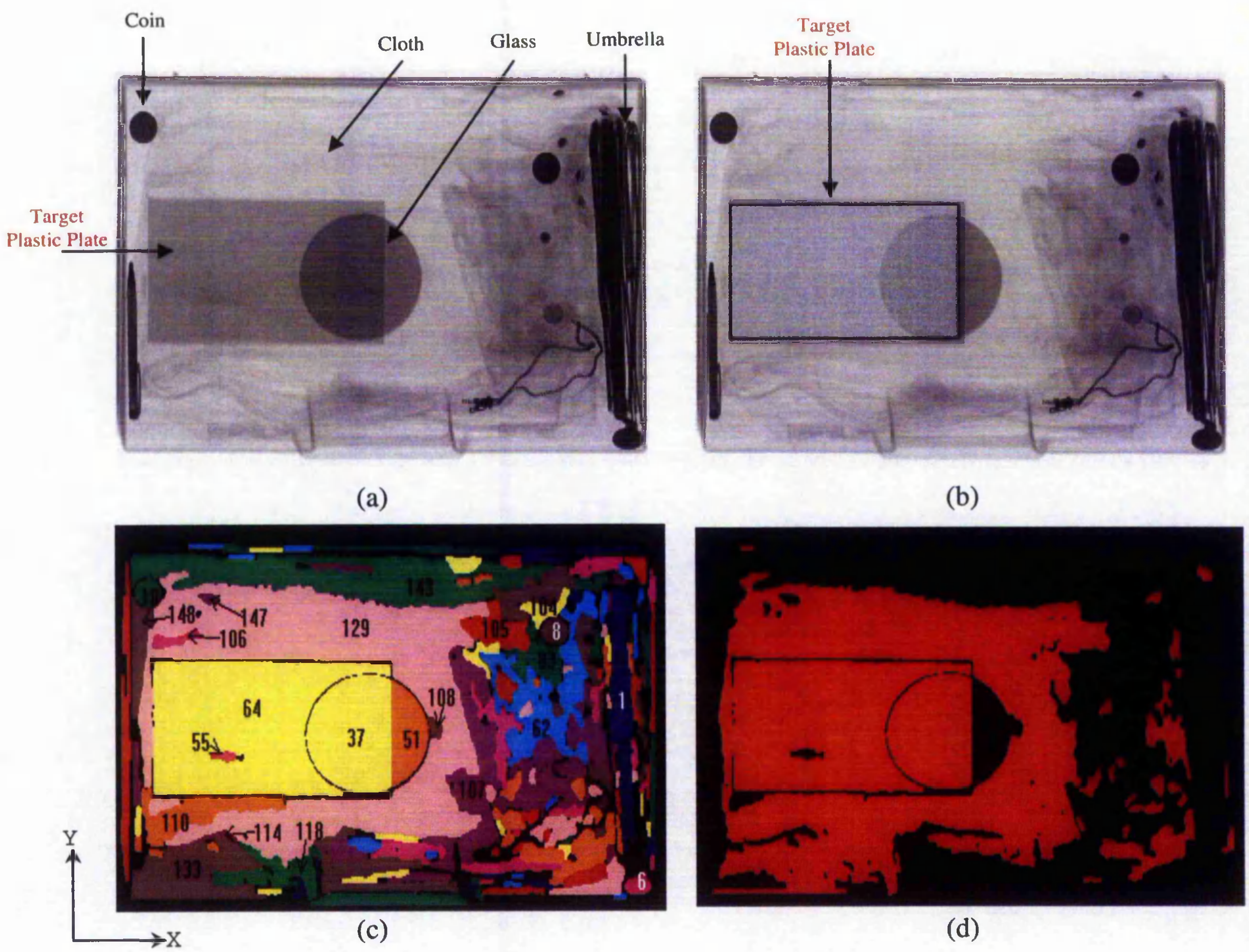

Fig. 5.12 Discriminating a plastic target in baggage sample-8.

Table 5-17 tabulates the results produced by the automated target material detection program. The characteristic angle calculations for all the segmented regions in baggage sample-8 are recorded in Appendix F.

Segmented Region	Calculated t_{1PL}, t_{2PL} (mm)	Calculated angle θ (degrees)	Error in calculated angle (%)
37	0.20, 9.95	88.8	-1.29
64	-0.01, 10.77	90.0	0.04

Table 5-17 The calculated (t_{1PL}, t_{2PL}) and characteristic angle for the plastic target, (PL) in baggage sample-8.

It can be again concluded that the calculated characteristic angle for the plastic plate is very close to its true value of 90°. Fig. 5.12 (d) shows the results obtained from the automated target material detection program. It can be deduced that several other regions of the baggage have characteristic angles that are similar to the plastic plate. Thus, these are also false positive detections produced by the inaccuracy of the polynomial curve fitting and also the limitations of the automated image categorisation program as discussed in Chapter 4.

5.6.3 Baggage Sample-9

Fig. 5.13 illustrates the detection of a plastic plate (PL) in baggage sample-9, which comprises of various overlapping materials including a newspaper, coins, glass and wood plate. The area of target material is highlighted in Fig. 5.13(b). The segmented and labelled image resulting from the automated image segmentation and categorisation programs is shown in Fig. 5.13(c). Hence, the segmented regions of 7, 29, 31 and 32 in the labelled image constitute the area of the plastic target.

Table 5-18 tabulates the results produced by the automated target material detection program. The characteristic angle calculation for each of the segmented regions in baggage sample-9 is recorded in Appendix F.

Segmented Region	Calculated t_{1PL}, t_{2PL} (mm)	Calculated angle θ (degrees)	Error in calculated angle (%)
7	0.05, 10.02	89.7	-0.29
29	0.12, 9.73	89.3	-0.79
31	0.04, 10.06	89.8	-0.26
32	-0.27, 11.11	91.4	1.55

Table 5-18 The calculated (t_{1PL} , t_{2PL}) and characteristic angle for the plastic target, (PL) in baggage sample-9.

The calculated characteristic angle for the plastic plate is very close to its true value of 90°. It can be appreciated from Fig. 5.13 (d) that several other regions of the baggage have characteristic angles close to plastic plate. These are generally false positive detections produced by the inaccuracy of the polynomial curve fitting and also the limitations of the automated image categorisation program as discussed in Chapter 4.

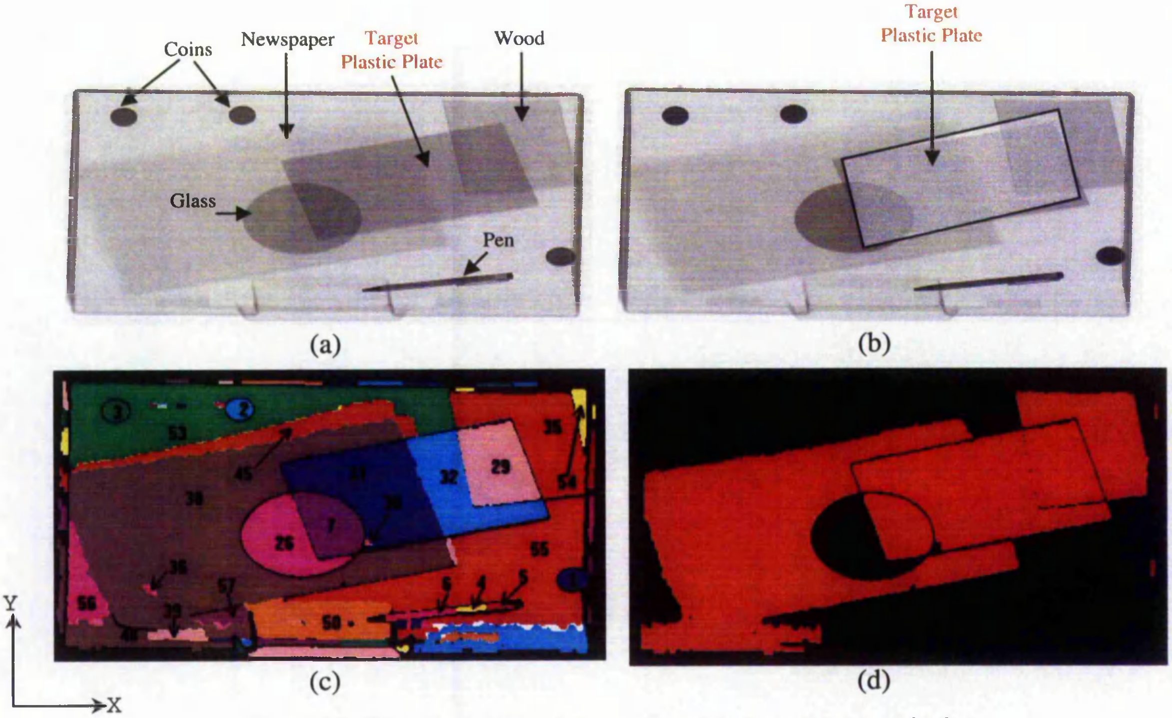

Fig. 5.13 Discriminating a plastic target in baggage sample-9.

5.6.4 Summary

The experimental results produced by the automated target material detection program within the context of experimental noise have validated the automated x-ray image segmentation and categorisation programs, and also the basis materials subtraction technique. It can be deduced from the results that all the calculated (t_{1PL}, t_{2PL}) and the characteristic angle for the plastic target object are very close to its true value. Indeed, the maximum errors are merely {+1.72%, -2.26%}.

5.7 Overview

The results presented in this chapter indicate that the basis materials subtraction technique is feasible. Hence, an 'organic' target substance that is embedded in baggage can be discriminated by applying the BMS technique to subtract the overlapping effect of other objects. However, the accuracy in the calculation of characteristic angle to discriminate the target material is significantly affected by system noise. This can be deduced from the empirical results obtained in Section 5.4. Thus, the maximum errors in the calculated characteristic angle of {+5.98%, -9.78%} are significant for the objective of target material discrimination.

A general problem associated with dual-energy x-ray imaging technique is the amplification of photon noise throughout the image acquisition chain. Thus, the total system noise as discussed in Chapter 3 will further amplify the error in searching for target materials. The low and the high attenuation measurements are independently affected by the photon noise arising from the x-ray source. Hence, a small variation in estimating the energy independent line integrals of the basis material coefficients (i.e. t_1, t_2) will subsequently lead to a great error in the calculated characteristic angle.

In addition, the direct approximation method is sensitive to system noise[C6]. Thus, a small variation in the calibration data creates great errors in calculating the equivalent amounts of basis materials (i.e. t_1, t_2) for a target material. While, the goodness of the polynomial fit equations exhibited minimum and maximum residuals for the estimation of t_1 in the order of {-4.20, +5.26} mm and t_2 for the order of {-13.93, +10.92} mm respectively. The inaccuracy from the polynomial fit will also amplify the error in the computation of characteristic angle. As a result, only test objects with a uniform thickness are utilised in this phase of research work.

It can be generally concluded from the experimental results that the accuracy in calculating the characteristic angle for a target material that is masked by many layers of materials is lower, in comparison to the situation when the target material is masked with a smaller number of overlapping objects. This is due to the fact that the inherent statistical nature of x-rays produces noise arising when there is limited number of transmitted photons[C6] (i.e. low Signal-to-Noise Ratio). Therefore, the accuracy in detecting a target material under dense overlapping conditions will be significantly affected. As a result, more transmitted photons are required to achieve better levels of precision.

The characteristic angle for the overlapping materials is constrained to test items with effective atomic numbers lying within the window of $6.6 \leq Z_{eff} \leq 13$ (i.e. $0° \leq$ characteristic angle $\leq 90°$). Therefore, the technique described will only work correctly if the materials masking the target material fall within the organic window defined by the chosen basis materials. Thus, for instance a metal mask could produce an erroneous false negative.

Nevertheless, this problem can be resolved by careful selection of new basis materials that best mimic the normal materials present in baggage by applying *Basis Material Coefficients Transformation Method*[G11, G12]. The advantage of this technique is the calibration of the conventional aluminium and plastic basis materials can be numerically transformed to cover a wider range of materials in terms of effective atomic number Z_{eff}. The success of this method would rely on the determination of the effective energies from the polychromatic x-ray spectra utilised in the experimental x-ray machine. The *Basis Material Coefficients Transformation Method* is recommended as future work.

Since there are many materials that have similar characteristic angles, it would be highly desirable to determine target material's mass density to discriminate it more accurately. An investigation of mass density determination is described in the following Chapter 6.

CHAPTER SIX

INVESTIGATION OF DEPTH MEASUREMENT FOR MASS DENSITY EXTRACTION

6.1 Introduction

This chapter describes an investigation into the extraction of depth information or thickness data from the binocular stereoscopic x-ray images in order to obtain mass density information. Consequently, this extra information coupled with the characteristic angle will enable a more accurate material discrimination process to be realised.

The schematic diagram of the experimental x-ray machine is shown in Fig. 2.1 on page 11. The x-ray beams utilise a convergence angle of 3.75°. The X and Y-axis shown in Fig. 2.1 are at the conveyer belt surface, while the Z-axis is orthogonal to the plane of linear translation.

This chapter is divided into the following two areas:

- The extraction of depth information from the stereoscopic dual-energy x-ray images.
- The application of the extracted depth information in calculating mass density.

To calculate the depth of an imaged structure requires that conjugate image points relating to the structure be identified. The depth resolution or the minimum detectable increment in object space (δZ) is examined theoretically and empirically for the experimental x-ray system.

The extracted depth data can provide the thickness of layered materials and thus mass density information. Since every material has a unique characteristic angle and mass density, this information can be exploited in searching for plastic explosives.

6.2 The Mathematical Algorithms for Depth Extraction

The basic x-ray beam geometry for the experimental single x-ray source divergent beam stereoscopic configuration is shown in Fig. 6.1 below.

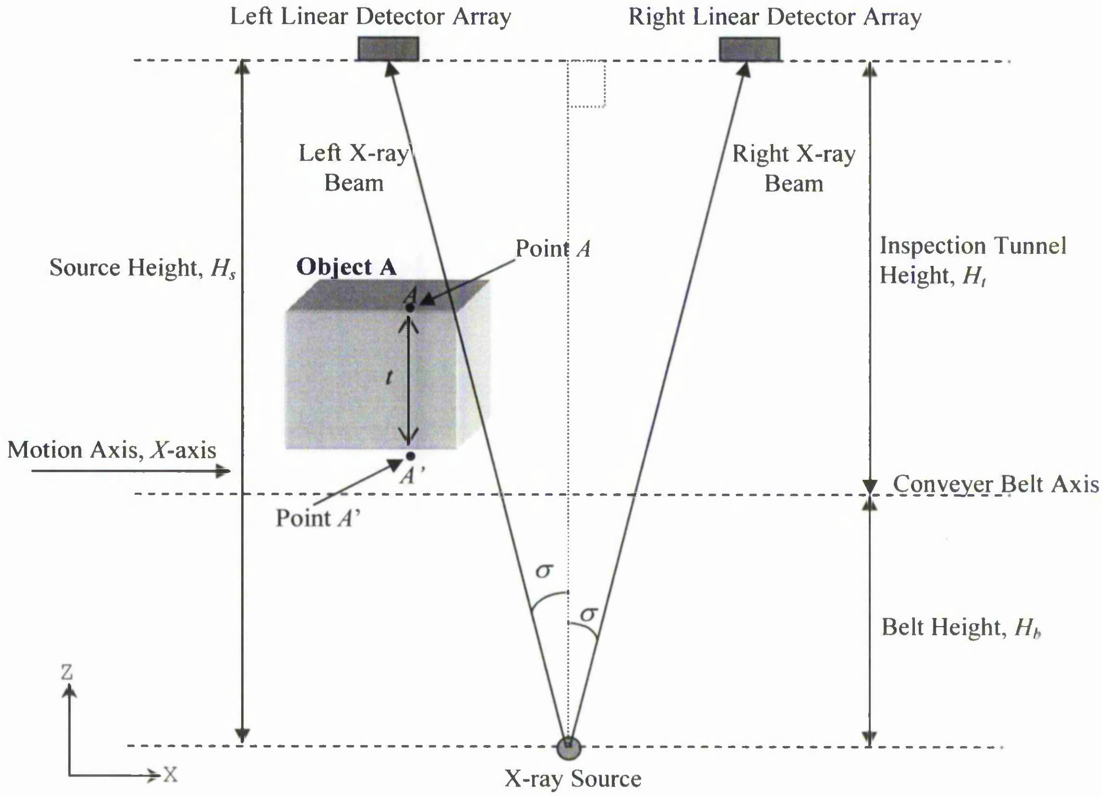

Fig. 6.1 Stereoscopic divergent x-ray beam geometry.

It can be deduced with the aid of Fig. 6.1 that the thickness (*Z*-axis) of an imaged item is proportional to the difference in parallax recorded at the top and bottom of the object:

$$t = \frac{D_A - D_A'}{2 \tan \sigma} \qquad \text{Equation 6-1}$$

where,

$$D_A = (X_{AR} - X_{AL}) \times \delta P$$

$$D_A' = (X_{A'R} - X_{A'L}) \times \delta P$$

The quantities $(X_{AR} - X_{AL})$ and $(X_{A'R} - X_{A'L})$ are the parallax values for point *A* and *A*' respectively obtained from the stereoscopic image pair. The parallax value is expressed as a pixel separation in the left and right images and as such is a dimensionless quantity. However, it can be converted to a distance by multiplying by the conversion parameter δP, which is the corresponding sample size in the X-axis. Also, δP may be interpreted as the minimum parallax in the image sensor plane and is defined as[E6]:

$$\delta P = \frac{B_s}{f_s}$$

where B_s and f_s are the linear translation speed (m/s) and the detector scan frequency (Hz) respectively.

The minimum resolvable depth increment in object space δZ is[E6]:

$$\delta Z = \frac{\delta P}{2\tan\sigma} \qquad \text{Equation 6-2}$$

It can be deduced from Equation 6-2 that the depth resolution is constant throughout the stereoscopic volume and independent of range Z.

The experimental x-ray system has the following parameters:

- Translation belt speed, $B_s = 0.2$m/s;
- Linear detector scan frequency, $f_s = 200$ Hz;
- Convergence angle, $\sigma = 3.75°$.

Therefore, from Equation 6-2 the minimum resolvable depth increment is:

$$\delta Z = 7.6\text{mm}$$

To locate the conjugate points in each perspective automatically is not within the scope of this thesis. Therefore, a manual solution to the correspondence problem is adopted in this research. Points from which measurements are taken are identified by attaching 2mm diameter lead spheres to the object of interest. Each target point can be identified and thus recorded at its corresponding X,Y pixel location in the resultant image.

6.3 Experimental Set Up for Depth Extraction

A series of experiments was devised to determine the depth resolution of the experimental machine. A stepwedge supporting a distribution of *targets* in the form of 2 mm diameter lead spheres is shown in Fig. 6.2. The targets were attached to each step (10 mm) of the plastic stepwedge. In total thirty lead spheres were arranged to mark the top and the bottom of the successive steps. The x-ray image of the stepwedge in Fig. 6.2 is shown in Fig. 6.3.

The accuracy in positioning each target is estimated to be approximately ±1mm. However, the theoretical accuracy in depth resolution is ±7.6 mm. Therefore, any positional errors are considered negligible as far as these experiments are concerned. It should be noted that the Z-axis measurement capability of the experimental system is nominally independent of the x,y,z position of the structure[E6].

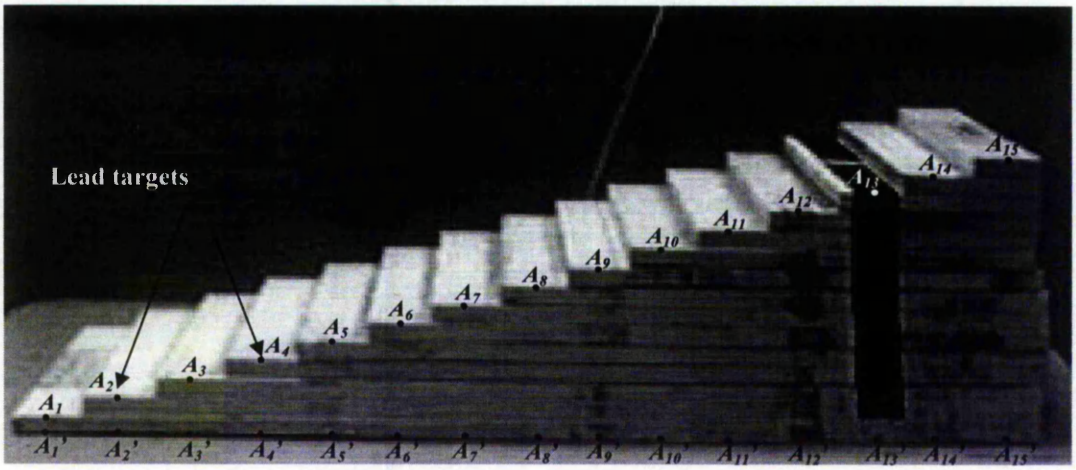

Fig. 6.2 The plastic stepwedge with lead targets on each step.

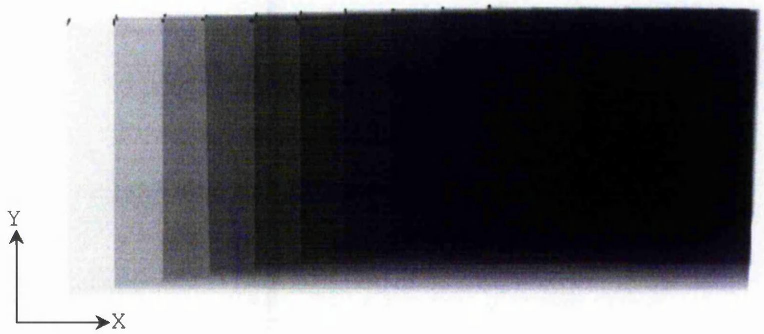

Fig. 6.3 A monochrome x-ray image of the set up in Fig. 6.2.

<u>6.3.1 Parallax Measurements</u>

The X-axis parallax (D_{An}-D_{An}', where n=1, 2, 3…., 15 as illustrated in Fig. 6.2) for each pair of target points is determined from the left and right perspective images. The height of each step is calculated from Equation 6-1.

The left and right perspective images are digitised and stored in the framestore memory in a 1024×320 pixel resolution format. The coordinate system implemented to identify the location of each pixel is illustrated in the diagrams shown in Fig. 6.4. The parallax value D_A for a conjugate point A in the left and right perspective images (A_L and A_R) is:

$$D_A = | X_{AR} - X_{AL} | \times \delta P$$

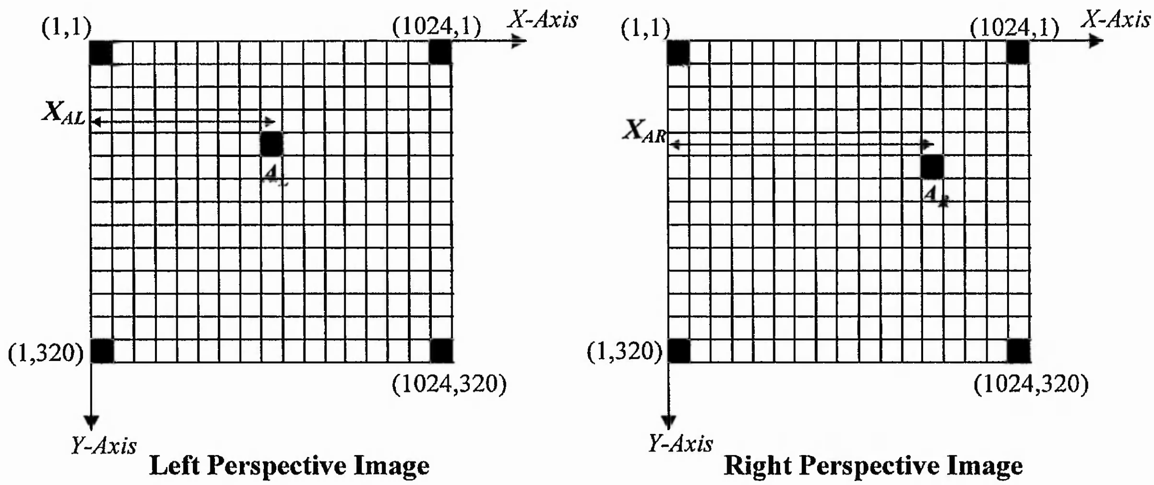

Fig. 6.4 The 'framestore' coordinate system.

6.3.2 Experimental Results

The results in calculating the heights of each plastic step shown in Fig. 6.2 are listed in Table 6-1. Initially, step number 8 was used as a reference to determine the practical value of $\left[\frac{\delta P}{\tan\sigma}\right]$:

From Equation 6-1:

$$80 = \frac{(66-54)}{2\tan\sigma} \times \delta P$$

$$\frac{\delta P}{\tan\sigma} = 13.3\ mm$$

Therefore, the practical minimum resolvable depth resolution δZ that can be detected in object space by examining the conjugate points in the left and right perspective images can be calculated using Equation 6-2:

$$\delta Z = \frac{\delta P}{2\tan\sigma}$$

$$\approx 6.7 \text{ mm}$$

This is in reasonable agreement with the theoretical value of 7.6 mm calculated in Section 6.2 on page 111.

The determination of an object's thickness t is:

$$t = \frac{|X_2 - X_1|_{An} - |X_2 - X_1|_{An'}}{2} \times 13.3\ mm$$

where the quantity $|X_2 - X_1|_{An}$ is the magnitude of the parallax value for conjugate points A_n, while the $|X_2 - X_1|_{An'}$ is the magnitude of the parallax value for conjugate points A_n' respectively, where n=1, 2, 3, …., 15.

Conjugate Points, A_n & A_n'	Left Image X_1	Right Image X_2	Parallax $\|X_2-X_1\|$	Difference in Parallax $\|X_2-X_1\|_{An}-\|X_2-X_1\|_{An'}$	Calculated Height, t (mm)
A_1	137	193	56		
A_1'	138	192	54	2	13.3
A_2	178	236	58		
A_2'	179	234	55	3	20.0
A_3	222	280	58		
A_3'	224	278	54	4	26.7
A_4	258	318	60		
A_4'	261	315	54	6	40.0
A_5	302	363	61		
A_5'	305	359	54	7	46.7
A_6	341	404	63		
A_6'	346	400	54	9	60.0
A_7	380	444	64		
A_7'	384	438	54	10	66.7
A_8	421	487	66		
A_8'	426	480	54	12	80.0
A_9	465	533	68		
A_9'	472	526	54	14	93.3
A_{10}	506	575	69		
A_{10}'	513	568	55	14	93.3
A_{11}	546	617	71		
A_{11}'	552	606	54	17	113.3
A_{12}	588	659	71		
A_{12}'	595	649	54	17	113.3
A_{13}	628	701	73		
A_{13}'	638	692	54	19	126.7
A_{14}	665	739	74		
A_{14}'	677	730	53	21	140.0
A_{15}	703	779	76		
A_{15}'	717	771	54	22	146.7

Table 6-1 Empirically determined plastic step heights.

The accuracy of the extracted depth information for each plastic step can be deduced from the graph in Fig. 6.5. The minimum and maximum residuals for the calculated depth in *Z*-axis for this experiment are of the order of $\{-6.7, +3.3\}$ mm.

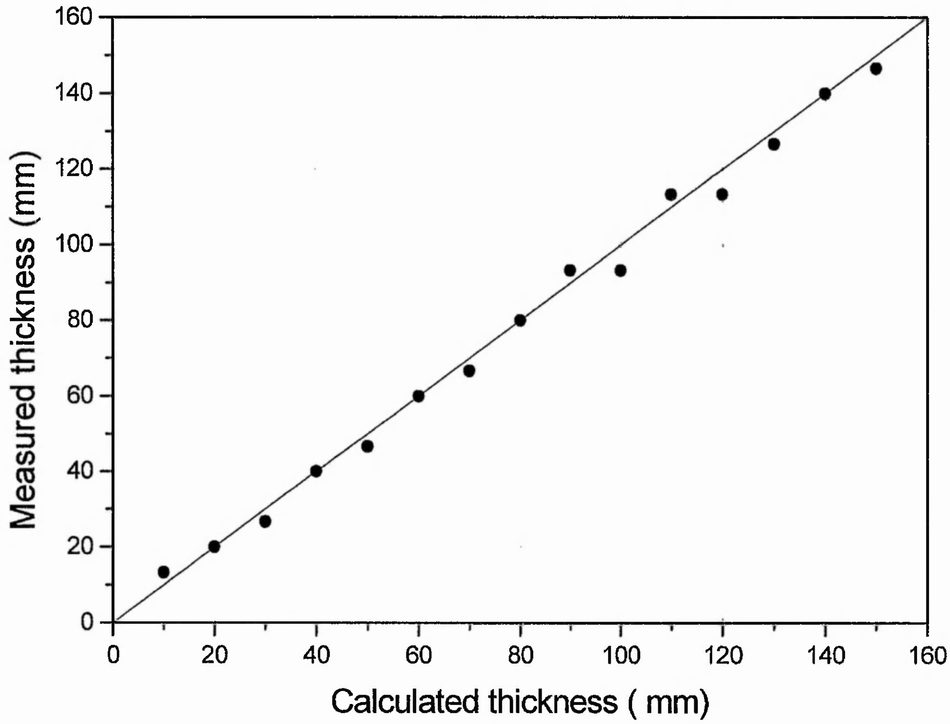

Fig. 6.5 Graph of the measured thickness versus the calculated thickness for the plastic stepwedge.

6.4 Experiments on Mass Density Extraction for a Plastic Stepwedge

The results obtained in Section 6.3.2 are used to evaluate the accuracy in calculating the mass density for each step of the plastic stepwedge. The mass density is calculated from Equation 2-22 on page 31:

$$\rho_{PL} = \frac{\rho_2 t_2}{t_{PL}\, a_{2PL}}$$

$$= \frac{t_2}{t_{PL} \times 1} \times 1.4\ g\ cm^{-3}$$

where mass density for plastic ρ_2=1.4 g/cm^3, t_2 is the thickness of basis material 2 (i.e. plastic) calculated from the polynomial fit equations derived in Chapter 5, t_{PL} is the calculated plastic step thickness from Table 6-1, and a_{2PL} =1 for a plastic target (PL).

The results of the characteristic angle and mass density calculated for the fifteen steps of the plastic stepwedge are tabulated in Table 6-2. It can be deduced from the table that the maximum percentage of error for the calculated mass density is -30.0%. This error is due to the inaccuracy of the polynomial fit in determining the quantity of t_2 and also the inaccuracy in determining plastic's thickness utilising the parallax data.

Steps	Calculated Characteristic Angle (Degree)	Calculated Mass Density (g cm^{-3})	Error in Calculated Mass Density (%)
1	90.6	0.98	-30.0
2	90.0	1.32	-5.7
3	88.8	1.44	2.9
4	88.8	1.30	-7.1
5	88.5	1.37	-2.1
6	88.5	1.29	-7.9
7	88.6	1.36	-2.9
8	88.5	1.29	-7.9
9	87.8	1.21	-13.6
10	88.2	1.36	-2.9
11	88.5	1.25	-10.7
12	88.4	1.36	-2.9
13	88.5	1.32	-5.7
14	88.4	1.27	-9.3
15	88.3	1.27	-9.3

Table 6-2 The calculated characteristic angle and mass density for each of the fifteen steps of the plastic stepwedge.

6.5 Experiments on Mass Density Extraction for Baggage Sample-7 and Sample-8

Fig. 6.6 and Fig. 6.7 illustrate the detection of a plastic target, (PL) in baggage sample-7 and sample-8. These each contain overlapping materials including clothing, newspaper, keys and coins. The result in searching for the target material (i.e. highlighted in Fig. 6.6(b) and Fig. 6.7(b)) illustrated in Fig. 6.6(a) and Fig. 6.7(a), are listed in Table 6-3. The experiments utilise the calculated thickness of the plastic target plate from Table 6-1 (i.e. 13.3 mm).

It can be deduced from the table that the percentage of error for the calculated mass density is -25.0% for baggage sample-7 and -22.9% for baggage sample-8. The error is a result of the inaccuracy of the polynomial curve fitting and the inaccuracy in determining the plastic's thickness.

	Calculated Characteristic Angle (Degree)	Calculated Mass Density (g cm^{-3})	Error in Calculated Mass Density (%)
PL in *Baggage-7*	90.6	1.05	-25.0
PL in *Baggage-8*	90.0	1.08	-22.9

Table 6-3 The calculated characteristic angle and mass density for the plastic target in baggage sample-7 and sample-8.

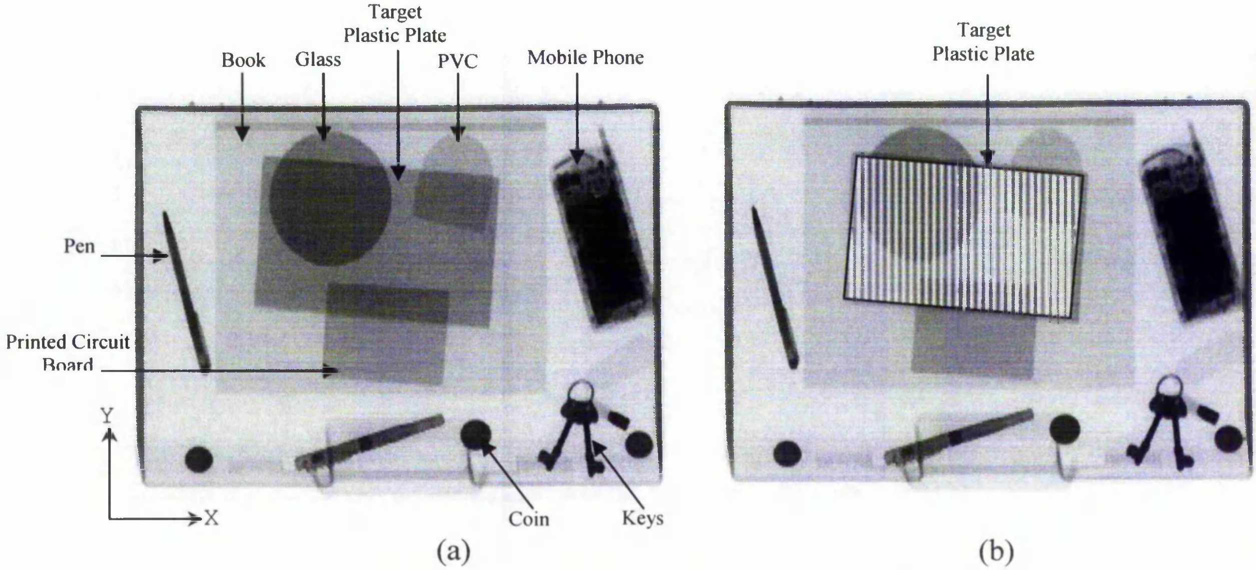

Fig. 6.6 Discriminating a plastic target in baggage sample-7.

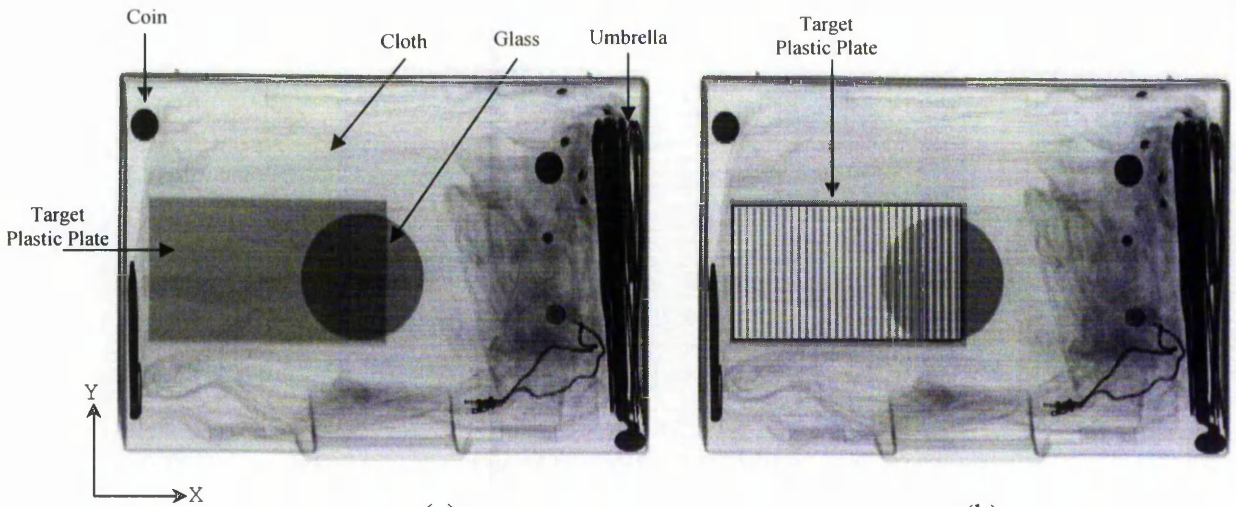

(a) (b)

Fig. 6.7 Discriminating a plastic target in baggage sample-8.

6.6 Summary

The examination of the parallax data indicates that the experimental system's resolution (Z-axis) is of the order of $\approx\pm6.7$ mm. The extraction of the depth data for more complicated radiographic images will require the location of conjugate image points automatically. This is very different from the contrived nature of target points implemented in this research. The automatic extraction of depth data (i.e. automatic correlation of conjugate image points) from the binocular stereoscopic image pairs is thus recommended as future work.

However, the course depth resolution δZ in object space for the experimental x-ray machine produces very significant error in the determination of the mass density of the target material. The empirical results indicate that the maximum percentage of error for the estimation of plastic plate's mass density is $\approx$-30.0% error even under well controlled and contrived experimental conditions. Although, it should be pointed out that the detection of bulk explosives may be more successful.

CHAPTER SEVEN

SUMMARY, CONCLUSIONS AND FUTURE WORK

7.1 Summary

A discussion of the results is presented throughout the main text of this thesis where appropriate.

Standard dual-energy x-ray techniques enable colour encoding of the resultant images in terms of organic, inorganic and metal substances. However, this crude materials discrimination technique can only be used as a general indicator of substances and is by no means a precise definition. As a result, the standard dual-energy x-ray technique will place plastic explosive in the same organic window as other harmless organic items. The potential solution to this problem presented in this research is the development of an automated materials discrimination technique. This has been achieved by developing and combining an automated image segmentation and categorisation algorithm with a basis materials subtraction (BMS) technique. The BMS technique is derived from the basis materials decomposition (BMD) technique and is exploited to extract the characteristic angle or effective atomic number for successfully segmented overlapping objects in baggage. The concept of the BMD technique has been utilised in medical imaging for tissue characterisation. Therefore, what is new in this research is the combining of the BMD and BMS analysis with the binocular stereoscopic dual-energy x-ray technique previously developed by TNTU team. This enables the decomposition of the stereoscopic dual-energy x-ray data into characteristic angle to search for the target materials. Additionally, the experimental stereoscopic system utilises a novel castellated dual-energy x-ray detector recently developed by the TNTU team. The castellated detector utilises half the number of scintillator-photodiodes in comparison to a conventional sandwich detector arrangement. Thus, it substantially reduces the sensor complexity and cost, and yet is proved capable of providing good materials discrimination capability and together with producing high quality monochrome and colour x-ray images.

A de-interlacing algorithm has been developed to remove the spatial interlace effect produced as a natural consequence of the castellated detector array. This enables the calibration of the experimental x-ray machine for organic, inorganic and metal discrimination capability. The experimental x-ray system's noise and repeatability were examined. Generally, the results are reasonable for broad materials discrimination. However, the accuracy of the BMS technique to detect target materials was much affected, since it is highly sensitive to the system noise and system repeatability[C6].

An automated x-ray image segmentation program utilising the wavelet transform technique was developed to segment overlapping objects in an x-ray image into individual regions for further quantitative analysis. The wavelet transform technique is derived from earlier research by Jean-Christophe Olivo[O2, O3] and Stephane Mallat[M5]. This work is expanded by the author to further categorise the segmented regions into overlapping and non-overlapping objects. In addition, the information that pertains to each segmented object that is surrounded or overlapped by other objects is determined automatically. This information is utilised for the investigation of characteristic angle and mass density extraction.

The BMD technique developed by R.E. Alvarez, A. Macovski and L.A. Lehmann[A2, L2] is extended (i.e. BMS technique) by the author to discriminate materials in baggage inspection for aviation security screening. A programme of experiments has established the feasibility of the BMS technique for the extraction of the characteristic angle from overlapping materials under certain conditions. An automated material recognition program combines the developed automated image segmentation and categorisation programs together with the BMS analysis.

The research was expanded to include a brief theoretical analysis of the stereoscopic depth extraction capability utilising the binocular stereoscopic dual-energy x-ray images produced by the experimental x-ray system. The depth measurements utilise parallax information obtained from conjugate image points located manually in the left and right perspective images. The conjugate points were easily identified in this research by placing lead spheres to mark the points of interest on the object under inspection. The successful extraction of the relative depth information from the stereoscopic dual-energy x-ray images is applied to determine an object's mass density. This extra information coupled with the calculated characteristic angle enables, in theory, a more accurate analysis of the target.

However, the accuracy in determining the characteristic angle and mass density values of a target material is significantly affected by the following factors:

- the minimum resolvable depth increment in object space is of the order of ±6.7 mm;
- unstable x-ray source output;
- non-uniform detector response;
- inaccuracy in the polynomial curve fitting for basis material calibration.

The calculation of the characteristic angle and mass density for layers of overlapping substances can only be determined provided that each layer has a discernable shape that can be segmented. Also, all the test objects utilised in this phase of work have uniform thickness. The ability to segment objects with non-uniform structure is problematic in terms of overlapping structure categorisation. This problem can only be resolved if the three-dimensional information at specific points on the imaged objects are known automatically. The automatic extraction of depth data from the binocular stereoscopic image pairs is therefore recommended as future work as a partial solution. It would be envisaged that the author's methodology could be incorporated in such a scheme.

The aluminium and plastic basis materials employed in this research, constrains the material discrimination to a window in effective atomic number of $6.6 \leq Z_{eff} \leq 13$ (i.e. 0°≤ characteristic angle ≤ 90°). Therefore, the technique will only work correctly if the materials masking the target material fall within the organic window defined by the chosen basis materials. Thus, for instance a metal mask would produce a false negative result.

Nevertheless, it is vital to acknowledge that there is no single technique that can be utilised to automatically search for target items concealed in passenger baggage. In fact, the variety of techniques that are presented in Chapter 1 will be required to detect a wide range of concealment techniques for target items such as plastic explosives.

The conclusions drawn from the work, and the direction and nature of the suggested future work are discussed in the remainder of this chapter.

7.2 Conclusions

The conclusions drawn from this research are categorised as following:

- The calibration of the experimental dual-energy x-ray machine.
- The development of an automated x-ray image segmentation and categorisation algorithm.
- The extraction of the characteristic angle of a target material.
- The extraction of depth data from the stereoscopic images in determining a material's mass density.

The castellated detector array is calibrated to enable further investigations to be conducted. The remainder of the research work has investigated the quantitative analysis capability of the experimental x-ray system in extracting characteristic angle and mass density for objects in baggage.

The calibration of the experimental dual-energy x-ray machine:

- The castellated detector array has reduced by half the number of scintillator-photodiode sensors in comparison to the conventional sandwich arrangement.

- The development of a de-interlacing enhancement algorithm to remove the spatial interlace effect in the x-ray images produced by the castellated sensors has been demonstrated. The spatial resolution of the sensor is similar to a sandwich sensor of the same pitch.

- The experimental system is calibrated to discriminate between organic, inorganic and metal substances automatically. The resultant images are colour encoded to enable visual inspection.

- The resultant colour encoded images are of high quality and of comparable imaging quality to images produced by sandwich detector arrays.

- The castellated detector array does not enable single sample (i.e. one pixel) materials discrimination. Nevertheless, the size of threat objects such as explosives in a security screening application will be very large in comparison to single pixel sample.

- The noise in the bright field (4095) grey level images produced by the experimental machine has a standard deviation of ±49.4.

- The system repeatability test on the grey level images indicated a maximum standard deviation of the order of ±7.2.

- Generally, the system noise and system repeatability results enable broad materials discrimination in terms of organic, inorganic and metal substances. However, the accuracy of the BMS technique to detect target materials is significantly affected by system noise and system repeatability.

The development of an automated x-ray image segmentation and categorisation algorithm:

- A wavelet based segmentation algorithm operates on the grey scale histogram of the low energy image. However, the choice is arbitrary and the high energy image would also be suitable choice for segmentation purposes.

- The limitation of the wavelet analysis occurs when the region of interest in an x-ray image is small compared to the background or when the region of interest and the background have a broad range of grey levels.

- The automatic segmentation program has been examined utilising a series of baggage samples containing uniform thicknesses of overlapping substances with a 'best' wavelet scale concluded from the experiments of 2^2.

- The maximum recorded standard deviation for the grey levels in a segmented region in the experiments is ± 10. This supports the concept that the image segmentation algorithms operate on clusters of homogeneous grey levels in an image.

- The segmentation results for spatially complex arrangements of overlapping materials requires intensive processing which could make it unsuitable for real time applications. In 'realistic' conditions, the problem could be resolved by only analysing a potential 'threat' with relatively low grey levels. Typically, threat items such as plastic explosives are dense and will be displayed in low grey level clusters in the resultant x-ray image.

- The x-ray image categorisation algorithms automatically extract the high energy and low energy data as the basis to further categorise the segmented regions into overlapping and non-overlapping regions.

The extraction of the characteristic angle of a target material:

- The basis materials decomposition (BMD) technique utilising aluminium and plastic as basis materials is employed in this research programme.

- The goodness of the polynomial curve fitting for the direct approximation BMD technique has minimum and maximum residuals for the estimation of t_1 of the order of {-4.20, +5.26} mm and t_2 of the order of {-13.93, +10.92} mm respectively. The inaccuracy of the polynomial fit tends to amplify the system error in searching for specific materials.

- The basis materials subtraction (BMS) technique enables the extraction of the characteristic angle from successfully segmented layers of overlapping substances in baggage. In general, this technique has been validated empirically. However, its accuracy is greatly affected by the system noise and the consequential inaccuracy in deriving the polynomial equations for the estimation of the basis materials thicknesses.

- The automated target recognition program combines the automated image segmentation and categorisation programs together with the BMS equations to extract the characteristic angle for overlapping objects.

The extraction of depth data from the stereoscopic images in determining a material's mass density:

- The examination of the empirical data suggested that the experimental system's Z-axis resolution is of the order of ± 6.7 mm.

- The measurement accuracy achievable in the Z-axis is limited by the constraints imposed by the binocular stereoscopic design theory. This is due to the limit placed on the display screen parallax by the human visual system which in turn limits the x-ray beam convergence angle.

- A preliminary investigation into utilising material thickness extracted from the stereoscopic parallax in the resultant images indicates that the depth resolution ($\approx\pm 6.7$ mm) of the experimental system is too coarse. Nevertheless, the mass density equations developed by L.A. Lehmann[L2] would enable a material that is concealed in luggage to be discriminated according to its relative characteristic angle and mass density, if the accuracy in material thickness is sufficiently good.

- The errors arising from determining the material's mass density are governed by the following factors:
    - The inaccuracy in determining the depth data (i.e. $\delta Z \approx \pm 6.7$ mm);

- Inaccurate polynomial fits for the BMD technique as a result of system noise.

In conclusion, the author suggests that the techniques developed may be appropriate for applications in other fields, such as industrial non-destructive inspection, especially in a combined stereoscopic visual inspection and quantitative analysis package.

7.3 Future Work

Energy-dependent systematic errors:

The fundamental assumption of the basis materials decomposition (BMD) technique is that the linear attenuation coefficient of any material at any given energy can be expressed as a linear combination of the linear attenuation coefficient of two basis materials, where the basis material coefficients are assumed to be independent of energy. The basis material coefficients are employed to discriminate unknown materials in this research programme. However, in general these coefficients are found to be energy dependent[G11, G12]. Therefore, the synthesized linear attenuation coefficients values utilising the BMD technique are expected to suffer from energy dependent systematic errors. Another assumption of the BMD technique is that the set of basis materials utilised best describe the attenuation coefficients of various materials to be discriminated. In aviation security screening, these are materials that are 'normally' found in passenger baggage together with threat items such as plastic explosives. As a result, the quantifying error will become significant if a high atomic number masking substance like metal is present in the x-ray image.

Nevertheless, the systematic errors can be reduced significantly by careful selection of new basis materials that best mimic the normal materials present in baggage by applying the *Basis Material Coefficients Transformation Method*[G11, G12]. The advantage of this technique is that it enables the energy-dependent systematic errors inherent in the calibration of the aluminium and plastic basis materials to be numerically transformed to cover a wider range of materials in terms of effective atomic number Z_{eff} . The success of this method would rely on measuring the effective energies of the polychromatic x-ray spectra produced by the experimental x-ray machine. The effective energies are defined as the mean x-ray energies detected by the dual-energy sensors.

Multiple-view x-ray system:

There are currently two views taken of the examined object, it therefore seems that any attempt to find a mass model of the bag that is sufficiently accurate for the purposes of target recognition will be difficult or impossible under realistic screening conditions. The problem will tend to become worse with increasing image complexity. In a multiple-view x-ray system, there would be significantly increased coordinate information[H12] available. Also better measurement accuracy in the depth axis in the object space could be achieved, while retaining improved visual inspection capability. The multiple-view x-ray system can be realised by utilising a single x-ray source to produce a number (6 to 16) of collimated x-ray beams incident on their respective folded linear detector arrays. Since the castellated detector array has reduced by half the number of dual-energy sensor elements, the implementation of multiple-view x-ray screening system could be accomplished in a practical manner.

Automatic correlation of conjugate image points:

The stereoscopic images by their very nature contain three-dimensional information. This research programme has in part been concerned with the extraction of the depth information in an attempt to determine a material's mass density. A critical aspect of this research in terms of a practical solution would be the ability to locate the conjugate image points in the left and right perspective images automatically. Thus, enabling an object's spatial distribution and consequently its mass density to be resolved automatically.

The research programme presented in this thesis is theoretical in nature and is limited to simple arrangements of object structures. It is anticipated that the complexity of the object under inspection will have a critical bearing on the ability of the system to locate target items. In particular, it is also anticipated that structures that cause overlapping of suspect devices in the resultant images would still be problematic. Therefore, a scheme for better quantifying this effect will require devising in conjunction with the multiple-view x-ray imaging technique.

Thus in conclusion the author suggests that each of the recommended areas of future work be further investigated, since they all represent substantial potential improvements to the techniques already developed.

Publications

1. WANG T.W., EVANS J.PO., 'Stereoscopic Dual-energy X-ray Imaging for Target Materials Identification', *IEE Proceedings – Vision, Image and Signal Processing*, submitted Dec 2001 (accepted for publication).

References

A1 ARIYAEEINIA A.M., 'An active co-ordinate imaging system for robot vision', Trent Polytechnic, PhD Thesis, 1985.

A2 ALVAREZ R.E., MACOVSKI A., 'Energy-selective reconstructions in X-ray computerized tomography', *Phys. Med. Biol.,* Vol. 21, No. 5, pp. 733-744, 1976.

A3 ANNIS M., BJORKHOLM P., SCHAFER D., 'Automatic Detection of Explosives Using X-ray Imaging', *Access Security Screening: Challenges & Solutions*, ASTM STP 1127, pp. 68-81, 1992.

A4 ALVAREZ R.E., 'Experimental comparison of dual energy X-ray image detectors' *SPIE Proceedings*, Vol. 2708, pp. 534-543, 1996.

B1 BRODY W.R. ET AL., 'A method for selective tissue and bone visualization using dual energy scanned projection radiography', *Med. Phys.*, Vol. 8, pp. 353-357, 1981.

B2 BENTUM M.J., ARENDSEN R.G.J., SLUMP C.H., 'Design and Realization of High Speed Single Exposure Dual Energy Image Processing', *5th Annual IEEE Symposium on Computed-Based Medical Systems*, pp. 25-34, 1992.

B3 BEEVOR S.P., SANDER J., RAITT I., BURROWS J.D., MANN K., 'Non-invasive inspection of baggage using coherent X-ray scattering', *Journal of Defence Science*, Vol.1, No. 1, pp. 102-106, 1996.

B4 BJORKHOLM P.J., WANG T.R., 'Contraband Detection Using X-rays with Computer Assisted Image Analysis', *Contraband and Cargo Inspection Technology International Symposium, Sponsored by: Office of National Drug*

Control Policy and National Institute of Justice, pp.99-103, Washington, D.C., U.S.A., 111-115 Oct. 1992.

B5 BELTRAN J.R., BELTRAN F., ESTOPANAN A., 'Multiresolution edge detection and classification: noise characterization', *IEEE International Conference on Systems, Man, and Cybernetics*, Vol. 5, pp. 4476-4481, 1998.

C1 COLIN N., J. DERWIN K., 'Selective gamma ray resonant absorption for explosives detection', *Proceeding of the 1st International Symposium on Explosive Detection Technology*, pp. 333-345, Nov. 13-15, 1991.

C2 COENEN J.G.C., MAAS J.G., 'Material classification by dual-energy computerized X-ray tomography', *International Symposium on Computerized Tomography for Industrial Applications*, pp. 120-127, June 1994.

C3 CHRISTENSEN E.E., CURRY T.S., NUNNALLY J., 'An Introduction to the Physics of Diagnostic Radiology', Lea and Feibiger - Philadelphia, pp. 196-223, 1972.

C4 CHEN P., WANG Y., 'Multicriterion Compton backscatter imaging', *IEE Proceedings of Science, Measurement and Technology*, Vol. 143, No. 6, pp. 357-361, November 1996.

C5 CUZIN M., GLASSER F., LAJZEROWICZ J., MATHY F., VERGER L., 'Applications of CdTe detectors in X-ray imaging and metrology', *SPIE Proceedings of X-ray Detector Physics and Applications II*, Vol. 2009, pp. 192-202, 1993.

C6 CHUANG K.S., HUANG H.K., 'Comparison of four dual energy image decomposition methods', *Phys. Med. Biol.*, Vol. 33, No. 4, pp. 455-466, 1988.

C7 CHYE H.Y., WHALEN R.T., BEAUPRE G.S., YEN S.Y., NAPEL S., 'Reconstruction algorithm for polychromatic CT imaging: application to beam hardening correction', *IEEE Transactions on Medical Imaging*, Vol. 19, No.1, pp. 1-11, Jan. 2000.

D1 DAVSON H., 'Davson's Physiology of the Eye, 5th Edition', Macmillan Press London, pp. 449-485, 1990.

D2 DAVIES E.R., 'Machine Vision', Academic Press, London, 1990.

D3 DEV P.C., GARY T.B., 'An energy sensitive cassette for dual-energy mammography', *Med. Phys.*, Vol. 16, No. 1, pp. 7-13, 1989.

D4 DEV P.C., GARY T.B., 'Bone mineral densitometry with X-ray and radionuclide sources: A theoretical comparison', *Med. Phys.*, Vol. 18, No. 5, pp. 978-984, 1991.

D5 DUVAUCHELLE P., FREUD N., KAFTANDJIAN V., BABOT D., 'A computer code to simulate X-ray imaging techniques', *Nuclear Instruments & Methods in Physics Research Section B-Beam Interactions with Materials & Atoms*, Vol. 170, No.1-2, pp. 245-258, Sept. 2000.

E1 EVANS J.P.O., 'Castellated linear array system', British Pat. Appl. 99147005.0, Filed 23rd June 1999.

E2 ESAM M.A.H., 'Detection of explosive materials using nuclear radiation: a critical review', *SPIE Proceeding*, Vol. 1736, pp.130-137, 1992.

E3 EVANS J.P.O., ROBINSON M., 'The Development of 3D X-ray equipment for security Systems', *Contraband and Cargo Inspection Technology International Symposium, Sponsored by: Office of National Drug Control Policy and National Institute of Justice*, pp.99-103, Washington, D.C., U.S.A., 28-30 Oct. 1992.

E4 EVANS J.P.O., ROBINSON M., 'The development of 3D X-ray systems for airport security applications', *SPIE Proceeding: Applications of Signal and Image Processing in Explosives Detection Systems*, Vol. 1824, pp. 171-182, Boston Massachusetts, U.S.A., 16-17 Nov. 1992.

E5 EVANS J.P.O., GODBER S.X., ROBINSON M., 'Stereoscopic X-ray systems for airport security applications', *4th European Workshop on Three-Dimensional Television*, pp. 97-101, Rome, Italy, Oct. 1993.

E6 EVANS J.P.O., 'Development of a 3-D X-ray system', The Nottingham Trent University, PhD Thesis, 1993.

E7 EVANS J.P.O., GODBER S.X., ROBINSON M., 'Three-dimensional X-ray imaging techniques', *SPIE Proceeding: Symposium on Electronic Imaging Science and Technology in Stereoscopic Displays and Applications V*, Vol. 2177, pp. 161-165, California, U.S.A., Feb. 1994.

E8 EVANS J.P.O., ROBINSON M., GODBER S.X., 'A new stereoscopic imaging technique using a single X-ray source: theoretical analysis', *Journal of Non-Destructive Testing and Evaluation International (NDT&E)*, pp. 27-35, Feb. 1996.

E9 EVANS J.P.O., ROBINSON M., GODBER S.X., PETTY R.S., 'The Development of 3-D (Stereoscopic) Imaging Systems for Security Applications', *29th IEEE International Carnahan Conference*, pp. 505-511, Sanderstead, Surrey, UK, Oct.1995.

E10 EVANS J.P.O., GODBER S.X., ROBINSON M., 'The derivation of 2½-D image models from one-dimensional X-ray image sensors', *SPIE Proceeding: Symposium on Electronic Imaging Science and Technology in Stereoscopic Displays and Virtual Reality Systems III*, Vol. 2653, pp. 189-193, California, U.S.A., Feb. 1996.

E11 EVANS J.P.O., ROBINSON M., GODBER S.X., 'Identification of volume elements in a 3-D X-ray imaging system', *IEE Electronics Letters*, Vol. 32, No. 7, pp. 644-645, March 1996.

E12 EVANS J.P.O., ROBINSON M., GODBER S.X., '3-D X-ray Image Modelling - Latest Developments', *IEE Publication No: 437, European Conference on Security and Detection*, pp.1-4, London, UK, April 1997.

E13 EVANS J.P.O., ROBINSON M., 'Line-scan imaging in 3-D', British Pat. Appl. 9720864.9, Filed 1st Oct. 1997.

E14 EVANS J.P.O., ROBINSON M., 'Testing and Evaluation of an Advanced (3-D) X-ray Imaging System', *32nd IEEE International Carnahan Conference*, pp. 50-54, Alexandria, Virginia, USA, Oct., 1998.

E15 EVANS J.P.O., ROBINSON M., 'Design of a stereoscopic X-ray imaging system using a single X-ray source', *Journal of Non-Destructive Testing and Evaluation International (NDT&E)*, Vol. 33, No. 5, pp. 325-332, July 2000.

E16 EVANS J.P.O., ROBINSON M., 'A binocular stereoscopic X-ray imaging technique using folded array linear X-ray detectors', *Institute of Physics: Journal of Measurement Science and Technology*, No. 13, pp. 1388-1397, July 2002.

E17 EVANS B.L., MARTIN J.B., BURGGRAF L.W., ROGGEMANN M.C., 'Nondestructive inspection using Compton scatter tomography', *IEEE Transactions on Nuclear Science*, Vol. 45, No. 3, pp. 950-956, June 1998.

F1 FORMAN A.T., 'Depth measurement in three-dimensional television images', Trent Polytechnic, Project Report, 1983.

F2 FRIEND D.B., JONES A., 'A stereoscopic television system for reactor inspection', C.E.G.B. Research Division, March 1980.

F3 FUQIANG Z., DAZONG J., 'Multiple decomposition technique for dual energy X-ray image', *Engineering in Medicine and Biology Society, Proceedings of the Annual International Conference of the IEEE*, Vol. 5, pp. 1778 –1779, 1992.

F4 FREDRICK L.R., 'The Evolution Of Computed Tomography (CT) As An Explosives Detection Modality', *Proceeding of the 1st International Symposium on Explosive Detection Technology*, pp. 297-308, Nov. 13-15, 1991.

F5 FIORETTO E., INNOCENTI F., VIESTI G., CINAUSERO M., ZUIN L., FABRIS D., LUNARDON M., NEBBIA G., PRETE G., 'CsI(Tl)-photodiode detectors for gamma-ray spectroscopy', *IEEE Transactions on Nuclear Science*, Vol. 47, No. 4, pp. 1315 –1318, Aug. 2000.

F6 FOGELMAN I., BLAKE GM., 'Different approaches to bone densitometry', *Journal of Nuclear Medicine*, Vol. 41, No.12, pp. 2015-2025, Dec. 2000.

G1 GRODZINS L., 'Photons in-photons out: Non-destructive Inspection of Containers using X-ray and Gamma Ray Techniques', *Proceeding of the 1st International Symposium on Explosive Detection Technology*, pp. 201-231, Nov. 1991.

G2 GEOFFREY H., 'Optimization criteria for CXRS baggage inspection', *SPIE Proceeding*, Vol. 2511, pp.64-70, 1995.

G3 GOZANI T., 'Advances in accelerator based explosives detection systems', *Nuclear Instruments and Methods in Physics Research*, Vol. B79, pp. 601-604, 1993.

G4 GONZALEZ R.C., WINTZ P., 'Digital Image Processing', Addison-Wesley Publishing Company, pp. 30-33, 1987.

G5 GARY T.B., RICHARD A.S., MIKE M.T., DOUGLAS R.M., JOHN N.S., 'Detector for Dual-Energy Digital Radiography', *Radiology*, Vol. 156, pp. 537-540, 1985.

G6 GIAKOS G.C., PILLAI B., CHOWDHURY S., DASGUPTA A., GUNTUPALLI R., SURYANARAYANAN S., 'Sensitometric response of CdZnTe detectors for digital radiography', *IEEE Proceedings of Sensing, Processing and Networking: Instrumentation and Measurement Technology Conference*, Vol. 1, pp. 12-15, 1997.

G7 GROSSMANN A., MORLET J., 'Decomposition of Hardy functions into square integrable wavelets of constant shape', SIAM J. Math, Vol. 15, pp. 723-736, 1984.

G8 GIAKOS G.C., CHOWDHURY S., SHAH N., VEDANTHAM S., PASSERINI A.G., SURYANARAYANAN S., MEHYA K., SUMRAIN S., SCHEIBER C., 'Dual-energy measurements utilizing a novel multimedia detector', *The 17th IEEE Proceedings of Instrumentation and Measurement Technology*, Vol. 2, pp. 607-610, 2000.

G9 GUY M.J., CASTELLANO-SMITH I.A., FLOWER M.A., FLUX G.D., OTT R.J., VISVIKIS D., 'DETECT-dual energy transmission estimation CT-for improved attenuation correction in SPECT and PET', *IEEE Transactions on Nuclear Science*, Vol. 45, No. 3, pp. 1261-1267, June 1998.

G10 GINGOLD E.L., HASEGAWA B.H., 'Dual-Energy X-ray Processing for Quantitative Projection Imaging', *IEEE Nuclear Science Symposium*, pp. 1147-1150, 1990.

G11 GOH K.L., LIEW S.C., HASEGAWA B.H., 'Energy-Dependent Systematic Errors in Dual-Energy X-ray CT', *IEEE Transactions on Nuclear Science*, Vol. 44, No. 2, pp. 212-217, April 1997.

G12 GOH K.L., LIEW S.C., HASEGAWA B.H., 'Correction of Energy-Dependent Systematic Errors in Dual-Energy X-ray CT using a Basis Material Coefficients Transformation Method', *IEEE Transactions on Nuclear Science*, Vol. 44, No. 6, pp. 2419-2424, Dec. 1997.

H1 HARDING G., NEWTON M., KOSANETZKY J., 'Energy-dispersive X-ray diffraction tomography', *Phys. Med. Biol.*, Vol. 35, No. 1, pp. 33-41, 1990.

H2 HELMUT S., 'Simulation-based training and testing of classification schemes for CXRS explosive detection', *SPIE Proceeding*, Vol. 2511, pp.88-98, 1995.

H3 HASSLER U., GARNERO L., RIZO P., 'X-Ray Dual-Energy Calibration Based on Estimated Spectral Properties of the Experimental System', *IEEE Transactions on Nuclear Science*, Vol. 45, No. 3, pp. 1699-1712, June 1998.

H4 HOBBIE R.K., 'Interaction of photons and charged particles with matter', *Nuclear Medical Physics*, Vol. 1, pp. 65-141, 1987.

H5 HARALICK R.M., SHAPIRO L.G., 'Glossary of computer vision terms', *Pattern Recognition*, Vol. 24, No. 1, pp. 69-93, 1991.

H6 HORN B.K.P., 'Robot Vision', MIT Press, London, 1986.

H7 HIROSHI T., TETSURO O., KOICHI O., SUEKI B., 'CdTe Semiconductor X-ray Imaging Sensor and Energy Subtraction Method Using X-ray Energy Information', *IEEE Transactions On Nuclear Science*, Vol. 40, No. 2, pp. 95-101, April 1993.

H8 HITOMI K., MUROI O., MATSUMOTO M., HIRABUKI R., SHOJI T., HIRATATE Y., 'X-ray detection characteristics of thallium bromide nuclear radiation detectors', *IEEE Transactions on Nuclear Science*, Vol. 47, No. 3, pp. 777-779, June 2000.

H9 HO J.T., PARKER D.L., 'K-edge Filtration In Dual-energy, Single-exposure Chest Radiography', *Proceedings of the Twelfth Annual International Conference of the IEEE Engineering in Medicine and Biology Society*, Vol. 12, No.1, pp. 470-471, 1990.

H10 HASSLER U., RIZO P., 'Segmentation and density-evaluation of fiber-reinforced materials by dual-energy computed tomography', *Review of Progress in Quantitative Nondestructive Evaluation*, Vol. 15, pp. 473-480, 1996.

H11 HENRI C.J., PETERS T.M., 'Evaluation of perceived distortions in stereoscopic images', *First Conference on Visualisation in Biomedical Computing, Atlanta, Georgia, IEEE Computer Society Press*, pp. 216-222, May, 1990.

H12 HON H.W., 'The Modelling of Multiple Beam X-ray Systems Using Visible Light', The Nottingham Trent University, PhD Thesis, 2000.

I1 ISHIGAKI T. ET AL., 'One-shot Dual-energy Subtraction Imaging', *Radiology 161*, pp. 271-273, 1986.

I2 IVANOV O.P., STEPANOV V.E., SUDARKIN A.N., VOLKOVICH A.G., URUTSKOEV L.I., 'An algorithm for material density reconstruction from X-ray images of field of compton scattering obtained with HERV', *IEEE: Nuclear Science Symposium and Medical Imaging Conference*, Vol. 1, pp. 52 –55, 1995.

J1 JUPP I.D., DURRANT P.T., RAMSDEN D., CARTER T., DERMODY G., PLEASANTS I.B., BURROWS D., 'The non-invasive inspection of baggage using coherent X-ray scattering', *IEEE Transactions on Nuclear Science*, Vol. 47, No. 6, pp. 1987 –1994, Dec. 2000.

J2 JONES A., 'Some theoretical aspects of the design of stereoscopic television systems', C.E.G.B. Research Division, March 1980.

J3 JACOBSON B., 'Dichromatic absorption radiography: dichromography', *Acta Radiol.*, Vol. 39, pp. 436-452, 1953.

J4 JENKINS R., GOULD R.W., GEDCKE D., 'Quantitative X-ray Spectrometry', Marcel Dekker INC, 1981.

K1 KRISTOPH D. KRUG, JAY A. STEIN, 'Advanced Dual Energy X-ray For Explosives Detection', *Proceeding of the 1st International Symposium on Explosive Detection Technology*, pp. 282-284, Nov. 1991.

K2 KANG S.B., WEBB J.A., ZITNICK C.L., KANADE T., 'A multibaseline stereo system with active illumination and real-time image acquisition', *Proceeding 5th International Conference on Computer Vision*, pp. 88-93, USA, June 1995.

K3 KLEIMANN P., LINNROS J., FROJDH C., PETERSSON C.S., 'An X-ray imaging pixel detector based on a scintillating guides screen', *IEEE Transactions on Nuclear Science*, Vol. 47, No. 4, pp. 1483-1486, Aug. 2000.

K4 KIM N.D., UDPA S., 'Nonlinear operators for edge detection and line scratch removal', *IEEE International Conference on Systems, Man, and Cybernetics*, Vol. 5, pp. 4401-4404, 1998.

K5 KONOVALOV A.V., VOLEGOV P.L., DMITRAKOV Y.L., 'A simple method for CT-scanner calibration against effective photon energy', *Pribory i Tekhnika Eksperimenta*, No. 3, pp. 122-126, May-June 2000.

L1 LYNNE H., 'Materials discrimination at high energies and the effects of afterglow in scintillating crystals', Cranfield University, MPhil Thesis, 1998.

L2 LEHMANN L.A., ALVAREZ R.E., MACOVSKI A., BRODY W.R., 'Generalized image combinations in dual KVP digital radiography', *Med. Phys.*, Vol. 8, No. 5, pp. 659-667, Sept./Oct. 1981.

L3 LAPRADE G.L., 'The Manual of Photogrammetry', Fourth Edition, American Society of Photogrammetry, pp. 519-544, 1980.

L4 LUGGAR R.D., HORROCKS J.A., FARQUHARSON M.J., SPELLER R.D., LACEY R.J., 'Real time analysis of scattered X-ray spectra for sheet explosives detection', *SPIE Proceeding*, Vol. 2936, pp.219-228, 1997.

L5 LEE S.U., CHUNG S.Y., PARK R.H., 'A comparative performance study of several global thresholding techniques for segmentation', *Comput. Vision Graphics Image Processing*, Vol. 52, pp. 171-190, 1990.

L6 LI H.B., LIU Y., CHANG C.C., CHANG C.Y., CHAO J.H., CHEN C.P., 'A CsI(Tl) scintillating crystal detector for the studies of low-energy neutrino interactions', *Nuclear Instruments & Methods in Physics Research Section A-Accelerators Spectrometers Detectors & Associated Equipment*, Vol. 459, No. 1-2, pp. 93-107, Feb. 2001.

M1 MOULD R.F., 'A History of X-rays and Radium', IPC Building and Contract Journals Ltd., IPC Business Press, 1980.

M2 MACOVSKI A., ALVAREZ R.E., CHAN J.L., STONESTROM J.P., ZATZ L.M., 'Energy dependent reconstruction in X-ray computerized tomography', *Comput. Biol. Med.*, Vol. 6, pp. 325-336, 1976.

M3 MAYHEW J.E.W., FRISBY J.P., '3D Model Recognition from Stereoscopic Cues', MIT Press, 1991.

M4 MOUSAVI M.S., SCHALKOFF R.J., 'A neural network approach for stereo vision', *SOUTHEASTCON 90*, Vol. 3, pp. 808-812, USA, April 1990.

M5 MALLAT S., 'Zero-Crossings of a Wavelet Transform', *IEEE Transactions on Information Theory*, Vol. 37, No. 4, pp. 1019-1033, July 1991.

N1 NALCIOGLU O., LOU R.Y., Paper No. 244 presented at the 63rd Annual Meeting of the Radiology Society of North America, Chicago, IL, 1977.

O1 OKOSHI T., 'Three-dimensional Imaging Techniques', Academic Press, pp. 49-59, 1976.

O2 OLIVO J.C., 'Image segmentation by wavelet-based automatic threshold selection', *SPIE Proceedings*, Vol. 2094, pp. 1159-1172, 1993.

O3 OLIVO J.C., 'Automatic Threshold Selection Using the Wavelet Transform', *CVGIP: Graphical Models and Image Processing*, Vol. 56, No. 3, pp. 205-218, May 1994.

P1 PERINI M., 'Single camera 3-D system', Trent Polytechnic, 1984.

P2 PONG T.C., KENNER M.A., OTIS J., 'Stereo/motion cues in pre-attentive vision processing: some experiments with random dot stereographic image sequences', *IEEE Proceeding of the workshop on visual motion*, pp. 314-320, March 1989.

R1 ROBINSON M., SOOD S.C., 'Real-time depth measurement in a stereoscopic television display', *SPIE Annual Technical Symposium*, Vol. 367, pp. 34-40, 1982.

R2 ROBINSON M., SOOD S.C., 'Calibration and depth resolution of a stereoscopic video display', *SPIE Proceeding*, Vol. 402, pp. 162-165, 1983.

R3 ROBINSON M., 'Three-dimensional vision for bomb disposal', *8th International Conference on Special Equipment for the Police*, INTERPOL HQ, Paris, Nov. 1983.

R4 ROBINSON M., 'Remote control vehicle guidance using stereoscopic displays', *Proceedings U.S. Human Factors Soc.*, Vol. 28, 1984.

R5 ROBINSON M., ARIYAEEINIA A.M., 'An active co-ordinate imaging system for robot vision', *SPIE Applications of Artificial Intelligence*, Vol. 657, pp. 141-151, 1986.

R6 ROBINSON M., '3-D Television for teleoperator, measurement, and robot vision applications', *Proceeding of International Workshop on Nuclear Robotic Technologies*, Vol. 3, paper 18, 1987.

R7 ROBINSON M., SHUTTLEWORTH P., 'Visual feedback for robotic manipulator control', *Proceeding of 8th International Conference on Robot Vision and Sensory Control*, pp. 65-70, May 1989.

R8 RUTHERFORD R.A., PULLAN B.R., ISHERWOOD I., 'Measurement of Effective Atomic Number and Electron Density Using an EMI Scanner', *Neuroradiology*, Vol. 11, pp. 15-21, 1976.

R9 RODER F.L., 'The Evolution of Computed Tomography (CT) As An Explosives Detection Modality', *Proceeding of the 1st International Symposium on Explosive Detection Technology*, pp. 297-308, Nov 1991.

R10 RICHARD F.E., KRISTOPH D.K., 'Aspects of image recognition in Vivid Technology's dual-energy X-ray system for explosive detection', *SPIE Proceeding: Applications of Signal and Image Processing in Explosives Detection Systems*, Vol. 1824, pp. 127-143, Boston Massachusetts, U.S.A., 16-17 Nov. 1992.

R11 RAMESH N., YOO J.H., SETHI I.K., 'Thresholding based on histogram approximation', *IEE Proceedings of Vision Image Signal Processing*, Vol. 142, No. 5, pp. 271-279, Oct. 1995.

S1 SPELLER R.D., HORROCKS J.A., LACEY R., 'X-ray scattering signatures for material identification', *SPIE Proceeding*, Vol. 2092, pp.366-377, 1993.

S2 SPELLER R.D., MALDEN C., EVELYN NG., HORROCKS J.A., LUGGAR R.D., LACEY R., 'System tuning for X-ray scatter measurements in explosive detection', *SPIE Proceeding*, Vol. 2936, pp.191-200, 1997.

S3 SHUTTLEWORTH P.J., 'Visual feedback for robot manipulator control', Trent Polytechnic, PhD Thesis, 1989.

S4 SHUTTLEWORTH P., ROBINSON M., 'Vision guided robot control', *International Conference on Intelligent Autonomous Systems 2*, pp. 459-464, Dec. 1989.

S5 SPOTTISWOODE R., SPOTTISWOODE N.L., SMITH C., 'Basic principles of the three-dimensional film', *Journal of the SMPTE*, pp. 249-286, Oct. 1952.

S6 SPELLER R.D., ENSELL G.J., 'A system for dual-energy radiography', *British Journal of Radiography*, Vol. 56, pp. 461-465, 1983.

S7 STRECKER H., HARDING G., BOMSDORF H., KANZENBACH J., LINDE R., MARTENS G., 'Detection of Explosives in Airport Baggage Using Coherent X-ray Scatter', *SPIE Proceeding*, Vol. 2092, pp. 399-410, 1993.

S8 SPEES G., MUNIER B., ROZIERE G., PRIEUR P., ROUGEOT H., 'Solid-state linear detector for X-ray digital imaging', *The American Soc. for NDT Inc., Materials Evaluation*, No. 48, pp. 326-327, March 1990.

S9 SIDDIQUE J.I., BARNER K.E., 'Wavelet-based multiresolution edge detection utilizing gray level edge maps', *International Conference on Image Processing*, Vol. 2, pp. 550-554, 1998.

S10 SEIBERT J.A., POAGE T.F., ALVAREZ R.E., 'Dual energy radiography using active detector technology', *IEEE Nuclear Science Symposium*, Vol. 2, pp. 1244-1247, 1996.

S11 SKIPPER J.A., HANGARTNER T.N., 'Optimizing X-ray spectra for dual-energy radiographic bone densitometry', *IEEE Proceedings of the Biomedical Engineering Conference*, pp. 297-300, 1996.

S12 SUKOVIC P., CLINTHORNE N.H., 'Design of an experimental system for dual energy X-ray CT', *IEEE Nuclear Science Symposium*, Vol. 2, pp. 1021-1022, 2000.

S13 SUKOVIC P., CLINTHORNE N.H., 'Basis material decomposition using triple-energy X-ray computed tomography', *IEEE Proceedings of the Instrumentation and Measurement Technology*, Vol. 3, pp. 1615-1618, 1999.

S14 SUKOVIC P., CLINTHORNE N.H., 'Penalized weighted least-squares image reconstruction for dual energy X-ray transmission tomography', *IEEE Transactions on Medical Imaging*, Vol. 19, No. 11, pp. 1075-1081, Nov. 2000.

T1 TSAHI G., 'Advances in accelerator based explosives detection systems', *Nuclear Instruments and Methods in Physics Research*, Vol. B79, pp. 601-604, 1993.

T2 TYCHSEN L., 'Adler's Physiology of the Eye, 9th Edition', Mosby-Year Book Inc., pp. 773-853, 1992.

T3 TETSURO O., HIROSHI T., KOICHI O., SUEKI B., 'X-ray Imaging Sensor using CdTe Crystals for Dual Energy X-ray Absorptiometry', *IEEE Transactions On Nuclear Science*, Vol. 41, No. 5, pp. 1740-1745, Oct. 1994.

T4 PARANJAPE R., SLUSER M., RUNTZ K., 'Segmentation of handguns in dual energy X-ray imagery of passenger carry-on baggage', *IEEE Canadian Conference on Electrical and Computer Engineering*, Vol. 1, pp. 377-380, 1998.

T5 TREMSIN A.S., PEARSON J.F., NICHOLS A.P., OWENS A., BRUNTON A.N., FRASER G.W., 'X-ray-induced radiation damage in CsI, Gadox, Y/sub 2/O/sub 2/S and Y/sub 2/O/sub 3/ thin films', *Nuclear Instruments & Methods in Physics Research Section A-Accelerators Spectrometers Detectors & Associated Equipment*, Vol. 459, No. 3, pp. 543-551, March 2001.

V1 VALYUS N.A., 'Stereoscopy', The Focal Press, 1966.

W1 WANG T.R., BJORKHOLM P.J., SCARLET R., GOLDBERG S., 'Explosive detection using X-rays and thermal neutron activation', *Proceeding of the 1st International Symposium on Explosive Detection Technology*, pp. 309-310, Nov. 13-15, 1991.

W2 WILLI A. KALENDER, ERNST KLOTZ, LENA KOSTARIDOU, 'An Algorithm for Noise Suppression in Dual Energy CT Material Density Images', *IEEE Transactions on Medical Imaging*, Vol. 7, No. 3, pp. 218-224, Sept. 1988.

W3 WAGNER F.C., MACOVSKI A., NISHIMURA D.G., 'Effects of Scatter in Dual-Energy Imaging: An Alternative Analysis', *IEEE Transaction on Medical Imaging*, Vol. 8, No. 3, pp. 236-244, Sept. 1989.

W4 WELCH A., GULLBERG G.T., CHRISTIAN P.E., LI J., TSUI B.M.W., 'An investigation of dual-energy transmission measurements for more accurate non-uniform attenuation compensation in cardiac SPECT', *IEEE Nuclear Science Symposium and Medical Imaging Conference*, Vol. 4, pp. 1558-1562, 1995.

W5 WOJCIK R., MAJEWSKI S., PARKER F.R., WINFREE W.P., 'Single shot dual energy reverse geometry X-radiography (RGX)', *IEEE Nuclear Science Symposium*, Vol. 2, pp. 811-815, 1996.

W6 WILLIAM H.P., SAUL A.T., WILLIAM T.V., BRIAN P.F., 'Numerical Recipes in C – The Art of Scientific Computing', 2nd Edition, Cambridge University Press, 1995.

Y1 YAN C.H., WHALEN R.T., BEAUPRE G.S., YEN S.Y., NAPEL S., 'Reconstruction algorithm for polychromatic CT imaging: application to beam hardening correction', *IEEE Transactions on Medical Imaging*, Vol. 19, No. 1, pp. 1-11, Jan. 2000.

Y2 YOU J., BHATTACHARYA P., 'A wavelet-based coarse-to-fine image matching scheme in a parallel virtual machine environment', *IEEE Transactions on Image Processing*, Vol. 9, No. 9, pp. 1547 –1559, Sep. 2000.

APPENDIX A

Calibration data for the plastic, aluminium and steel stepwedges

Steps	HI*	LO*	HI*-LO*
1	3090	2900	190
2	2270	2060	210
3	1710	1500	210
4	1270	1080	190
5	962	806	156
6	729	587	142
7	558	442	116
8	433	327	106
9	329	244	85
10	250	192	58
11	187	148	39
12	142	119	23
13	110	89	21
14	89	73	16
15	65	55	10

* Grey levels (12-bit)

Table A-1 Transmitted HI and LO energy data for the plastic stepwedge.

Steps	HI*	LO*	HI*-LO*
1	3630	3470	160
2	3400	3110	290
3	3210	2840	370
4	2980	2590	390
5	2830	2390	440
6	2660	2200	460
7	2500	2020	480
8	2350	1860	490
9	2220	1720	500
10	2090	1580	510
11	1800	1340	460
12	1570	1150	420
13	1390	986	404
14	1240	840	400
15	1110	735	375
16	983	631	352
17	913	560	353
18	812	486	326
19	715	442	273
20	633	378	255
21	570	347	223
22	421	248	173
23	316	187	129
24	239	139	100
25	176	105	71
26	138	75	63
27	109	57	52
28	84	48	36
29	60	35	25
30	45	27	18

* Grey levels (12-bit)

Table A-2 Transmitted HI and LO energy data for the aluminium stepwedge.

Steps	HI*	LO*	HI*-LO*
1	3810	3560	250
2	3670	3300	370
3	3650	3240	410
4	3460	3010	450
5	3360	2810	550
6	3290	2800	490
7	3190	2640	550
8	3100	2450	650
9	3060	2480	580
10	2960	2320	640
11	2900	2140	760
12	2840	2210	630
13	2740	2100	640
14	2670	1910	760
15	2630	1980	650
16	2570	1900	670
17	2480	1700	780
18	2330	1560	770
19	2210	1400	810
20	2040	1290	750
21	1880	1160	720
22	1820	1210	610
23	1350	786	564
24	1120	536	584
25	1100	578	522
26	872	409	463
27	697	314	383
28	600	263	337
29	491	206	285
30	476	184	292
31	403	164	239
32	335	129	206
33	229	93	136
34	129	55	74
35	78	33	45
36	51	24	27
37	30	18	12
38	27	15	12
39	21	11	10
40	20	11	9
41	18	13	5
42	18	9	9
43	17	8	9
44	14	10	4
45	6	5	1

* Grey levels (12-bit)

Table A-3 Transmitted HI and LO energy data for the steel stepwedge.

APPENDIX B

Computational results for the materials discrimination curves
(together with a CD containing the full range of data collected – 4095 numerical results)

X	Y: Plastic Curve	Y: Aluminium Curve	Y: Steel Curve	Y: Curve A	Y: Curve B
0	6.00197	-6.36739	-9.81615	-8.09177	-0.18271
1	6.20947	-5.88826	-9.12934	-7.50880	0.16061
2	6.41686	-5.40936	-8.44285	-6.92610	0.50375
3	6.62416	-4.93069	-7.75667	-6.34368	0.84674
4	6.83136	-4.45225	-7.07081	-5.76153	1.18955
5	7.03846	-3.97405	-6.38527	-5.17966	1.53221
6	7.24547	-3.49608	-5.70005	-4.59806	1.87470
7	7.45237	-3.01834	-5.01514	-4.01674	2.21702
8	7.65918	-2.54083	-4.33055	-3.43569	2.55918
9	7.86590	-2.06355	-3.64628	-2.85491	2.90117
10	8.07251	-1.58650	-2.96232	-2.27441	3.24300
11	8.27902	-1.10969	-2.27868	-1.69419	3.58467
12	8.48544	-0.63310	-1.59536	-1.11423	3.92617
13	8.69176	-0.15675	-0.91236	-0.53455	4.26750
14	8.89798	0.31937	-0.22967	0.04485	4.60867
15	9.10411	0.79525	0.45270	0.62398	4.94968
16	9.31013	1.27091	1.13476	1.20283	5.29052
17	9.51606	1.74634	1.81650	1.78142	5.63120
18	9.72189	2.22153	2.49792	2.35972	5.97171
19	9.92763	2.69649	3.17902	2.93776	6.31206
20	10.13326	3.17122	3.85981	3.51551	6.65224
21	10.33880	3.64572	4.54028	4.09300	6.99226
22	10.54424	4.11999	5.22043	4.67021	7.33211
23	10.74958	4.59402	5.90026	5.24714	7.67180
24	10.95482	5.06783	6.57978	5.82380	8.01133
25	11.15997	5.54140	7.25898	6.40019	8.35068
26	11.36502	6.01474	7.93787	6.97630	8.68988
27	11.56997	6.48785	8.61644	7.55214	9.02891
28	11.77482	6.96073	9.29469	8.12771	9.36777
29	11.97958	7.43337	9.97262	8.70300	9.70647
30	12.18423	7.90579	10.65024	9.27801	10.04501

Table B-1 A sample of the computational results for the materials discrimination curves (i.e. first 31 from a total of 4095).

The computational results for the materials discrimination curves is stored on the compact disc.

APPENDIX C

Grey level noise data

Grey level noise data

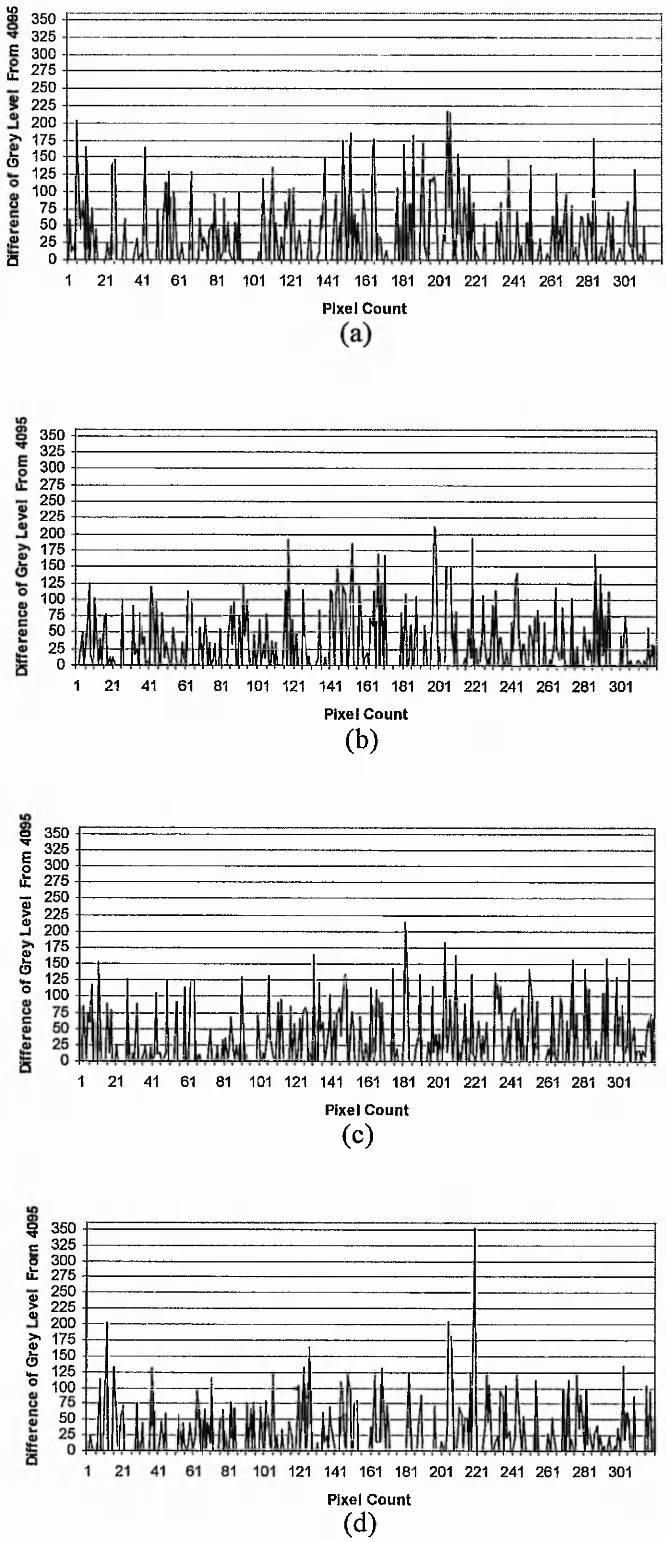

Fig. C-1 Graph of the noise analysis for the high energy data for the left perspective imaging channel: pixel column (a) 2, (b) 3, (c) 4 and (d) 5.

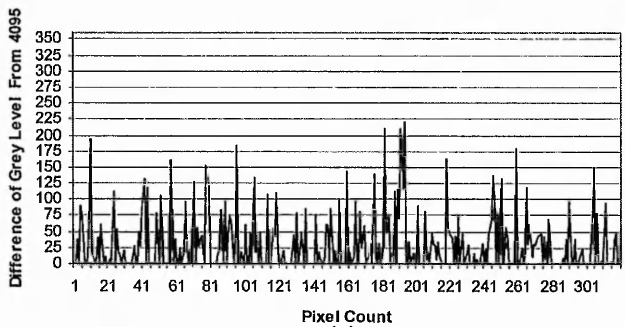

(a)

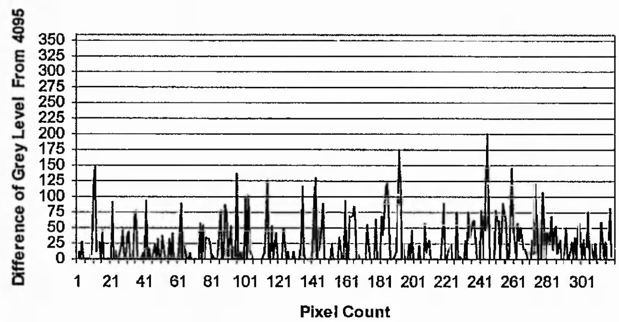

(b)

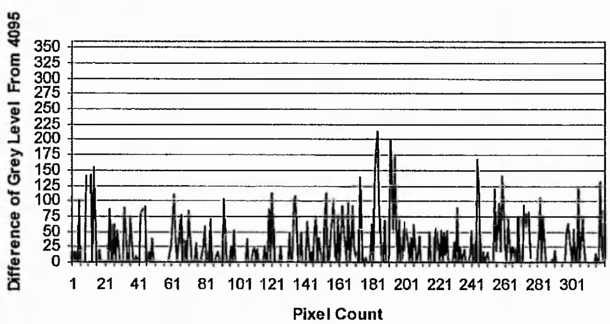

(c)

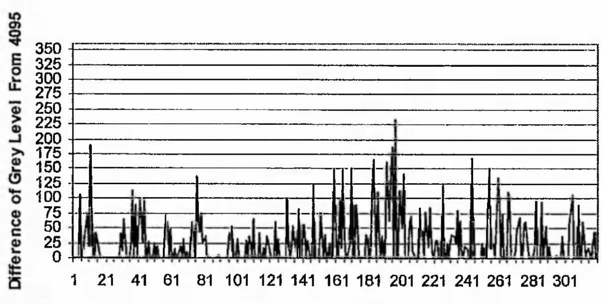

(d)

Fig. C-2 Graph of the noise analysis for the low energy data for the left perspective imaging channel: pixel column (a) 2, (b) 3, (c) 4 and (d) 5.

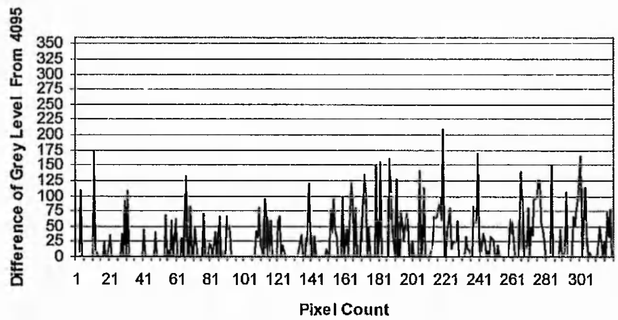

(a)

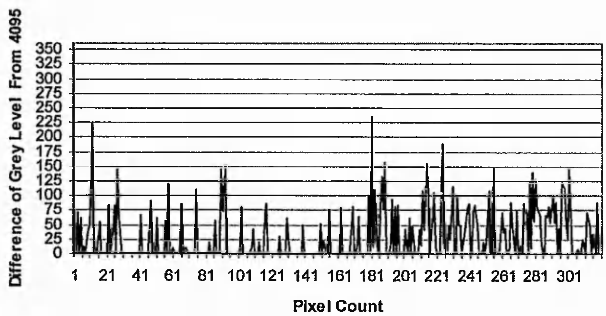

(b)

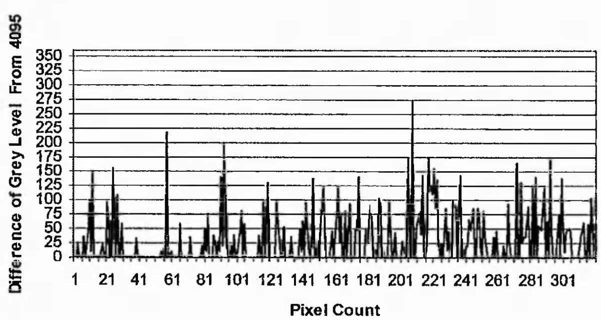

(c)

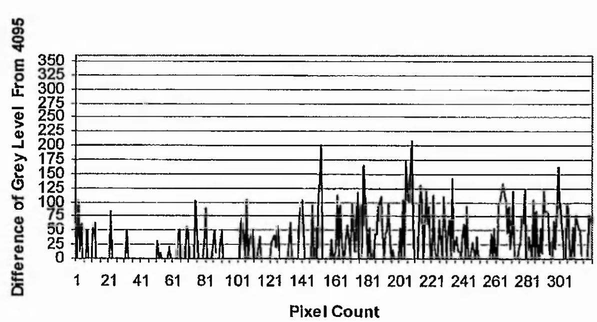

(d)

Fig. C-3 Graph of the noise analysis for the high energy data for the right perspective imaging channel: pixel column (a) 2, (b) 3, (c) 4 and (d) 5.

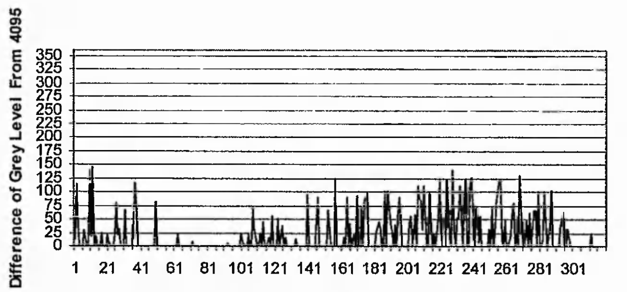

(a)

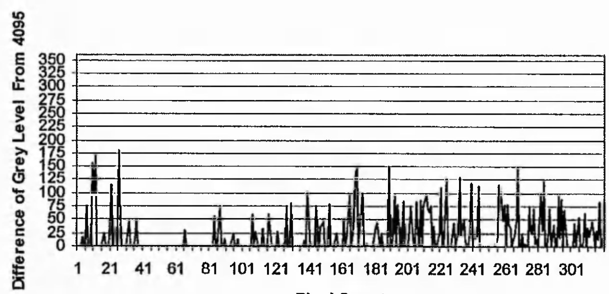

(b)

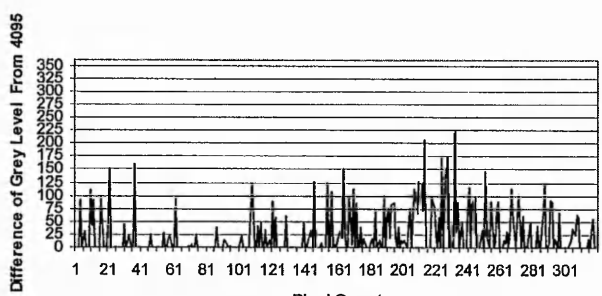

(c)

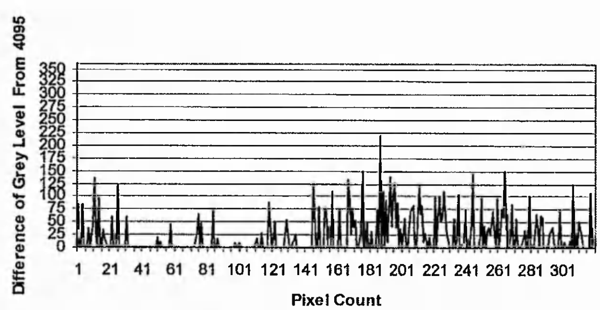

(d)

Fig. C-4 Graph of the noise analysis for the low energy data for the right perspective imaging channel: pixel column (a) 2, (b) 3, (c) 4 and (d) 5.

APPENDIX D

Automated image categorisation results

```
rawdata.dat - Notepad
File  Edit  Search  Help
=====================
Overlapping Regions:
=====================
1 overlap with 66, 2 overlap with 4, 3 overlap with 40, 4 overlap with 6,
4 overlap with 58, 5 overlap with 44, 6 overlap with 58, 7 overlap with 54,
7 overlap with 55, 7 overlap with 57, 7 overlap with 64, 7 overlap with 65,
7 overlap with 75, 8 overlap with 68, 9 overlap with 57, 10 overlap with 57,
12 overlap with 66, 12 overlap with 69, 14 overlap with 44, 21 overlap with 48,
24 overlap with 58, 25 overlap with 48, 39 overlap with 48, 40 overlap with 57,
42 overlap with 67, 44 overlap with 62, 44 overlap with 66, 44 overlap with 69,
44 overlap with 70, 44 overlap with 72, 45 overlap with 57, 45 overlap with 66,
45 overlap with 69, 45 overlap with 72, 45 overlap with 75, 48 overlap with 60,
48 overlap with 61, 48 overlap with 66, 49 overlap with 58, 50 overlap with 58,
50 overlap with 63, 50 overlap with 64, 51 overlap with 57, 52 overlap with 57,
53 overlap with 65, 54 overlap with 65, 55 overlap with 76, 57 overlap with 66,
57 overlap with 67, 57 overlap with 71, 57 overlap with 75, 58 overlap with 67,
58 overlap with 68, 58 overlap with 71, 58 overlap with 74, 59 overlap with 66,
60 overlap with 66, 61 overlap with 66, 63 overlap with 74, 64 overlap with 71,
64 overlap with 74, 65 overlap with 70

===============================
Raw Data for Region x=[LO,HI]:
===============================
Region 1=[39,74], Region 2=[23,50], Region 3=[28,57], Region 4=[51,87],
Region 5=[49,73], Region 6=[58,89], Region 7=[64,104], Region 8=[85,113],
Region 9=[85,114], Region 10=[77,103], Region 11=[75,86], Region 12=[80,125],
Region 13=[80,91], Region 14=[77,115], Region 15=[74,85], Region 16=[83,94],
Region 17=[72,81], Region 18=[92,102], Region 19=[92,101], Region 20=[98,106],
Region 21=[104,140], Region 22=[93,103], Region 23=[92,102],
Region 24=[117,155], Region 25=[114,137], Region 26=[124,152],
Region 27=[126,160], Region 28=[126,152], Region 29=[126,147],
Region 30=[125,152], Region 31=[129,156], Region 32=[130,158],
Region 33=[141,164], Region 34=[143,160], Region 35=[144,161],
Region 36=[146,164], Region 37=[147,162], Region 38=[146,163],
Region 39=[145,156], Region 40=[147,179], Region 41=[154,164],
Region 42=[156,167], Region 43=[155,169], Region 44=[167,195],
Region 45=[161,184], Region 46=[165,176], Region 47=[159,168],
Region 48=[184,193], Region 49=[197,209], Region 50=[193,204],
Region 51=[194,203], Region 52=[192,200], Region 53=[198,201],
Region 54=[197,202], Region 55=[190,197], Region 56=[190,190],
Region 57=[211,217], Region 58=[206,214], Region 59=[221,228],
Region 60=[209,224], Region 61=[209,222], Region 62=[219,205],
Region 63=[210,224], Region 64=[212,223], Region 65=[214,217],
Region 66=[230,232], Region 67=[231,233], Region 68=[229,232],
Region 69=[229,229], Region 70=[227,229], Region 71=[227,229],
Region 72=[228,232], Region 73=[247,247], Region 74=[225,227],
Region 75=[227,228], Region 76=[224,231]
```

Fig. D-1 Automated image categorisation results for baggage sample-6.

rawdata.dat - Notepad

File Edit Search Help

```
====================
Overlapping Regions:
====================
2 overlap with 6, 2 overlap with 8, 2 overlap with 9, 2 overlap with 10,
2 overlap with 11, 2 overlap with 12, 2 overlap with 21, 3 overlap with 13,
4 overlap with 69, 5 overlap with 19, 7 overlap with 73, 13 overlap with 73,
15 overlap with 68, 15 overlap with 71, 15 overlap with 73, 16 overlap with
69, 17 overlap with 68, 18 overlap with 70, 20 overlap with 69, 21 overlap
with 23, 21 overlap with 24, 22 overlap with 73, 27 overlap with 67,
27 overlap with 68, 28 overlap with 67, 28 overlap with 68, 30 overlap with
41, 33 overlap with 68, 34 overlap with 43, 35 overlap with 63, 38 overlap
with 44, 38 overlap with 47, 38 overlap with 50, 40 overlap with 49,
40 overlap with 50, 42 overlap with 68, 42 overlap with 73, 44 overlap with
47, 44 overlap with 48, 44 overlap with 51, 44 overlap with 64, 46 overlap
with 50, 46 overlap with 55, 47 overlap with 65, 49 overlap with 64,
50 overlap with 64, 50 overlap with 65, 51 overlap with 55, 51 overlap with
63, 51 overlap with 64, 51 overlap with 65, 52 overlap with 72, 53 overlap
with 62, 54 overlap with 61, 55 overlap with 64, 55 overlap with 65,
59 overlap with 69, 60 overlap with 68, 60 overlap with 81, 61 overlap with
69, 64 overlap with 72, 64 overlap with 73, 66 overlap with 73, 66 overlap
with 74, 67 overlap with 73, 68 overlap with 73, 68 overlap with 78,
68 overlap with 79, 69 overlap with 73, 69 overlap with 76, 69 overlap with
77, 69 overlap with 80, 70 overlap with 73, 71 overlap with 73, 71 overlap
with 80,

==============================
Raw Data for Region x=[LO,HI]:
==============================
Region 1=[4,9], Region 2=[8,21], Region 3=[12,28], Region 4=[7,17],
Region 5=[8,19], Region 6=[20,39], Region 7=[13,30], Region 8=[28,52],
Region 9=[28,51], Region 10=[35,61], Region 11=[35,62], Region 12=[28,51],
Region 13=[31,57], Region 14=[27,51], Region 15=[30,60], Region 16=[33,63],
Region 17=[21,43], Region 18=[32,62], Region 19=[20,43], Region 20=[20,41],
Region 21=[49,72], Region 22=[49,89], Region 23=[67,98], Region 24=[64,90],
Region 25=[67,101], Region 26=[76,120], Region 27=[64,102],
Region 28=[65,102], Region 29=[89,99], Region 30=[90,120],
Region 31=[88,121], Region 32=[83,92], Region 33=[90,127], Region 34=[90,121],
Region 35=[100,122], Region 36=[110,87], Region 37=[100,110],
Region 38=[101,122], Region 39=[111,121], Region 40=[107,133],
Region 41=[109,143], Region 42=[101,135], Region 43=[102,143],
Region 44=[132,156], Region 45=[130,160], Region 46=[131,143],
Region 47=[135,157], Region 48=[137,159], Region 49=[139,169],
Region 50=[149,161], Region 51=[163,167], Region 52=[161,172],
Region 53=[150,156], Region 54=[158,165], Region 55=[176,185],
Region 56=[181,192], Region 57=[190,199], Region 58=[182,187],
Region 59=[191,195], Region 60=[184,191], Region 61=[179,184],
Region 62=[184,187], Region 63=[200,195], Region 64=[199,208],
Region 65=[201,209], Region 66=[207,212], Region 67=[207,210],
Region 68=[211,214], Region 69=[210,214], Region 70=[207,211],
Region 71=[214,217], Region 72=[223,226], Region 73=[223,220],
Region 74=[222,225], Region 75=[221,224], Region 76=[221,223],
Region 77=[222,225], Region 78=[219,221], Region 79=[218,219],
Region 80=[221,223], Region 81=[220,223]
```

Fig. D-2 Automated image categorisation results for baggage sample-7.

rawdata.dat - Notepad

File Edit Search Help

```
====================
Overlapping Regions:
====================
1 overlap with 7, 1 overlap with 10, 1 overlap with 11, 1 overlap with 12, 1 overlap with 14, 1
overlap with 16, 1 overlap with 24, 1 overlap with 25, 1 overlap with 26, 1 overlap with 29, 1 overlap
with 30, 2 overlap with 7, 3 overlap with 22, 8 overlap with 62, 8 overlap with 104, 9 overlap with
21, 10 overlap with 22, 11 overlap with 24, 13 overlap with 25, 15 overlap with 56, 17 overlap with
27, 18 overlap with 129, 18 overlap with 143, 18 overlap with 148, 20 overlap with 36, 23 overlap with
33, 23 overlap with 36, 27 overlap with 110, 28 overlap with 56, 30 overlap with 111, 34 overlap with
54, 35 overlap with 40, 37 overlap with 51, 37 overlap with 64, 38 overlap with 56, 45 overlap with
148, 47 overlap with 102, 48 overlap with 62, 48 overlap with 63, 48 overlap with 65, 48 overlap with
66, 49 overlap with 62, 50 overlap with 62, 51 overlap with 108, 51 overlap with 129, 52 overlap with
62, 53 overlap with 62, 54 overlap with 39, 54 overlap with 62, 54 overlap with 67, 54 overlap with
69, 54 overlap with 70, 54 overlap with 71, 54 overlap with 74, 54 overlap with 75, 54 overlap with
76, 55 overlap with 64, 58 overlap with 122, 61 overlap with 101, 62 overlap with 81, 62 overlap with
82, 62 overlap with 83, 62 overlap with 84, 62 overlap with 85, 62 overlap with 86, 62 overlap with
87, 62 overlap with 103, 64 overlap with 109, 64 overlap with 110, 64 overlap with 129, 66 overlap
with 87, 66 overlap with 88, 68 overlap with 87, 70 overlap with 86, 73 overlap with 90, 74 overlap
with 89, 74 overlap with 91, 75 overlap with 92, 76 overlap with 91, 77 overlap with 91, 77 overlap
with 107, 78 overlap with 92, 78 overlap with 97, 79 overlap with 94, 79 overlap with 95, 80 overlap
with 98, 80 overlap with 118, 81 overlap with 104, 82 overlap with 104, 83 overlap with 104, 83
overlap with 105, 84 overlap with 105, 84 overlap with 107, 84 overlap with 129, 86 overlap with 107,
89 overlap with 107, 90 overlap with 112, 91 overlap with 107, 91 overlap with 115, 92 overlap with
111, 92 overlap with 116, 93 overlap with 111, 94 overlap with 113, 95 overlap with 107, 95 overlap
with 113, 95 overlap with 117, 95 overlap with 119, 96 overlap with 111, 97 overlap with 111, 98
overlap with 113, 100 overlap with 118, 101 overlap with 125, 101 overlap with 128, 101 overlap with
143, 102 overlap with 126, 102 overlap with 145, 103 overlap with 126, 103 overlap with 128, 104
overlap with 128, 105 overlap with 128, 105 overlap with 129, 106 overlap with 129, 107 overlap with
129, 107 overlap with 135, 108 overlap with 129, 109 overlap with 129, 110 overlap with 129, 110
overlap with 132, 111 overlap with 134, 111 overlap with 135, 111 overlap with 136, 113 overlap with
129, 113 overlap with 137, 113 overlap with 154, 113 overlap with 158, 114 overlap with 129, 114
overlap with 133, 117 overlap with 129, 118 overlap with 129, 118 overlap with 133, 118 overlap with
157, 120 overlap with 135, 120 overlap with 155, 121 overlap with 138, 122 overlap with 143, 123
overlap with 143, 124 overlap with 143, 124 overlap with 144, 125 overlap with 143, 126 overlap with
146, 127 overlap with 143, 128 overlap with 143, 129 overlap with 143, 129 overlap with 147, 129
overlap with 148, 129 overlap with 149, 130 overlap with 143, 131 overlap with 143, 133 overlap with
150, 133 overlap with 151, 133 overlap with 153, 133 overlap with 157, 134 overlap with 152, 136
overlap with 152, 137 overlap with 154, 139 overlap with 156, 140 overlap with 156, 142 overlap with
152,
```

rawdata.dat - Notepad

File Edit Search Help

```
===============================
Raw Data For Region x=[LO,HI]:
===============================
Region 1=[15,33], Region 2=[16,34], Region 3=[21,46], Region 4=[17,35], Region 5=[12,26],
Region 6=[20,39], Region 7=[38,66], Region 8=[31,61], Region 9=[35,65], Region 10=[32,61],
Region 11=[30,56], Region 12=[34,64], Region 13=[35,66], Region 14=[33,60], Region 15=[30,56],
Region 16=[37,66], Region 17=[33,62], Region 18=[42,75], Region 19=[45,75], Region 20=[36,65],
Region 21=[49,85], Region 22=[45,79], Region 23=[44,73], Region 24=[45,76], Region 25=[47,80],
Region 26=[48,81], Region 27=[48,85], Region 28=[35,62], Region 29=[49,83], Region 30=[50,86],
Region 31=[42,76], Region 32=[79,113], Region 33=[82,122], Region 34=[80,105], Region 35=[77,87],
Region 36=[99,108], Region 37=[95,116], Region 38=[93,102], Region 39=[87,96], Region 40=[90,103],
Region 41=[119,28], Region 42=[121,73], Region 43=[126,149], Region 44=[133,157],
Region 45=[117,126], Region 46=[112,120], Region 47=[112,118], Region 48=[127,141],
Region 49=[131,144], Region 50=[133,143], Region 51=[127,151], Region 52=[133,145],
Region 53=[133,145], Region 54=[81,113], Region 55=[135,148], Region 56=[132,145],
Region 57=[127,135], Region 58=[138,109], Region 59=[138,139], Region 60=[143,151],
Region 61=[143,146], Region 62=[144,156], Region 63=[150,163], Region 64=[146,157],
Region 65=[145,155], Region 66=[148,159], Region 67=[140,152], Region 68=[147,159],
Region 69=[142,154], Region 70=[143,154], Region 71=[147,158], Region 72=[149,161],
Region 73=[149,160], Region 74=[148,160], Region 75=[145,156], Region 76=[152,164],
Region 77=[145,156], Region 78=[131,146], Region 79=[144,154], Region 80=[135,142],
Region 81=[158,168], Region 82=[163,175], Region 83=[166,177], Region 84=[163,173],
Region 85=[164,173], Region 86=[164,174], Region 87=[162,172], Region 88=[166,176],
Region 89=[167,175], Region 90=[162,172], Region 91=[164,174], Region 92=[165,175],
Region 93=[162,172], Region 94=[164,174], Region 95=[164,173], Region 96=[165,174],
Region 97=[161,172], Region 98=[161,167], Region 99=[166,176], Region 100=[157,163],
Region 101=[186,193], Region 102=[185,192], Region 103=[182,190], Region 104=[181,189],
Region 105=[183,191], Region 106=[188,195], Region 107=[182,190], Region 108=[190,197],
Region 109=[184,192], Region 110=[186,193], Region 111=[183,191], Region 112=[182,190],
Region 113=[184,189], Region 114=[186,194], Region 115=[182,188], Region 116=[176,185],
Region 117=[183,188], Region 118=[184,192], Region 119=[178,188], Region 120=[182,190],
Region 121=[180,182], Region 122=[205,182], Region 123=[203,210], Region 124=[203,208],
Region 125=[199,204], Region 126=[203,207], Region 127=[206,211], Region 128=[208,211],
Region 129=[201,207], Region 130=[205,210], Region 131=[206,214], Region 132=[197,203],
Region 133=[202,207], Region 134=[200,206], Region 135=[200,205], Region 136=[203,209],
Region 137=[203,208], Region 138=[203,209], Region 139=[199,202], Region 140=[202,205],
Region 141=[205,205], Region 142=[202,198], Region 143=[215,210], Region 144=[219,221],
Region 145=[220,222], Region 146=[216,218], Region 147=[212,215], Region 148=[222,225],
Region 149=[211,215], Region 150=[213,216], Region 151=[215,217], Region 152=[215,217],
Region 153=[214,215], Region 154=[214,217], Region 155=[219,218], Region 156=[215,215],
Region 157=[213,214], Region 158=[222,224]
```

Fig. D-3 Automated image categorisation results for baggage sample-8.

rawdata.dat - Notepad

File Edit Search Help

```
=====================
Overlapping Regions:
=====================
1 overlap with 55, 2 overlap with 53, 3 overlap with 53, 4 overlap with 55,
5 overlap with 55, 6 overlap with 51, 6 overlap with 55, 7 overlap with 26,
7 overlap with 31, 8 overlap with 53, 10 overlap with 53, 11 overlap with 53,
19 overlap with 53, 20 overlap with 53, 21 overlap with 53, 26 overlap with
38, 29 overlap with 32, 29 overlap with 35, 30 overlap with 31, 31 overlap
with 32, 31 overlap with 38, 32 overlap with 53, 32 overlap with 55,
35 overlap with 44, 35 overlap with 53, 35 overlap with 54, 36 overlap with
38, 37 overlap with 50, 38 overlap with 45, 38 overlap with 48, 38 overlap
with 49, 38 overlap with 50, 38 overlap with 55, 38 overlap with 57,
39 overlap with 48, 40 overlap with 52, 41 overlap with 48, 42 overlap with
48, 43 overlap with 50, 43 overlap with 59, 45 overlap with 53, 46 overlap
with 53, 47 overlap with 53, 48 overlap with 56, 48 overlap with 57,
49 overlap with 55, 50 overlap with 55, 51 overlap with 55, 51 overlap with
58, 52 overlap with 55, 52 overlap with 58,

===============================
Raw Data for Region x=[LO,HI]:
===============================
Region 1=[31,64], Region 2=[42,75], Region 3=[42,76], Region 4=[44,81],
Region 5=[60,103], Region 6=[58,95], Region 7=[91,112], Region 8=[101,96],
Region 9=[105,70], Region 10=[101,119], Region 11=[101,119], Region
12=[103,122], Region 13=[107,122], Region 14=[100,110], Region 15=[104,114],
Region 16=[102,112], Region 17=[99,108], Region 18=[98,105], Region
19=[115,108], Region 20=[114,110], Region 21=[117,115], Region 22=[117,117],
Region 23=[121,129], Region 24=[121,129], Region 25=[110,117], Region
26=[121,145], Region 27=[112,120], Region 28=[112,120], Region 29=[134,146],
Region 30=[137,149], Region 31=[143,153], Region 32=[163,172], Region
33=[150,156], Region 34=[161,168], Region 35=[180,188], Region 36=[184,192],
Region 37=[181,187], Region 38=[192,199], Region 39=[190,196], Region
40=[192,199], Region 41=[194,196], Region 42=[190,194], Region 43=[186,191],
Region 44=[216,221], Region 45=[208,212], Region 46=[212,216], Region
47=[214,220], Region 48=[210,214], Region 49=[212,217], Region 50=[209,212],
Region 51=[215,219], Region 52=[211,214], Region 53=[222,210], Region
54=[223,225], Region 55=[223,225], Region 56=[221,224], Region 57=[222,224],
Region 58=[219,223], Region 59=[221,223]
```

Fig. D-4 Automated image categorisation results for baggage sample-9.

APPENDIX E

Software listing for the automated target material detection program

```
/*************************************************************************************
Date:    17th August 2002
Author:  Ta Wee Wang
Title:   Automated Target Material Detection Program

Utilised standard imaging tools:
=======================
Matrox Imaging Library (MIL 4.0)
COPYRIGHT (c) Matrox Electronic Systems Ltd.

Description:
=========
Initially, the program will acquire the input low energy and the high energy x-ray images, and store them into image buffers for further processing. These images will be first filtered by utilising a median filter.

The low energy image will be then delineated into individual segmented regions by employing the wavelet transform technique. The high and the low energy data (i.e. average grey levels) for every successfully segmented region are computed from the filtered high and the low energy image. The dual-energy data is then stored in a database for further analysis.

Then, the program will determine the neighbouring regions that are connected to each segmented region in an x-ray image. Each segmented region (n) will be examined in comparison to all other segmented regions (m). If region n has a neighbouring region m, where region n's average grey level is less than the average grey level for the region m, it is defined that region n is overlapping region m. All the results are stored in a database for further quantitative analysis (i.e. to extract the characteristic angle for overlapping objects).

The characteristic angle for each overlapping object is calculated by using the formulae derived in the thesis. The program will display the discriminated target material in red, provided that the calculated characteristic angle lies within the predefined window (i.e. 87.0<ϑ<92.0, for a plastic target).
*************************************************************************************/


#include <stdio.h>
#include <stdlib.h>
#include <mil.h>
#include <math.h>
#include "AMR.h"


//+++++++++++++++++++++++++++++++++++++++++++++++++++++++++++++++++++++++++++++++++++//
FILE            *savedata;      //Database stored in local C drive.
struct temp                     //Database stored in local C drive.
{char tmp[50];};
struct temp raw_data[500];

#define J 5 //Maximum wavelet scale.
#define DATA_POINTS   256 //Predefined histogram having 256 data points

struct dummy //Dummy database
{char tmp[50];};
```

```
struct dummy values[500];
struct dummy1 //Dummy database for wavelet results
{float H[DATA_POINTS];
 float G[DATA_POINTS];};
struct dummy1 wc[6];

//Setup the path in "milsetup.h".
#define  IMAGE_FILE     M_IMAGE_PATH"1ll.tif"  //Input low energy image.
#define  IMAGE_FILE2    M_IMAGE_PATH"1lh.tif"  //Input high energy image.
#define  IMAGE_WIDTH  1024L                    //Image X-Axis size.
#define  IMAGE_HEIGHT 320L                     //Image Y-Axis size.
#define  RAWDATA        "C:\\Automated Material Recognition\\Analysis Database\\rawdata.dat"
                                               //File location for database.

//Predefined target material's characteristic angle window. For plastic plate detection, the window is
//defined as:
#define  Target_Window1  87.9  //Minimum characteristic angle.
#define  Target_Window2  91.6  //Maximum characteristic angle.


double   Mean_GL[2][500L],T[2][500L],  //Grey level database for all materials.
         Overlap[2][500L][500L];       //Overlapping materials' database
//Initialisation definitions for MATROX IMAGING LIBRARY, where
//L=Low energy image
//H=High energy image

MIL_ID MilApplication,   // Application identifier
         MilSystem,        // System identifier
         MilDisplayL,      // Display identifier for Parent image
         MilDisplayH,      // Display identifier for Parent image
         MilDisplayL2,     // Display identifier for Parent image
         MilDisplayH2,     // Display identifier for Parent image
         MilOvrDisplay,    // Overlay display identifier for Source image
         MilOvrDisplay2,   // Overlay display identifier for Source image
         MilParentLoImage,    // Low energy image buffer identifier
         MilParentHiImage,    // High energy image buffer identifier
         MilSegImage,         // Segmented low energy image buffer identifier
         MilBinSubImage,      // Binary image buffer identifier
         MilBinSub2Image,     // 2nd Binary image buffer identifier
         MilSrcSubImage,      // Source image buffer identifier
         MilDstSubImage,      // Destination image buffer identifier
         MilTmpSubImage,      // Temporary image buffer identifier
         MilTmp2SubImage,     // Temporary2 image buffer identifier
         MilColorImage,       // Color image buffer identifier
         MilColor2Image,      // Color2 image buffer identifier
         MilGL_AnaLOImage, //Low energy image buffer identifier for grey level calculation
         MilGL_AnaHIImage, //High energy image buffer identifier for grey level calculation
         HistResult,          // Histogram buffer identifier
         ExtrResult,          // Extreme result buffer identifier
         BlobResultLO,        // Blob result buffer identifier
         BlobResultHI,        // Blob result buffer identifier
         FeatureList;         // Feature list identifier
//++++++++++++++++++++++++++++++++++++++++++++++++++++++++++++++++++++++++++++++++++++++++++++++//

void main(void)
{
long     ErrorCode;
int      thres[100], thres_c;

//Allocate the default system and image buffer
```

```
MappAllocDefault(M_SETUP, &MilApplication, &MilSystem,
M_NULL, M_NULL, M_NULL);

Alloc_Buffer(); //Allocate all image buffers.
MappGetError(M_CURRENT, &ErrorCode);//Check the error status code set by the allocation
                                    //command.

if (ErrorCode == M_NULL) //If no error found, start executing the Automated Target
                         //Material Detection Program.
{
Auto_Image_Seg(thres, &thres_c); //Call Automated Image Segmentation Program.
Auto_Image_Cat(thres, thres_c);    //Extract area of interest.
getchar();
Release_Buffer();                  //Release all allocated buffer.
}

else //End of code if initialisation fails.
{
printf("Error: Image buffer allocation failed.\n");
printf("Press <Enter> to end.\n");
}

// Free all allocations
MappFreeDefault(MilApplication, MilSystem, M_NULL, M_NULL, M_NULL);
printf("\nDone!!!\n");
}
//++++++++++++++++++++++++++++++++++++++++++++++++++++++++++++++++++++++++++++++//

void Alloc_Buffer()
{
// Allocate image buffers with the defined dimensions for Display and Processing purposes.
MbufAlloc2d(M_DEFAULT, IMAGE_WIDTH, IMAGE_HEIGHT,
8L+M_UNSIGNED, M_IMAGE+M_DISP+M_PROC, &MilParentLoImage);//Low energy image

MbufAlloc2d(M_DEFAULT, IMAGE_WIDTH, IMAGE_HEIGHT,
8L+M_UNSIGNED, M_IMAGE+M_DISP+M_PROC, &MilParentHiImage);//High energy image

MbufAllocColor(M_DEFAULT, 3L, IMAGE_WIDTH, IMAGE_HEIGHT,
8L+M_UNSIGNED, M_IMAGE+M_DISP, &MilSegImage);//Segmented image

MbufAlloc2d(M_DEFAULT, IMAGE_WIDTH, IMAGE_HEIGHT,
1+M_UNSIGNED, M_IMAGE+M_PROC, &MilBinSubImage);//Binary image1

MbufAlloc2d(M_DEFAULT, IMAGE_WIDTH, IMAGE_HEIGHT,
1+M_UNSIGNED, M_IMAGE+M_PROC, &MilBinSub2Image);//Binary image2

MbufAlloc2d(M_DEFAULT, IMAGE_WIDTH, IMAGE_HEIGHT,
8L+M_UNSIGNED, M_IMAGE+M_PROC, &MilSrcSubImage);//Temp image buffer1

MbufAlloc2d(M_DEFAULT, IMAGE_WIDTH, IMAGE_HEIGHT,
8L+M_UNSIGNED, M_IMAGE+M_PROC+M_DISP, &MilDstSubImage);//Temp image buffer2

MbufAlloc2d(M_DEFAULT, IMAGE_WIDTH, IMAGE_HEIGHT,
8L+M_UNSIGNED, M_IMAGE+M_DISP+M_PROC, &MilTmpSubImage);//Temp image buffer3

MbufAlloc2d(M_DEFAULT, IMAGE_WIDTH, IMAGE_HEIGHT,
8L+M_UNSIGNED, M_IMAGE+M_DISP+M_PROC, &MilTmp2SubImage);//Temp image buffer4
```

```
MbufAlloc2d(M_DEFAULT, IMAGE_WIDTH, IMAGE_HEIGHT,
8L+M_UNSIGNED, M_IMAGE+M_PROC, &MilGL_AnaLOImage);//Temp image buffer for low
                                                    //energy image

MbufAlloc2d(M_DEFAULT, IMAGE_WIDTH, IMAGE_HEIGHT,
8L+M_UNSIGNED, M_IMAGE+M_PROC, &MilGL_AnaHIImage);//Temp image buffer for High
                                                    //energy Image

MbufAllocColor(M_DEFAULT, 3L, IMAGE_WIDTH, IMAGE_HEIGHT,
8L+M_UNSIGNED, M_IMAGE+M_PROC+M_DISP, &MilColorImage);//Image buffer for colour
                                                    //image1

MbufAllocColor(M_DEFAULT, 3L, IMAGE_WIDTH, IMAGE_HEIGHT,
8L+M_UNSIGNED, M_IMAGE+M_PROC+M_DISP, &MilColor2Image);//Image buffer for colour
                                                    //image2

MdispAlloc(M_DEFAULT, M_DEV0, "M_DEFAULT", M_DEFAULT, &MilDisplayL);
                                                    //Image for display mode 1

MdispAlloc(M_DEFAULT, M_DEV1, "M_DEFAULT", M_DEFAULT, &MilDisplayL2);
                                                    //Image for display mode 2

MdispAlloc(M_DEFAULT, M_DEV2, "M_DEFAULT", M_DEFAULT, &MilDisplayH);
                                                    //Image for display mode 3

 MdispAlloc(M_DEFAULT, M_DEV3, "M_DEFAULT", M_OVR, &MilDisplayH2);
                                                    //Image for display mode 4

MdispAlloc(M_DEFAULT, M_DEV4, "M_DEFAULT", M_OVR, &MilOvrDisplay);
                                                    //Image for display mode 5

MdispAlloc(M_DEFAULT, M_DEV5, "M_DEFAULT", M_OVR, &MilOvrDisplay2);
                                                    //Image for display mode 6
}
//++++++++++++++++++++++++++++++++++++++++++++++++++++++++++++++++++++++++++++//

void Auto_Image_Seg(int thres[], int *thres_c)// Automated Image Segmentation Program.
{
long    HistVals[500L];
float   Hf[500L];
int     thres_c2;
short   i;

MbufLoad(IMAGE_FILE, MilParentLoImage);      //Load source image into an image buffer.
MimRank(MilParentLoImage,     MilParentLoImage,     M_3X3_RECT,     M_MEDIAN,
M_GRAYSCALE);                                //Perform median filtering to remove noise.

MbufCopy(MilParentLoImage, MilSrcSubImage);  // Copy data buffer to another.
MdispSelect(MilDisplayL, MilParentLoImage);  // Display the image buffer.
MgraText(M_DEFAULT, MilParentLoImage, 5, 5,"- LO IMAGE -");//Add text into image buffer.
MbufCopy(MilSrcSubImage, MilGL_AnaLOImage); // Copy data buffer to another.
getchar();

MbufLoad(IMAGE_FILE2, MilParentHiImage);     // Load source image into an image buffer.
MimRank(MilParentHiImage, MilParentHiImage, M_3X3_RECT, M_MEDIAN, M_GRAYSCALE);
                                             //Perform median filtering to remove noise.
MdispSelect(MilDisplayH, MilParentHiImage);  // Display the image buffer.
MgraText(M_DEFAULT, MilParentHiImage, 5, 5,"- HI IMAGE -");//Add text into image buffer.
MbufCopy(MilParentHiImage, MilGL_AnaHIImage);     // Copy data buffer to another buffer.
getchar();
```

```
MimAllocResult(M_DEFAULT, 256, M_HIST_LIST, &HistResult); //Allocate a histogram buffer
MimHistogram(MilSrcSubImage, HistResult);                   // Perform the histogram
MimGetResult(HistResult, M_VALUE, HistVals);                // Get the results

for(i=0; i<256; i++) //Float cast the histogram value for wavelet analysis.
Hf[i]=(float)HistVals[i];

GetThresholdData(Hf, 2, thres, &thres_c2);//Get wavelet results.
*thres_c=thres_c2;        //Point to the wavelet result.
MimFree(HistResult);
}
//++++++++++++++++++++++++++++++++++++++++++++++++++++++++++++++++++++++++++++++//

void Auto_Image_Cat(int thres[], int thres_c)//Automated Image Categorisation Program.
{
int      colour=1L, multip=1L, upflag=1L, count, w, x, y, z;
long     MaxLabelNumber, HistVals[500L];
double   Mean_Tmp[1], al, pl, al_tmp, pl_tmp, result;
z=0;  // Initialised with 0 for the analysis of low energy segmented regions.

MbufClear(MilDstSubImage, 0L);                 // Clear buffer
MbufClear(MilColor2Image, 0L);                 // Clear buffer

//Allocate a histogram buffer
MimAllocResult(M_DEFAULT, 1L, M_EXTREME_LIST, &ExtrResult);
MimAllocResult(M_DEFAULT, 256L, M_HIST_LIST, &HistResult);
//Allocate buffer for high energy and low energy data (i.e. grey level)
MblobAllocFeatureList(M_DEFAULT, &FeatureList);
MblobSelectFeature(FeatureList, M_MEAN_PIXEL);
MblobAllocResult(M_DEFAULT, &BlobResultLO);
MblobAllocFeatureList(M_DEFAULT, &FeatureList);
MblobSelectFeature(FeatureList, M_MEAN_PIXEL);
MblobAllocResult(M_DEFAULT, &BlobResultHI);

for (w=0; w<thres_c-1; w++)  //Extract all segmented regions.
{
//Binarise the image buffer for further processing.
MimBinarize(MilSrcSubImage, MilBinSubImage, M_IN_RANGE, thres[w], thres[w+1]);

        if (multip > 1)
        {
        //Extract area of interest.
        MimBinarize(MilDstSubImage, MilBinSub2Image, M_IN_RANGE, 1, multip-1);
        MbufCopy(MilBinSub2Image, MilTmp2SubImage);//Store into temp buffer.
        MbufCopy(MilBinSubImage, MilTmpSubImage);//Store into temp buffer.

        //Logical subtract the 2 images.
        MimArith(MilTmp2SubImage, MilTmpSubImage, MilTmpSubImage, M_SUB);

        //The resultant segmented region.
        MimBinarize(MilTmpSubImage, MilBinSubImage, M_EQUAL, 255, M_NULL);
        }

        MimOpen(MilBinSubImage, MilBinSubImage, 1L, M_BINARY);//Remove noise

        //Label all materials for further processing.
        MimLabel(MilBinSubImage, MilTmpSubImage, M_4_CONNECTED+M_BINARY);

        //Get the maximum segmented regions.
        MimFindExtreme(MilTmpSubImage, ExtrResult, M_MAX_VALUE);
```

```
        MimGetResult(ExtrResult, M_VALUE, &MaxLabelNumber);  //Get the calculation result


        //Find the histogram of the image to know the size of each region.
        MimHistogram(MilTmpSubImage, HistResult);

        MimGetResult(HistResult, M_VALUE, HistVals);    //Get histogram result.

        if (MaxLabelNumber >= 0)//Maximum segmented regions found.
        {
                for (x=1; x<=MaxLabelNumber; x++)
                {
                if (HistVals[x]>30L) //30 is defined max noise level.
                {
                MimBinarize(MilTmpSubImage, MilBinSubImage, M_EQUAL, x,
                M_NULL);//First, binarise the material

                Label_Colour(colour);//Assign a colour into the area of interest.
                if (upflag==0)//Counter to colour the segmented region.
                {
                colour=colour-1;//assign the colour randomly
                        if (colour==0)
                        {
                        upflag=1;
                        colour=colour+1;//assign the color randomly
                        }
                }
                else if (upflag==1)
                {
                colour=colour+1;//assign the color randomly
                        if (colour>10)
                        {
                        upflag=0;
                        colour=colour-1;//assign the color randomly
                        }
                }

                //Further remove noise
                MimErode(MilBinSubImage, MilBinSub2Image, 1, M_BINARY);

                //Get the grey levels values for the low and the high energy segmented regions.
                MblobCalculate(MilBinSub2Image, MilGL_AnaLOImage, FeatureList,
                BlobResultLO);
                MblobGetResult(BlobResultLO, M_MEAN_PIXEL, Mean_Tmp);
                Mean_GL[0][multip]=Mean_Tmp[0]; //Results for low energy Image
                MblobCalculate(MilBinSub2Image, MilGL_AnaHIImage, FeatureList,
                BlobResultHI);
                MblobGetResult(BlobResultHI, M_MEAN_PIXEL, Mean_Tmp);
                Mean_GL[1][multip]=Mean_Tmp[0]; //Results for high energy Image
                MimArith(MilBinSubImage, multip, MilTmp2SubImage, M_MULT_CONST);
                //Store result in destination image buffer (i.e. labelled image).
                MimArith(MilTmp2SubImage,MilDstSubImage, MilDstSubImage, M_OR);
                multip++;//Counter for all extracted regions.
                }
                }
        }
}

multip=multip-1;//Counter for all extracted materials.
```

```
MbufCopy(MilColor2Image, MilSegImage);//Store into temp buffer.
MdispSelect(MilDisplayL2, MilSegImage);//Display the segmentation results.
MgraText(M_DEFAULT, MilSegImage, 5, 5,"- Segmented Image -");//Add text into image buffer.
//Save image into local drive.
MbufSave("C:\\Automated Material Recognition\\Analysis Database\\Segmented Img Color.tif",
MilColor2Image);
getchar();

MimOpen(MilDstSubImage, MilDstSubImage, 1L, M_GRAYSCALE); //Further remove noise.
for (x=1; x<=multip; x++)
{
//Binarise all materials to analyse overlapping structures.
MimBinarize(MilDstSubImage, MilBinSubImage, M_EQUAL, x, M_NULL);
MimDilate(MilBinSubImage, MilBinSubImage, 2, M_BINARY);//Expand the area by '2'.
//Multiply with the buffered image.
MimArith(MilBinSubImage, MilDstSubImage, MilTmp2SubImage, M_MULT);

MimHistogram(MilTmp2SubImage, HistResult);            //Get the histogram.
MimGetResult(HistResult, M_VALUE, HistVals);          //Get the result.
w=1;
for (y=1; y<=multip; y++)
{
        //If the condition is fulfilled, then the 2 regions are overlapped on each other.
        if ( HistVals[y]>15 && y!=x && Mean_GL[z][x]<Mean_GL[z][y])
        {
         //Store the overlapping information into database for characteristic angle calculations.
         Overlap[z][x][w]=y;
         w++;
        }
}
}


//Start storing all raw data into local drive for further analysis (i.e.characteristic angle calculations).
if ((savedata = fopen(RAWDATA, "wt" )) == NULL)
{
        printf("\nUnable to open raw data file!");
        exit(1);
}

sprintf(raw_data[x].tmp,"====================\nOverlapping
Regions:\n====================\n");

fputs(raw_data[x].tmp, savedata);//Start storing all the overlapping materials' database.
for (x=1; x<=multip; x++)
{       w=1;
        while (Overlap[z][x][w]!=0)
        {
        //Store all the overlapping materials' database.
        sprintf(raw_data[x].tmp, "%d overlap with %.0f, ", x,  Overlap[z][x][w++]);
        fputs(raw_data[x].tmp, savedata);
        }
}

sprintf(raw_data[x].tmp,  "\n\n==============================\nRaw Data for Region
x=[LO,HI]:\n==============================\n");

fputs(raw_data[x].tmp, savedata);//Start storing all the materials' grey level database.
for (x=1; x<=multip; x++)
{
```

```
        sprintf(raw_data[x].tmp, "Region %d=[%.0f,%.0f], ", x, Mean_GL[0][x], Mean_GL[1][x]);
        fputs(raw_data[x].tmp, savedata);//Store all the materials' grey level database.
}

sprintf(raw_data[x].tmp,      "\n\n==============================\nCharacteristic      Angle
Calculation:\n==============================\n");

fputs(raw_data[x].tmp, savedata);//Start storing all the Characteris Angle Calculation database.

MbufClear(MilColorImage, 0L);//Clear the buffer.
MbufClear(MilColor2Image, 0L);//Clear the buffer.
//Add text onto the image buffer.
MgraText(M_DEFAULT, MilColor2Image, 1, 1,"Material with 87.9<Angle<91.6");
for (x=1; x<=multip; x++)
{
        w=1; count=0;

        //Formulae for logarithmic transmission for background grey level, TL
        T[0][x]=(log10(253.1)/log10(2.718281828))- (log10(Mean_GL[0][x])/log10(2.718281828));
        //Formulae for logarithmic transmission for background grey level, TH
        T[1][x]=(log10(253.1)/log10(2.718281828))- (log10(Mean_GL[1][x])/log10(2.718281828));

        //Non overlapping region//
        //Formulae obtained from calibration results for plastic basis materials.
        pl=-0.6130059495-87.18457982*T[0][x]+150.0505503*T[1][x]+
        94.93020284*T[0][x]*T[1][x]-61.84689434*T[0][x]*T[0][x]- 47.19713241*T[1][x]*T[1][x]
        - 0.6950932582*T[0][x]*T[0][x]*T[1][x]*T[1][x] + 6.136233669*T[0][x]*T[0][x]*T[0][x]
        - 1.519782068*T[1][x]*T[1][x]*T[1][x];

        //Formulae obtained from calibration results for aluminium basis materials.
        al=0.2115282084+37.52390472*T[0][x]-47.65888221*T[1][x]-4.82311783*T[0][x]*T[1][x]

        +37.53039056*T[0][x]*T[0][x]+33.07199059*T[1][x]*T[1][x]+0.2592219569*T[0][x]*T[0]
        [x]*T[1][x]*T[1][x]-2.448328168*T[0][x]*T[0][x]*T[0][x]
        +0.7037951622*T[1][x]*T[1][x]*T[1][x];

        //Non overlapping region
        if (Overlap[z][x][w] == 0)
        {
                if (al != 0)
                {
                result = atan2( pl, al )*57.29577951;//Calculate the characteristic angle.
                sprintf(raw_data[x].tmp, "Region %d=%.5f, ", x, result);//Save into the database.
                fputs(raw_data[x].tmp, savedata);//Save into the database.
                }
                else if (al == 0)//To avoid calculation overflow error.
                {
                result = 90.0;//If the characteristic angle is exactly 90 degree.
                sprintf(raw_data[x].tmp, "Region %d=%.5f, ", x, result);//Save into the database.
                fputs(raw_data[x].tmp, savedata);//Save into the database.
                }

                //Target materials windows for characteristic angle.
                if (result>Target_Window1 && result<Target_Window2)
                {
                //For display purposes
                MimBinarize(MilDstSubImage, MilBinSubImage, M_EQUAL, x, M_NULL);
                Label_Colour(5);//Label the target object in red colour.
                }
        }
```

```
//For overlapping materials, the calculation of characteristic angle will require the Basis
//Materials Subtraction techniques.
else if (Overlap[z][x][w] != 0)
{
//Calculate all possible characteristic angles, if that region is overlapped by many possible
//neighbouring regions by utilising the Basis Materials Subtraction techniques.
while (Overlap[z][x][w]!=0)
{
y = Overlap[z][x][w];

//Formulae for logarithmic transmission for background grey level, TL
T[0][y]=(log10(253.1)/log10(2.718281828))-(log10(Mean_GL[0][y])/log10(2.718281828));

//formulae for logarithmic transmission for background grey level, TH
T[1][y]=(log10(253.1)/log10(2.718281828))- (log10(Mean_GL[1][y])/log10(2.718281828));

//Formulae obtained from calibration results for plastic basis materials.
pl_tmp=-0.6130059495-87.18457982*T[0][y]+150.0505503*T[1][y]+
94.93020284*T[0][y]*T[1][y]-61.84689434*T[0][y]*T[0][y]- 47.19713241*T[1][y]*T[1][y]
- 0.6950932582*T[0][y]*T[0][y]*T[1][y]*T[1][y] + 6.136233669*T[0][y]*T[0][y]*T[0][y]
 - 1.519782068*T[1][y]*T[1][y]*T[1][y];

//Formulae obtained from calibration results for aluminium basis materials.
al_tmp = 0.2115282084 + 37.52390472*T[0][y] - 47.65888221*T[1][y] -
64.82311783*T[0][y]*T[1][y]+37.53039056*T[0][y]*T[0][y]+ 3.07199059*T[1][y]*T[1][y]
 + 0.2592219569*T[0][y]*T[0][y]*T[1][y]*T[1][y] - 2.448328168*T[0][y]*T[0][y]*T[0][y]
 + 0.7037951622*T[1][y]*T[1][y]*T[1][y];

//Apply the Basis Materials Subtraction techniques.
pl_tmp = pl - pl_tmp;
al_tmp = al - al_tmp;

if (al_tmp != 0)
{
result = atan2( pl_tmp, al_tmp )*57.29577951;//Calculate the characteristic angle
sprintf(raw_data[x].tmp, "Region %d=%.5f, ", x, result);//Save into the database.
fputs(raw_data[x].tmp, savedata);//Save into the database
}

else if (al_tmp == 0) //To avoid calculation overflow error.
{
result = 90.0;//If the characteristic angle is exactly 90 degree
sprintf(raw_data[x].tmp, "Region %d=%.5f, ", x, result);//Save into the database
fputs(raw_data[x].tmp, savedata);//Save into the database
}

if (count!=11)//counter is to avoid displaying the same detected area for more than once.
{
        //Target materials windows for characteristic angle.
        if (result>Target_Window1 && result<Target_Window2)
        {
        //For display purposes.
        MimBinarize(MilDstSubImage, MilBinSubImage, M_EQUAL, x, M_NULL);

        Label_Colour(5);//Label the target material in red colour.
        count=11;
        }
}

w++;
```

```
        }
        }
sprintf(raw_data[x].tmp, "\n");//Save the characteristic angle calculation results.
fputs(raw_data[x].tmp, savedata);//Save into the database.
}

MdispSelect(MilOvrDisplay, MilColor2Image);//Display the detected target materials.
MbufSave("C:\\Automated Material Recognition\\Analysis Database\\Detected Target Materials.tif",
MilColor2Image);//Save the detected target materials.

fclose(savedata);//Finished storing whole database.

//Free all previously allocated buffer before exiting.
MimFree(ExtrResult);
MimFree(HistResult);
MblobFree(BlobResultLO);
MblobFree(BlobResultHI);
MblobFree(FeatureList);
}
//+++++++++++++++++++++++++++++++++++++++++++++++++++++++++++++++++++++++++++++++//

void Label_Colour(int colour)//label each segmented region with colour.
{
switch (colour)
{
case 1  :   MimArith(MilBinSubImage, 255L, MilTmp2SubImage, M_MULT_CONST);
            MbufCopyColor(MilTmp2SubImage, MilColorImage, M_BLUE);     //Blue
            break;
case 2  :   MimArith(MilBinSubImage, 255L, MilTmp2SubImage, M_MULT_CONST);
            MbufCopyColor(MilTmp2SubImage, MilColorImage, M_BLUE);     //Cyan
            MbufCopyColor(MilTmp2SubImage, MilColorImage, M_GREEN);
            break;
case 3  :   MimArith(MilBinSubImage, 255L, MilTmp2SubImage, M_MULT_CONST);
            MbufCopyColor(MilTmp2SubImage, MilColorImage, M_GREEN);    //Green
            break;
case 4  :   MimArith(MilBinSubImage, 255L, MilTmp2SubImage, M_MULT_CONST);
            MbufCopyColor(MilTmp2SubImage, MilColorImage, M_GREEN);    //Yellow
            MbufCopyColor(MilTmp2SubImage, MilColorImage, M_RED);
            break;
case 5  :   MimArith(MilBinSubImage, 255L, MilTmp2SubImage, M_MULT_CONST);
            MbufCopyColor(MilTmp2SubImage, MilColorImage, M_RED);      //Red
            break;
case 6  :   MimArith(MilBinSubImage, 255L, MilTmp2SubImage, M_MULT_CONST);
            MbufCopyColor(MilTmp2SubImage, MilColorImage, M_RED);      //Magenta
            MbufCopyColor(MilTmp2SubImage, MilColorImage, M_BLUE);
            break;
case 7  :   MimArith(MilBinSubImage, 153L, MilTmp2SubImage,
            M_MULT_CONST);//Purple
            MbufCopyColor(MilTmp2SubImage, MilColorImage, M_RED);
            MimArith(MilBinSubImage, 204L, MilTmp2SubImage, M_MULT_CONST);
            MbufCopyColor(MilTmp2SubImage, MilColorImage, M_BLUE);
            break;
case 8  :   MimArith(MilBinSubImage, 123L, MilTmp2SubImage,
            M_MULT_CONST);//Brown
            MbufCopyColor(MilTmp2SubImage, MilColorImage, M_RED);
            MimArith(MilBinSubImage, 63L, MilTmp2SubImage, M_MULT_CONST);
            MbufCopyColor(MilTmp2SubImage, MilColorImage, M_GREEN);
            MbufCopyColor(MilTmp2SubImage, MilColorImage, M_BLUE);
            break;
```

```
case 9  :       MimArith(MilBinSubImage, 255L, MilTmp2SubImage, M_MULT_CONST);
                MbufCopyColor(MilTmp2SubImage, MilColorImage, M_RED);       //Pink
                MimArith(MilBinSubImage, 153L, MilTmp2SubImage, M_MULT_CONST);
                MbufCopyColor(MilTmp2SubImage, MilColorImage, M_GREEN);
                MimArith(MilBinSubImage, 204L, MilTmp2SubImage, M_MULT_CONST);
                MbufCopyColor(MilTmp2SubImage, MilColorImage, M_BLUE);
                break;
case 10  :      MimArith(MilBinSubImage, 255L, MilTmp2SubImage, M_MULT_CONST);
                MbufCopyColor(MilTmp2SubImage, MilColorImage, M_RED);       //Orange
                MimArith(MilBinSubImage, 102L, MilTmp2SubImage, M_MULT_CONST);
                MbufCopyColor(MilTmp2SubImage, MilColorImage, M_GREEN);
                break;
default  :      break;
}
//Store the result into this colour image buffer.
MimArith(MilColorImage,MilColor2Image, MilColor2Image, M_OR);
MdispSelect(MilOvrDisplay, MilColor2Image);//Display on to screen.
}
//+++++++++++++++++++++++++++++++++++++++++++++++++++++++++++++++++++++++++++++++//
void Release_Buffer()//Release all buffers before exiting.
{
MbufFree(MilGL_AnaLOImage);
MbufFree(MilGL_AnaHIImage);
MbufFree(MilColor2Image);
MbufFree(MilColorImage);
MbufFree(MilTmp2SubImage);
MbufFree(MilTmpSubImage);
MbufFree(MilBinSubImage);
MbufFree(MilBinSub2Image);
MbufFree(MilDstSubImage);
MbufFree(MilSrcSubImage);
MbufFree(MilParentLoImage);
MbufFree(MilParentHiImage);
MbufFree(MilSegImage);
MdispFree(MilOvrDisplay);
MdispFree(MilOvrDisplay2);
MdispFree(MilDisplayL);
MdispFree(MilDisplayL2);
MdispFree(MilDisplayH);
MdispFree(MilDisplayH2);
}
//+++++++++++++++++++++++++++++++++++++++++++++++++++++++++++++++++++++++++++++++//


//+++++++++++++++++++++++++++Wavelet Transform Program+++++++++++++++++++++++//
//Get threshold results from wavelet analysis.
GetThresholdData(float data[], int scale, int lt[], int *ltn)
{
int jj, length, rtn;

float g[11] = {0.0039, 0.0062, -0.0226, -0.112, -0.2309,0.7118, -0.2309, -0.1120, -0.0226, 0.0062,
0.0039};//Detail wavelet filter.
float h[11] = {0.0032, -0.0132, -0.0393, 0.045, 0.2864, 0.4347, 0.2864, 0.045, -0.0393, -0.0132,
0.0032};//Smooth wavelet filter.

length = 10;

for(jj = 0; jj ≤ J; jj++)
{
length = 10;
```

```
apply_filter(data, g, jj, length, wc[jj].G);//Start finding the wavelet results using detail wavelet filter.
length = 10;
apply_filter(data, h, jj, length, wc[jj].H);//Start finding the wavelet results using smooth wavelet filter.
trans_data(data, wc[jj].H);//Copying the smooth histogram for the next loop of wavelet transform.
}
peak_finder(wc[scale].G, lt, &rtn);//Find the peaks to get the threshold values.
*ltn = rtn;
}


//Calculate the wavelet results.
void apply_filter(float d[], float f[], int scale, int len, float out[])
{
int i, j, k, n;
double power;
power = pow(2,scale);//Wavelet scale is equated to the power of 2.
//If lower and upper boundary is reached.
for( j = 0; j < DATA_POINTS; j++ )
{
k = 0;
out[j] = 0;
i = 0;
        while( i <= len * power )
        {
        n = j - ((len * power)/2);
        if( (n+i) >= DATA_POINTS )
        n = 510 - (n+i);
        if( ((n+i) >= 0) && ((n+i) < DATA_POINTS) )
        n = n + i;
        if( (n+i) < 0 )
        n = -(n + i);
        out[j] += d[n] * f[k++];
        i += power;
        }
}
}

//Copying the smooth histogram for the next loop of wavelet transform.
void trans_data(float arr[], float arr1[])
{
        int i;
        for( i = 1; i <= DATA_POINTS; i++ )
        arr[i] = arr1[i];
}

//Algorithms to find the threshold values automatically.
void peak_finder(float a[], int t_point[], int *t_no)
{
int i, j, k, mark;
float min, max;
k = 1;
t_point[0] = 1;

for( i = 1; i < DATA_POINTS; i++ ) //Find the zero crossing points.
if( (a[i-1] < 0 ) && (a[i] > 0) )
{
        max = 0;
        j = i;
        while( (j < DATA_POINTS) && (a[j] > 0) )
        {
```

```
                if( a[j] > max )
                {
                max = a[j];
                mark = j;
                }
        j++;
        }
        j = i - 1;

        min = 0;
        while( (j >= 0) && (a[j] < 0) )
        {
                if( a[j] < min )
                {
                min = a[j];
                mark = j;
        }
        j--;
        }
                if( mark != 0 )
                t_point[k++] = mark;
        }
t_point[k] = 255;
*t_no = k;
}
//+++++++++++++++++++++++++++++++++++++++++++++++++++++++++++++++++++++++++++++++++++++//
```

APPENDIX F

Automated target material detection results

rawdata.dat - Notepad

File Edit Search Help

```
============================
Characteristic Angle Calculation:
============================
Region 1=81.71644,
Region 2=68.37746, Region 2=80.26117, Region 2=76.39536, Region 2=72.29682,
                   Region 2=77.37681, Region 2=75.13670, Region 2=46.59473,
Region 3=64.65063,
Region 4=58.03125,
Region 5=96.65336,
Region 6=39.46174,
Region 7=11.66867,
Region 8=11.84623,
Region 9=19.78272,
Region 10=18.35924,
Region 11=6.95369,
Region 12=22.26294,
Region 13=-11.55807,
Region 14=16.35322,
Region 15=-25.87012, Region 15=-24.69968, Region 15=-26.97391,
Region 16=-25.27200,
Region 17=0.73955,
Region 18=-29.66105,
Region 19=3.77881,
Region 20=3.20191,
Region 21=93.48345, Region 21=67.93536,
Region 22=-43.25926,
Region 23=19.75888,
Region 24=50.04548,
Region 25=3.10292,
Region 26=-35.70063,
Region 27=-37.96353, Region 27=-36.22475,
Region 28=-36.29477, Region 28=-34.38707,
Region 29=91.46074,
Region 30=93.75849,
Region 31=15.27670,
Region 32=91.20030,
Region 33=-36.19017,
Region 34=102.98986,
Region 35=-0.13856,
Region 36=100.18717,
Region 37=92.06525,
Region 38=88.53185, Region 38=83.32624, Region 38=12.45347,
Region 39=92.27846,
Region 40=91.55243, Region 40=-45.77137,
Region 41=1.12078,
Region 42=-28.94430, Region 42=-31.57576,
Region 43=-26.09858,
Region 44=-57.74475, Region 44=-46.73925, Region 44=-61.12887,
                     Region 44=28.59003,
Region 45=27.07110,
Region 46=90.39407, Region 46=87.96343,
Region 47=43.60851,
Region 48=71.37974,
```

Fig. F-1 Automated target material detection results for baggage sample-7.

rawdata.dat - Notepad

File Edit Search Help

```
Region 49=-44.18206,
Region 50=90.55663, Region 50=89.99867,
Region 51=102.60824, Region 51=77.33701, Region 51=99.36770,
                     Region 51=98.96157,
Region 52=88.13845,
Region 53=88.70390,
Region 54=88.80175,
Region 55=94.65714, Region 55=93.65452,
Region 56=87.76239,
Region 57=90.27296,
Region 58=95.08399,
Region 59=96.68521,
Region 60=90.46128, Region 60=92.42639,
Region 61=96.78835,
Region 62=96.26297,
Region 63=99.95884,
Region 64=75.11012, Region 64=-46.91159,
Region 65=89.95075,
Region 66=-51.59444, Region 66=88.44465,
Region 67=-8.98994,
Region 68=-53.23882, Region 68=91.28669, Region 68=62.30036,
Region 69=-55.35296, Region 69=88.80103, Region 69=89.23031,
                     Region 69=86.49386,
Region 70=-33.66942,
Region 71=-62.94290, Region 71=85.41942,
Region 72=94.66255,
Region 73=99.98811,
Region 74=94.82452,
Region 75=93.70807,
Region 76=95.22716,
Region 77=95.33258,
Region 78=95.64986,
Region 79=96.70949,
Region 80=95.49500,
Region 81=94.30302.
```

Fig. F-1 Automated target material detection results for baggage sample-7 (continuation from previous page).

```
rawdata.dat - Notepad
File  Edit  Search  Help
==============================
Characteristic Angle Calculation:
==============================
Region 1=56.52413, Region 1=78.50345, Region 1=69.49212, Region 1=79.60270,
                   Region 1=69.98707, Region 1=72.17822, Region 1=64.57564,
                   Region 1=66.69694, Region 1=67.56841, Region 1=68.64759,
                   Region 1=72.67509,
Region 2=66.68794,
Region 3=24.40221,
Region 4=33.72805,
Region 5=44.42151,
Region 6=40.45634,
Region 7=8.49325,
Region 8=-40.67221, Region 8=-33.12770,
Region 9=50.22016,
Region 10=66.16405,
Region 11=53.35768,
Region 12=-10.23352,
Region 13=-34.43668,
Region 14=2.28930,
Region 15=-33.38409,
Region 16=-5.01019,
Region 17=69.37885,
Region 18=-28.82071, Region 18=-33.55720, Region 18=-23.07009,
Region 19=12.39232,
Region 20=-53.44967,
Region 21=-21.88296,
Region 22=-18.70314,
Region 23=73.97795, Region 23=-54.18752,
Region 24=-5.40698,
Region 25=-10.37048,
Region 26=-11.94172,
Region 27=-41.92266,
Region 28=-31.64178,
Region 29=-14.54936,
Region 30=-40.08066,
Region 31=-19.08567,
Region 32=6.83702,
Region 33=-24.54047,
Region 34=109.31362,
Region 35=97.65405,
Region 36=91.61823,
Region 37=88.84023, Region 37=2.30473,
Region 38=94.81638,
Region 39=91.54683,
Region 40=88.58219,
Region 41=88.33269,
Region 42=100.46635,
Region 43=71.09296,
Region 44=66.54616,
Region 45=92.07295,
Region 46=92.82705,
Region 47=95.10883,
```

Fig. F-2 Automated target material detection results for baggage sample-8.

rawdata.dat - Notepad

File Edit Search Help

```
Region 48=78.25285, Region 48=87.44632, Region 48=64.50966, Region 48=77.17824,
Region 49=86.72281,
Region 50=98.91290,
Region 51=-11.17730, Region 51=11.61622,
Region 52=88.10528,
Region 53=85.00317,
Region 54=-69.52346, Region 54=-47.07146, Region 54=-49.53858, Region 54=-48.09935,
                     Region 54=-49.28974, Region 54=-46.42924, Region 54=-44.82936,
                     Region 54=-47.63926, Region 54=-42.90538,
Region 55=40.25753,
Region 56=89.42403,
Region 57=93.73311,
Region 58=99.78447,
Region 59=96.50468,
Region 60=93.08858,
Region 61=98.14894,
Region 62=78.41258, Region 62=92.76857, Region 62=91.66837, Region 62=85.13185,
                    Region 62=82.49123, Region 62=85.74236, Region 62=83.56195,
                    Region 62=85.71021,
Region 63=89.04585,
Region 64=90.36250, Region 64=90.21413, Region 64=90.03380,
Region 65=91.13523,
Region 66=85.69439, Region 66=85.50218,
Region 67=90.32956,
Region 68=83.18325,
Region 69=89.99013,
Region 70=91.13313,
Region 71=90.76616,
Region 72=89.57011,
Region 73=90.22137,
Region 74=60.99745, Region 74=80.64498,
Region 75=90.67745,
Region 76=82.27731,
Region 77=89.96205, Region 77=88.95937,
Region 78=71.69666, Region 78=77.94430,
Region 79=92.27096, Region 79=91.12382,
Region 80=90.80006, Region 80=94.27597,
Region 81=88.20256,
Region 82=60.09027,
Region 83=54.10251, Region 83=69.62805,
Region 84=87.69443, Region 84=87.18924, Region 84=88.74304,
Region 85=91.76834,
Region 86=86.67098,
Region 87=91.46588,
Region 88=91.78646,
Region 89=94.89180,
Region 90=87.87444,
Region 91=87.52097, Region 91=67.15308,
Region 92=85.71243, Region 92=87.51488,
Region 93=86.69863,
Region 94=62.41732,
Region 95=88.55926, Region 95=69.47194, Region 95=53.63540, Region 95=94.40633,
Region 96=91.79435,
```

Fig. F-2 Automated target material detection results for baggage sample-8 (continuation from previous page).

rawdata.dat - Notepad

File Edit Search Help

```
Region 97=76.28710,
Region 98=94.44338,
Region 99=91.64635,
Region 100=96.51018,
Region 101=86.10539, Region 101=85.87854, Region 101=-31.99136,
Region 102=91.54485, Region 102=90.73702,
Region 103=87.20590, Region 103=84.61434,
Region 104=85.83255,
Region 105=82.88060, Region 105=89.89426,
Region 106=90.27294,
Region 107=90.28674, Region 107=86.10706,
Region 108=91.77544,
Region 109=89.13635,
Region 110=89.46176, Region 110=90.86705,
Region 111=91.55386, Region 111=84.03243, Region 111=89.44147,
Region 112=92.56175,
Region 113=97.05740, Region 113=97.19205, Region 113=94.56953, Region 113=93.91390,
Region 114=87.08094, Region 114=81.09691,
Region 115=94.15379,
Region 116=91.51182,
Region 117=98.17889,
Region 118=91.99435, Region 118=88.72262, Region 118=77.60357,
Region 119=90.69617,
Region 120=80.17910, Region 120=70.35814,
Region 121=100.03389,
Region 122=105.05125,
Region 123=-67.11879,
Region 124=-65.72247, Region 124=87.51284,
Region 125=-60.36696,
Region 126=77.06398,
Region 127=-67.75916,
Region 128=-68.35810,
Region 129=-64.50383, Region 129=85.45429, Region 129=89.81789, Region 129=80.62009,
Region 130=-67.40817,
Region 131=-69.28773,
Region 132=92.70072,
Region 133=85.96565, Region 133=89.87573, Region 133=54.40276, Region 133=-4.94293,
Region 134=58.11046,
Region 135=94.02944,
Region 136=57.67711,
Region 137=83.63741,
Region 138=93.37226,
Region 139=90.31422,
Region 140=74.01167,
Region 141=97.67355,
Region 142=103.32936,
Region 143=100.88396,
Region 144=95.61390,
Region 145=96.11742,
Region 146=96.97642,
Region 147=94.58994,
Region 148=95.10535, Region 149=94.88110, Region 150=95.55203, Region 151=95.26467,
Region 152=96.30547, Region 153=97.10125, Region 154=94.58871, Region 155=98.81521,
Region 156=97.73672, Region 157=97.45539, Region 158=95.43822
```

Fig. F-2 Automated target material detection results for baggage sample-8 (continuation from previous page).

rawdata.dat - Notepad

File Edit Search Help

```
==============================
Characteristic Angle Calculation:
==============================
Region 1=-31.71151,
Region 2=-38.40773,
Region 3=-38.21153,
Region 4=-35.60839,
Region 5=-41.81065,
Region 6=-32.72905, Region 6=-31.06429,
Region 7=89.73974, Region 7=7.78474,
Region 8=95.75783,
Region 9=100.22521,
Region 10=53.14261,
Region 11=47.40845,
Region 12=82.76204,
Region 13=87.13686,
Region 14=91.24172,
Region 15=92.06663,
Region 16=91.89171,
Region 17=91.53809,
Region 18=93.25097,
Region 19=96.40700,
Region 20=95.00885,
Region 21=94.01268,
Region 22=96.86032,
Region 23=93.20047,
Region 24=93.02666,
Region 25=93.38044,
Region 26=8.25728,
Region 27=93.19237,
Region 28=92.95786,
Region 29=85.00068, Region 29=89.29012,
Region 30=46.78839,
Region 31=85.51952, Region 31=89.76665,
Region 32=21.47967, Region 32=91.39058,
Region 33=94.52086,
Region 34=94.28940,
Region 35=91.93095, Region 35=-45.49349, Region 35=89.84107,
Region 36=89.18994,
Region 37=93.25659,
Region 38=86.14906, Region 38=88.13691, Region 38=92.37620,
                    Region 38=85.20734, Region 38=90.18815, Region 38=88.48440,
```

rawdata.dat - Notepad

File Edit Search Help

```
Region 39=91.21652,
Region 40=81.07386,
Region 41=99.41047,
Region 42=97.51681,
Region 43=94.95921, Region 43=94.56848,
Region 44=91.91591,
Region 45=-68.26969,
Region 46=-69.72177,
Region 47=-70.77852,
Region 48=95.24356, Region 48=89.03087,
Region 49=82.86801,
Region 50=94.11636,
Region 51=83.34292, Region 51=96.75286,
Region 52=95.78115, Region 52=99.85773,
Region 53=102.93588,
Region 54=94.58212,
Region 55=95.01466,
Region 56=93.96333,
Region 57=95.76445,
Region 58=92.95766,
Region 59=95.12816,
```

Fig. F-3 Automated target material detection results for baggage sample-9.